

**NANOINDENTATION STUDY AND QUANTITATIVE  
BACKSCATTERED ELECTRON IMAGING OF  
HUMAN CORTICAL BONE**

by

**LEANDRO DE MACEDO SOARES SILVA**

BASc in Mechanical Engineering, Federal University of Santa Catarina, Brazil, 2003

BASc in Mechanical Engineering, École Nationale Supérieure d'Arts et Métiers, France, 2001

A THESIS SUBMITTED IN PARTIAL FULFILLMENT OF  
THE REQUIREMENTS FOR THE DEGREE OF

**MASTER OF APPLIED SCIENCE**

in

THE FACULTY OF GRADUATE STUDIES

(Materials Engineering)

THE UNIVERSITY OF BRITISH COLUMBIA

February 2006

© Leandro de Macedo Soares Silva, 2006

## **Abstract**

Bone fracture is a burden for health care and especially for individuals suffering the consequences of fracture. Osteoporosis reduces bone mass and increases the likelihood of fracture as it causes bone thinning and increases porosity. The understanding of Peripheral Quantitative Computed Tomography (pQCT), a clinical tool used in bone health diagnosis to assess bone quality, requires an evaluation of bone mineral content (BMC) and porosity distribution across the cortex. This new analysis is introduced in this work.

Cortical bone quality depends on three factors: material properties, BMC and degree of porosity. Two key techniques were used to characterize bone structure and properties. Nanoindentation equipped with continuous stiffness measurement (CSM) allows depth-dependence measurement of material properties (elastic and viscoelastic). Quantitative Backscattered Electron Imaging (qBSEi) is a microscopy technique capable of quantifying the BMC and the porosity of bone tissue. Seventeen human cortical tibiae specimens, ranging from 67 to 88 years old, were used in this study. The results on nanoindentation and qBSEi and their correlation to pQCT data will be presented along with a statistical analysis.

The material properties of bone were intrinsically dependent on measurement conditions and water content had an important role in bone mechanics. Moistening bone reduced the elastic modulus and hardness and increased its viscoelasticity. The elastic modulus of bone increased with increasing BMC. In the bone microstructure, interstitial bone was more mineralized than osteonal bone, and thus had higher elastic modulus. The elastic modulus of

bone varied across the cortex; however, the central part of cortical bone remained uniform. The BMC distribution across the cortex was statistically uniform.

The degree of porosity in bone greatly influenced the pQCT measurement of apparent density; while BMC did not contribute as much as porosity. It is concluded that even though the bone mineral content appeared as an indicator of bone quality at the microscale level, it becomes less obvious at the macroscale level. At this level porosity becomes the major factor affecting bone density.

# Table of Contents

Abstract.....	ii
Table of Contents.....	iv
List of Tables.....	vii
List of Figures.....	viii
List of Abbreviations.....	xi
Acknowledgments.....	xii
Chapter 1 Introduction.....	1
1.1 Structural Organization of Bone.....	3
1.2 Osteoporosis and Age-Related Bone Loss.....	5
1.3 Clinical Evaluation of Bone Quality.....	7
1.3.1 Dual-energy X-ray Absorptiometry (DEXA).....	8
1.3.2 Peripheral Quantitative Computed Tomography (pQCT).....	8
1.4 Bone Mineral Content and Porosity Quantification.....	9
1.4.1 Contact Microradiography.....	9
1.4.2 Quantitative Backscattered Electron Imaging (qBSEi).....	10
1.4.2.1 <i>qBSEi Study of Bone</i> .....	11
1.4.2.2 <i>Cortical Bone Porosity</i> .....	12
1.5 Nanoindentation Testing of Bone.....	12
1.5.1 Theory of Instrumented Indentation Testing.....	13
1.5.1.1 <i>Hardness and Modulus calculation</i> .....	14
1.5.1.2 <i>Continuous Stiffness Measurement – CSM</i> .....	16
1.5.1.3 <i>Instrumentation of a Nanoindenter</i> .....	17
1.5.2 Current Progress in Nanoindentation of Bone.....	19
1.6 Objectives of this Research Work.....	21
1.7 Scope of this Research.....	22
Chapter 2 Materials and Methodology.....	23

<b>2.1 Bone Nanoindentation .....</b>	<b>23</b>
2.1.1 Sample Preparation .....	24
2.1.2 Positioning of the Nanoindentations .....	25
2.1.2.1 <i>Tibia Medial Aspect Testing</i> .....	26
2.1.3 Wet Measurements .....	27
2.1.3.1 <i>Effect of water on the Indenter Tip</i> .....	27
2.1.4 Dry Measurements .....	31
2.1.5 CSM Frequency and Amplitude .....	32
2.1.5.1 <i>CSM Frequency</i> .....	32
2.1.5.2 <i>CSM Amplitude</i> .....	32
<b>2.2 Bone Mineral Content and Porosity Quantification .....</b>	<b>34</b>
2.2.1 Quantitative Backscattered Electron Imaging (qBSEi) .....	34
2.2.1.1 <i>Calibration of the BSE signal</i> .....	34
2.2.1.2 <i>Standardization of the BSE signal</i> .....	36
2.2.1.3 <i>BSE Image Grey-level Analysis</i> .....	38
2.2.2 Porosity Analysis .....	40
<b>2.3 pOCT – qBSEi Correlation Procedure .....</b>	<b>41</b>
<b>2.4 Statistical Analysis .....</b>	<b>43</b>
2.4.1 Basic Material Properties t-test .....	44
2.4.2 Modulus and Bone Mineral Content Distribution across Medial Cortex .....	44
2.4.3 Linear Regression and Correlation .....	45
<b>Chapter 3 Results .....</b>	<b>46</b>
<b>3.1 Basic Material Properties of Bone .....</b>	<b>46</b>
3.1.1 Effect of Water Content, Harmonic Frequency, and Air-Drying Time .....	48
3.1.1.1 <i>Water Content Effect on Modulus, Hardness and Phase Angle</i> .....	48
3.1.1.2 <i>CSM Frequency Effect on Modulus, Hardness and Phase Angle</i> .....	49
3.1.1.3 <i>Air-Drying Time Effect on Modulus, Hardness and Phase Angle</i> .....	50
3.1.2 Wet-Dry Correlation .....	52
<b>3.2 Modulus of Elasticity Distribution across Medial Cortical Wall .....</b>	<b>52</b>
<b>3.3 Bone Mineral Content Distribution across Medial Cortical Wall .....</b>	<b>58</b>
3.3.1 Modulus versus Bone Mineral Content Correlation .....	62
<b>3.4 pOCT Imaging – qBSEi Correlation .....</b>	<b>64</b>
3.4.1 Mean Bone Mineral Content across Cortical Wall .....	64
3.4.2 Porosity across Cortical Wall .....	65
3.4.3 pOCT Reading and Correlation .....	67
<b>Chapter 4 Discussions .....</b>	<b>71</b>

<b>4.1 Basic Material Properties of Bone.....</b>	<b>71</b>
<b>4.2 Modulus and Bone Mineral Content Distribution.....</b>	<b>73</b>
<b>4.3 pQCT Imaging – qBSEi Correlation .....</b>	<b>75</b>
<b>Chapter 5 Conclusions.....</b>	<b>78</b>
<b>Chapter 6 Recommendations for Future Work.....</b>	<b>80</b>
<b>References .....</b>	<b>81</b>
<b>Appendices.....</b>	<b>88</b>
<b>Appendix A – Contact Microradiography.....</b>	<b>88</b>
<b>Appendix B – Anatomical Site Testing .....</b>	<b>89</b>
<b>Appendix C – Newman-Keuls Post-hoc analysis .....</b>	<b>93</b>
<b>Appendix D – Ethical Approval.....</b>	<b>94</b>

## List of Tables

<i>Table 2.1 List of human medial tibia samples. ....</i>	<i>27</i>
<i>Table 2.2 Elastic modulus and hardness for both dry and wet fused silica. ....</i>	<i>28</i>
<i>Table 2.3 Nanoindentation results of Z100 composite in dry and re-wetted conditions. ....</i>	<i>29</i>
<i>Table 2.4 Nanoindentation results of Z100 composite in re-dried conditions. ....</i>	<i>29</i>
<i>Table 2.5 Modulus, Hardness and Phase Angle: 2 nm, 5nm and 10 nm CSM amplitude. ....</i>	<i>34</i>
<i>Table B1 Bone specimens for anatomical site testing. ....</i>	<i>89</i>
<i>Table C1 Modulus Post-hoc analysis – Newman-Keuls test. ....</i>	<i>93</i>
<i>Table C2 Bone Mineral content Post-hoc analysis – Newman-Keuls test.....</i>	<i>93</i>

## List of Figures

<i>Figure 1.1 Hierarchical structural organization of bone [7].</i>	3
<i>Figure 1.2 Human Haversian systems (diameter ~200 microns).</i>	5
<i>Figure 1.3 Temporal changes in bone mass during life [14].</i>	7
<i>Figure 1.4 Voxel dimensions used in pQCT measurements.</i>	9
<i>Figure 1.5 Types of signals of SEM.</i>	10
<i>Figure 1.6 Berkovich indent imprint.</i>	14
<i>Figure 1.7 Load-displacement curve from where contact stiffness (S) is derived.</i>	15
<i>Figure 1.8 Schematic of the CSM loading cycle.</i>	17
<i>Figure 1.9 Schematic of a MTS Nano Indenter XP instrument [48].</i>	18
<i>Figure 2.1 Results from a typical nanoindentation test. a) Load on sample; b) Hardness; c) Elastic modulus; d) Phase angle vs. displacement into surface.</i>	24
<i>Figure 2.2 a) Cross-section of the distal tibia; b) Detailed view cortical wall – anterior site; c) Detailed view of an individual osteon with five indents.</i>	25
<i>Figure 2.3 Modulus for dental composite using 10 nm CSM amplitude (dry, re-wetted, re-dried (24 hours) and re-dried (48 hours)).</i>	30
<i>Figure 2.4 Modulus for dental composite: A) 2 nm, B) 5nm and C) 10 nm CSM amplitudes.</i>	33
<i>Figure 2.5 Calibration of BSE signal.</i>	35
<i>Figure 2.6 Standardization of BSE signal.</i>	37
<i>Figure 2.7 Osteoid, carbon and aluminum standard samples used in qBSEi technique.</i>	38
<i>Figure 2.8 Grey-level histogram for image analysis.</i>	38
<i>Figure 2.9 qBSEi of medial aspect of tibia 1096L.</i>	39
<i>Figure 2.10 Osteonal indentations (total 5; one labelled) in an image used for bone mineral content analysis.</i>	40
<i>Figure 2.11 Medial aspect of sample 1097L (top) and threshold for porosity quantification (bottom). Horizontal length – 3350 <math>\mu\text{m}</math>.</i>	41

<i>Figure 2.12 Bone density reading provided by pQCT – tibia sample 1096L.</i>	42
<i>Figure 3.1 Modulus, Hardness and Phase angle with depth-dependence measurements.</i>	47
<i>Figure 3.2 Effect of water content and harmonic frequency on Elastic Modulus.</i>	48
<i>Figure 3.3 Effect of water content and harmonic frequency on Hardness.</i>	49
<i>Figure 3.4 Effect of water content and harmonic frequency on Loss Tangent.</i>	50
<i>Figure 3.5 Effect of air-drying (time) on elastic modulus.</i>	51
<i>Figure 3.6 Wet-dry elastic modulus correlation.</i>	52
<i>Figure 3.7 Typical modulus distribution across medial cortical wall.</i>	53
<i>Figure 3.8 Normalized modulus distribution across medial cortical wall.</i>	54
<i>Figure 3.9 Mean (<math>\pm</math>SD) elastic modulus distribution for five cortical wall subregions (periosteum – 0 – 20%).</i>	55
<i>Figure 3.10 Modulus two-way repeated measures ANOVA.</i>	56
<i>Figure 3.11 Abnormal modulus distribution across medial cortical wall.</i>	57
<i>Figure 3.12 qBSEi of sample 1097L used to map bone mineral content distribution. Horizontal length – 3350 <math>\mu</math>m.</i>	58
<i>Figure 3.13 Typical calcium content distribution across medial cortical wall.</i>	58
<i>Figure 3.14 Normalized calcium content distribution across medial cortical wall.</i>	59
<i>Figure 3.15 Abnormal calcium content distribution across medial cortical wall.</i>	60
<i>Figure 3.16 Mean (<math>\pm</math>SD) calcium content modulus distribution for five cortical wall subregions (periosteum – 0 – 20%).</i>	61
<i>Figure 3.17 Bone Mineral content two-way repeated measures ANOVA.</i>	62
<i>Figure 3.18 Scatterplot of modulus versus bone mineral content.</i>	63
<i>Figure 3.19 Linear regression for the modulus versus bone mineral content correlation.</i>	63
<i>Figure 3.20 Mean bone mineral content for five zones division cortex.</i>	64
<i>Figure 3.21 qBSEi for sample 1095L. Horizontal length – 3100 <math>\mu</math>m.</i>	65
<i>Figure 3.22 qBSEi for sample 1096L. Horizontal length – 4300 <math>\mu</math>m.</i>	66

<i>Figure 3.23 qBSEi for sample 1069L. Horizontal length – 4100 <math>\mu\text{m}</math>.</i>	66
<i>Figure 3.24 Porosity variation for five zones division cortex.</i>	67
<i>Figure 3.25 Apparent density by pQCT for five zones division cortex.</i>	68
<i>Figure 3.26 Effect of porosity in the apparent density measured by pQCT.</i>	69
<i>Figure 3.27 Effect of bone mineral content in the apparent density measured by pQCT.</i>	69
<i>Figure 3.28 Calculated density compared to the apparent density measured by pQCT.</i>	70
<i>Figure 4.1 Modulus two-way repeated measures ANOVA.</i>	74
<i>Figure 4.2 Log-log correlation between modulus and bone mineral content.</i>	75
<i>Figure 4.3 Bone density reading provided by pQCT – sample 1069L</i>	76
<i>Figure A1 Contact microradiograph picture with aluminium step-wedge calibration.</i>	88
<i>Figure B1 Modulus distribution – 1067R – all anatomical sites.</i>	90
<i>Figure B2 Modulus distribution – 1096R – all anatomical sites.</i>	91

## **List of Abbreviations**

MSK – Musculoskeletal System

SD – Standard Deviation

pQCT – Peripheral Quantitative Computed Tomography

DEXA – Dual-energy X-ray Absorptiometry

qBSEi – Quantitative Backscattered Electron Imaging

NCP – Non-collagenous Protein

WHO – World Health Organization

BMC – Bone Mineral Content

BMD – Bone Mineral Density

BMDD – Bone Mineral Density Distribution

SEM – Scanning Electron Microscopy

BSE – Backscattered Electron

DSI – Depth-sensing Indentation

IIT – Instrumented Indentation Testing

CSM – Continuous Stiffness Measurement

VGH – Vancouver General Hospital

PBS – Phosphate Buffered Solution

EDTA – Ethylene Diamine Tetra-acetic Acid

BSEi – Backscattered Electron Imaging

ANOVA – Analysis of Variance

## **Acknowledgments**

I am delighted to express my sincere gratitude to many people who have kindly provided me with great contributions to the completion of my thesis. I would like to thank both my supervisors, Dr. Rizhi Wang and Dr. Thomas Oxland, for their incessant motivation and guidance during these two years of research work.

I am thankful to all my colleagues and staff at the Department of Materials Engineering (MTRL), at the Advanced Materials and Process Engineering Laboratory (AMPEL) and at the Division of Orthopaedic Engineering Research Division (DOER) for their support in several ways.

I would also like to thank the Canadian Institutes of Health Research (CIHR) and the Department of Materials Engineering (MTRL) who supported me and the research included in this thesis.

I would also like to thank my lovely family – to my dad, for being an example to me not only as a brilliant engineer but also for his great character and living; to my mom, for her continual prayers, spiritual guidance and encouraging words and her example of perseverance; and to my sister, for inspiring me with her longing and enthusiasm of improving the quality of human life.

Above all, I would like to express my gratefulness to God who, unconditionally, gives me the continual strength and guides my path every day of my life. May all the honour and glory be to Him.

## **Chapter 1 Introduction**

Bone is a vital tissue in the human body, and the maintenance of good bone quality is essential to a healthy life and prevention of fracture. Once bone starts to lose its quality and is not able to cope with its functions, problems start to arise and the likelihood of fractures increases dramatically. Bone fracture represents an enormous burden for the government and especially for those suffering from its symptoms. For example, hip fracture alone costs the Canadian government approximately 1.2 billion dollars per year. Hip fracture results in death in up to 20% of the cases and disability in 50% of those who survive [1-3]. In young people it is usually caused by high-impact trauma such as a car accident. However, in elderly people, simple falls due to impairments of muscle strength, neuromuscular coordination, balance, vision, and hearing, could result in fractures. Consequently, the understanding of bone fracture and possibly the prevention of these events are extremely important. To achieve this purpose, one requires the combined knowledge from two fields: engineering science and orthopaedic science. This research work is a combination of both mechanical and materials engineering applied to the studies of the musculoskeletal system (MSK), with particular emphasis on the skeletal system (bone tissue).

Bones form the hard tissue of the skeletal system. The skeletal system is a vital system in the human body and is responsible for several fundamental functions: maintaining the posture of the body (structural function); protecting the soft tissues located in the pelvic, thoracic and cranial cavities (protective function); transmitting the force of muscular contraction allowing human movements (locomotive function). Bone is also a reservoir of ions, principally

calcium in the bone marrow [4]. Section 1.1 will provide further information on bone structure.

Bone disorders can occur at any stage in life, from childhood to advanced ages. Osteoporosis is the most common metabolic bone disease and is more likely to affect elderly people. It is characterized as low bone mass with structural deterioration, increasing the likelihood of bone fracture. Section 1.2 will present further details on osteoporosis and age-related bone loss.

Bone fracture is a massive problem for the government and creates elevated costs to the health care system. As osteoporosis increases the likelihood of fracture, it is a common practice in health clinics and hospitals to diagnose bone quality. This is performed using clinical evaluative tools, such as Peripheral Quantitative Computed Tomography (pQCT) and Dual-energy X-ray Absorptiometry (DEXA), further explained in section 1.3.

Section 1.4 introduces a technique called quantitative backscattered electron imaging (qBSEi), which is used to measure the bone mineral content (BMC) and the degree of porosity of cortical bone. These two parameters will be used to establish a correlation with the bone apparent density provided by pQCT. Section 1.5 describes the Nanoindentation technique, a widely used technique to characterize bone material properties. The Introduction chapter is then finalized by stating the objectives and scope of this research work in sections 1.6 and 1.7 respectively.

## 1.1 Structural Organization of Bone

Bone has a very distinctive organization with seven hierarchical levels from nanoscale constituents to macroscopic bone [5-7] (Figure 1.1). The first level defines bone as a composite material [8, 9], where the two solid components are collagen fibres and carbonated apatite nanocrystals (also called hydroxyapatite –  $\text{Ca}_{10}(\text{OH})_2(\text{PO}_4)_6$ ). Water is a third component and it plays an important role in the mechanical behaviour of bone. There are also many non-collagenous proteins (NCPs) that together represent less than 10% of the total protein content. Bone is composed of approximately 70 wt% mineral crystals, 25 wt% collagen protein, 5 wt% non-collagenous proteins and water, although the proportion of these components varies.

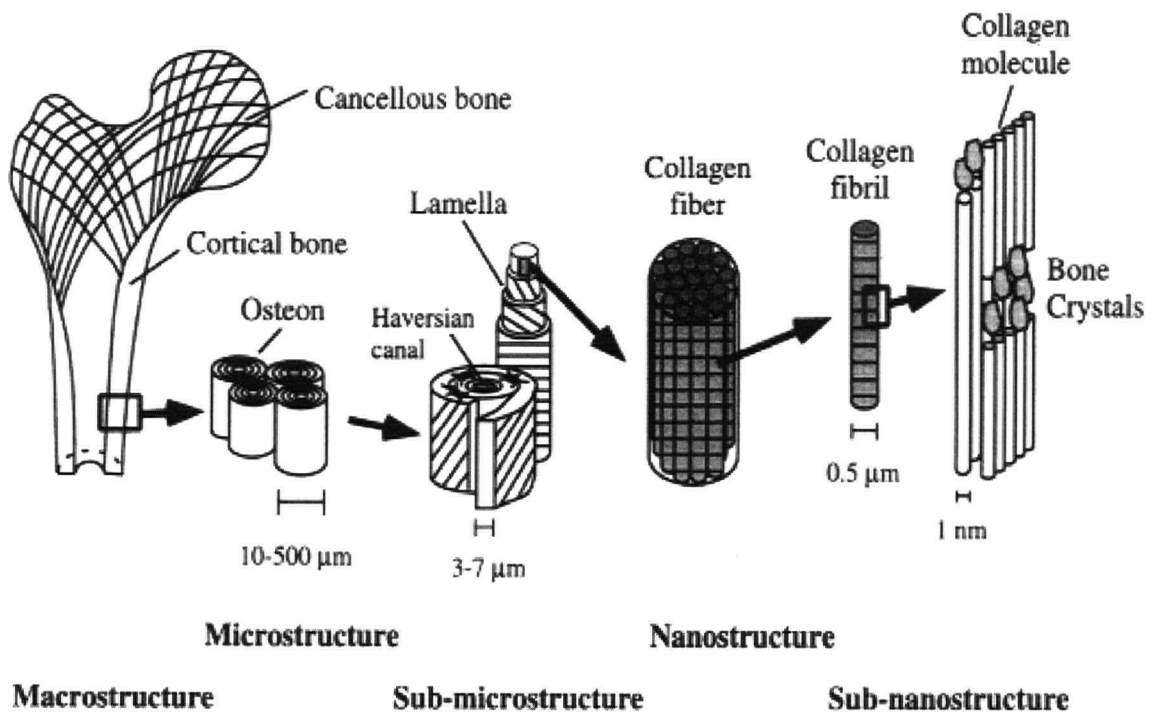


Figure 1.1 Hierarchical structural organization of bone [7].

At the second level of organization, the basic constituents assemble together to form a mineralized collagen fibril. At the third level of organization, a thicker bundle is formed from these previous mineralized collagen fibrils. At the fourth level, a remarkable diversity in structure occurs, with the mineralized bundles organized in a variety of patterns. The three most common patterns for bone are: parallel-fibered bone, woven bone and lamellar bone.

The structural organization comes to the macroscopic range at the fifth level, with cylindrical motifs called osteons. Osteon, also called Haversian system, is the basic unit of structure of cortical bone (sixth level). In the center of the osteon there is a channel called the Haversian canal. The Haversian system is created through a complex and significant process called bone remodelling [10-12], a bone turnover that helps to maintain load bearing, to repair microscopic structural damage, and to replace old bone. Figure 1.2 shows a picture of Haversian systems from a human ulna bone taken using transmitted light in an optical microscope. Bone remodelling consists of excavation of large tunnels (~200  $\mu\text{m}$  in diameter and ~300  $\mu\text{m}$  long) by specialized cells called osteoclasts (responsible for bone resorption). These tunnels are subsequently refilled with newer bone matrix; starting with a thin layer of cement followed by lamellar bone and repeatedly until a narrow remaining channel is left as a blood vessel. Cells called osteoblasts are responsible for the bone deposition process, which takes about 2 to 4 months in humans. The remaining old bone around the Haversian systems is called interstitial bone.

The difference between cortical and trabecular bone (two types of macroscopic bone) comes at the sixth level of organization (Figure 1.1 – macrostructure). Cortical bone, also called

compact bone, is a solid bone with very low porosity (canaliculi, osteocytes lacunae and blood channels). It is a heavier bone and has higher density when compared to trabecular bone. Trabecular bone, also called cancellous or spongy bone, is highly porous (visible porosity). In long bones, such as tibia and femur (seventh level of organization), the epiphysis (extremity of the long bone) is formed mostly by cancellous bone covered with a thin layer of cortical bone. The diaphysis (shaft of the long bone) is formed by cortical bone. Bone differs in size, function and shape (long bone, short bone, flat bone, irregular bone).

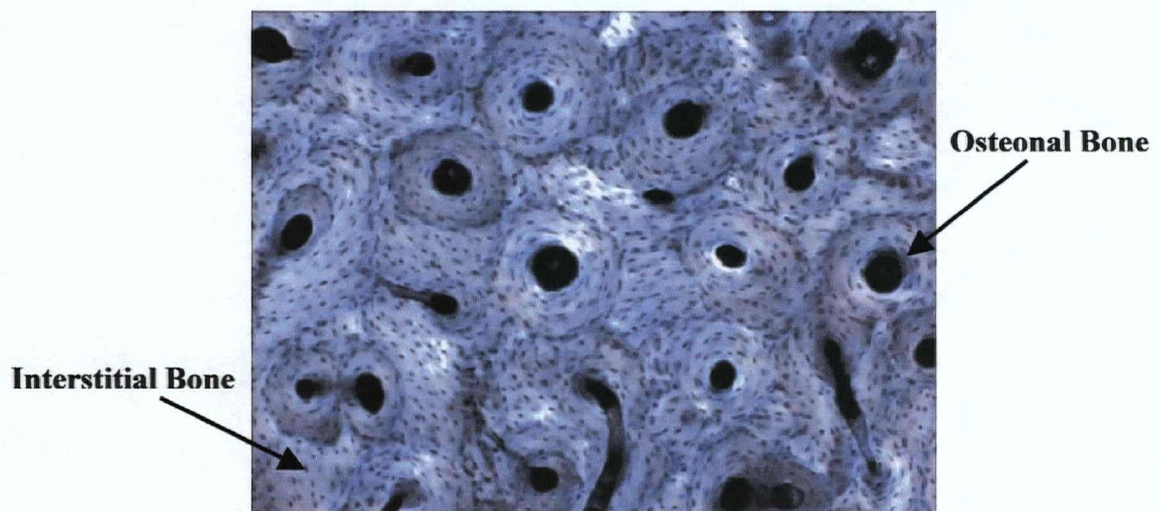


*Figure 1.2 Human Haversian systems (diameter ~200 microns).*

## **1.2 Osteoporosis and Age-Related Bone Loss**

Several bone disorders might occur during the span of life, from childhood to advanced ages, which affect the behaviour of bone and consequently might impair the quality of life. The purpose in this section is to provide a brief description about osteoporosis disease and age-related bone loss, and how it affects bone mechanics and deteriorates its quality.

Osteoporosis is a skeletal disease characterized by a decrease in bone mass and deterioration in bone microarchitecture, leading to an enhanced fragility of the skeleton and consequently a greater risk of fracture. With increased life expectancy, the likelihood of osteoporosis also increases. Osteoporosis affects mainly women, about 80% of the cases, and this is due mainly to the imbalance of hormones after menopause. The probability of hip fracture due to osteoporosis is also twice as large in the female population as in the male population.

Figure 1.3 shows the temporal changes in human bone mass during life. Human bone mass increases during growth, achieves its peak in young adult life and after about 30.5 years it begins to decrease [13-16]. At 70 years, less than 70% of the young adult mass remains. Osteoporosis is an excessive loss in bone mass. Osteoporosis has been defined to be once bone mass reaches a level where it can no longer maintain normal mechanical support. Bone loss occurs in all parts of the skeleton, but not in equal amounts. Osteoporosis is responsible for more than 1.5 million fractures annually (700,000 – vertebral fractures, 300,000 – hip fractures, 250,000 – wrist fractures and 300,000 at other sites) [17]. Usually women begin to lose bone mass approximately ten years earlier than men and also twice as fast. Prior to osteoporosis, both cortical and trabecular bone thin at the endosteal location and the porosity of the Haversian canals increases [18-20]. The World Health Organization (WHO) uses a statistical comparative definition for osteoporosis [21, 22], defined by a BMC that is 2.5 or more standard deviations (SD) below the mean value of a young adult reference. Low bone mass lies between 1 and 2.5 SD below the mean and a normal bone lies between 0 and 1 SD below the mean. Bone quality deteriorates with age; consequently fractures are more likely to happen in the older population.

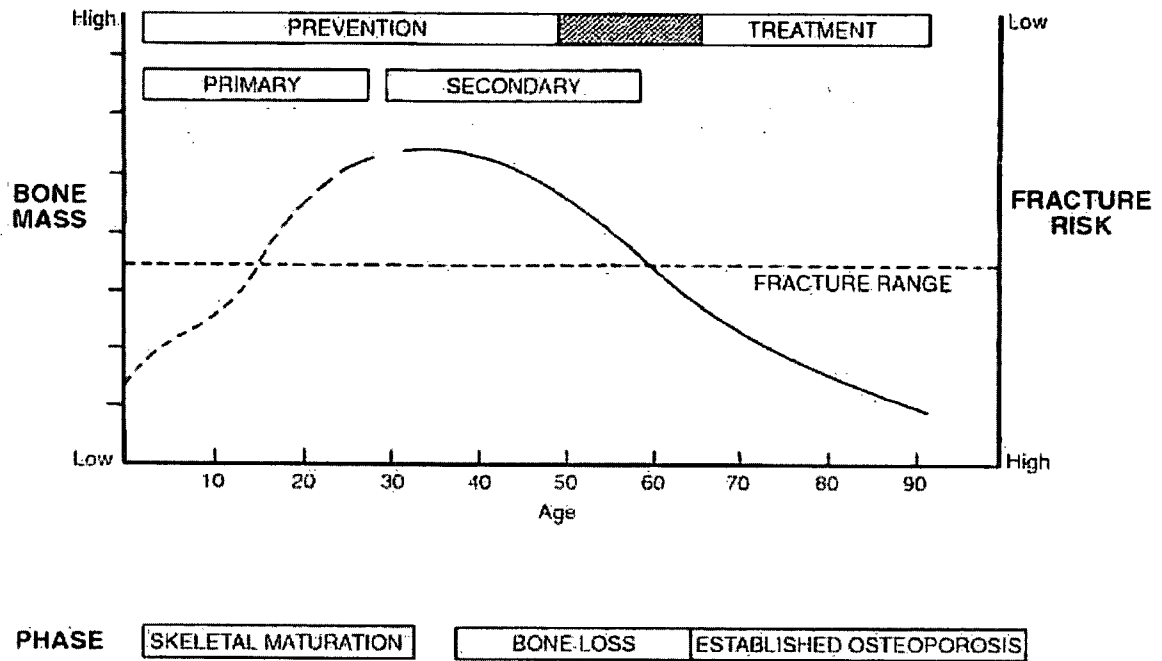


Figure 1.3 Temporal changes in bone mass during life [14].

### 1.3 Clinical Evaluation of Bone Quality

As seen in the previous section, all people lose bone mass (both cortical and trabecular bone) as they age. Identifying those who have excessive bone loss and fragility is crucial to establish preventive and/or therapeutic measures.

Two techniques using X-ray radiation are widely employed as clinical evaluative tools: Dual-energy X-ray Absorptiometry (DEXA) [23] and Peripheral Quantitative Computed Tomography (pQCT) [24, 25]. For both instruments, the radiation attenuation (reduction in intensity) is measured for a fixed amount of bone tissue. An osteoporotic bone presents a low level of attenuation.

### **1.3.1 Dual-energy X-ray Absorptiometry (DEXA)**

DEXA became very popular as it provided a relatively fast and low radiation exposure in a useful clinical tool for bone densitometry. DEXA measures the attenuation of X-ray beams using two different energies and consequently is able to compensate for the presence of soft tissue. DEXA is based on a two-dimensional (2D) image and provides a value of areal bone mineral density (aBMD) in  $\text{mg}/\text{cm}^2$ . Due to the limitations to estimate bone volume, DEXA measurements are not able to distinguish between cortical and trabecular bone.

### **1.3.2 Peripheral Quantitative Computed Tomography (pQCT)**

pQCT measurements are also based on the attenuation of the X-ray radiation; however, in pQCT it comes from a multitude of beams and not only unidirectional as in DEXA. pQCT is based on a three-dimensional (3D) image and consequently can differentiate cortical and trabecular bone. For this reason, pQCT will be used in this research work, which focused only on cortical bone [26]. pQCT uses voxels to measure a volumetric bone mineral density (BMD) in  $\text{mg}/\text{cm}^3$  (Figure 1.4) [27, 28]. Two of the dimensions are defined by the user (100 to 200 microns). The other dimension is the slice width, defined by the X-ray and detector assembly inside the scanner. A voxel measures not only the bone material but also the porosity. Consequently the bone mineral density measured by pQCT corresponds to a structural apparent density.

The apparent density of bone measured by pQCT is composed of two parts: the bone material density and the porosity. These two parts can be measured separately using

quantitative backscattered electron imaging (qBSEi) and will be further described in the following section.

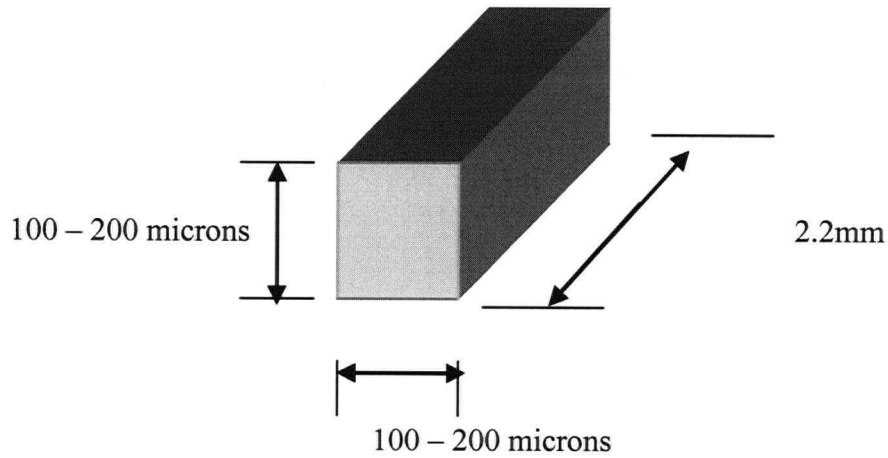


*Figure 1.4 Voxel dimensions used in pQCT measurements.*

## **1.4 Bone Mineral Content and Porosity Quantification**

Bone mineral content and porosity are two extremely important parameters that are related to bone quality. Two techniques were compared in this work regarding their quantification: contact microradiography and quantitative backscattered electron imaging [29, 30].

### **1.4.1 Contact Microradiography**

Contact microradiography is a technique based on radiographic emission [31, 32]. A thin cross-sectional slice of bone (100  $\mu\text{m}$ ) is exposed to a low energy x-ray beam for a certain time. Due to different levels of bone mineral content across the bone specimen, the image formed on the high resolution radiographic emulsion has a range of grey-levels. The grey-level depends on the radiographic absorption by the bone, which is a function of the average atomic number and the density of the local area. This technique has the advantage of

mapping the entire cross-section of bone at once. Further details about this technique, its advantages and disadvantages are presented in Appendix A.

### 1.4.2 Quantitative Backscattered Electron Imaging (qBSEi)

Quantitative Backscattered Electron Imaging is a technique used to measure the bone mineral content (BMC). Thus, it provides the bone mineral density distribution (BMDD). It can also be employed to map and quantify the porosity and its distribution across the cortical wall.

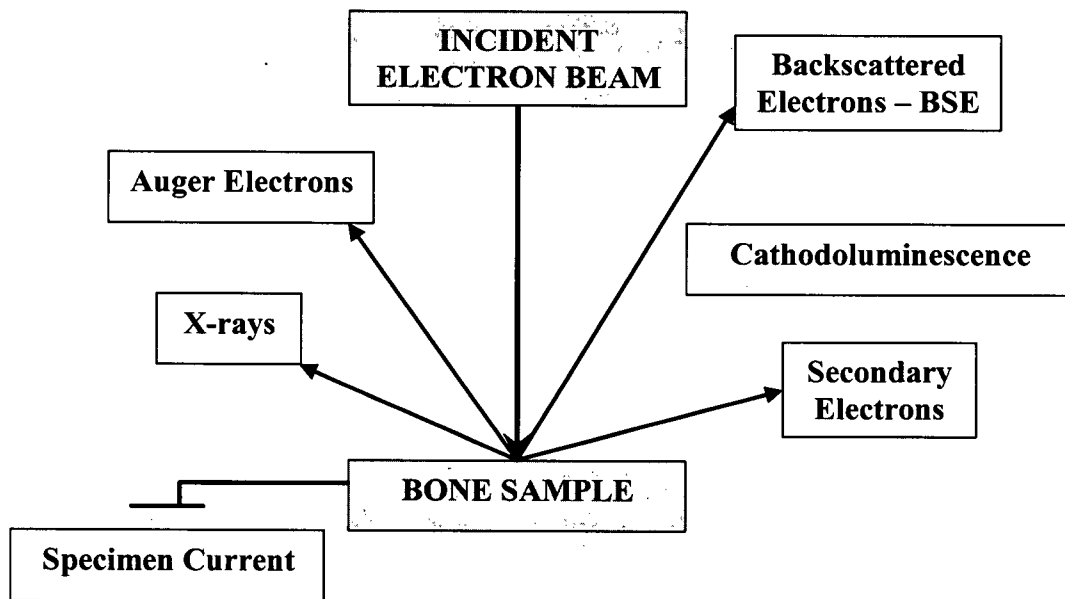


*Figure 1.5 Types of signals of SEM.*

The qBSEi technique is based on Scanning Electron Microscopy (SEM) [33]. SEM uses electrons to form an image and provides information on topography, morphology and composition. The electron beam is generated in the electron gun by a tungsten filament. The beam is accelerated and directed to the sample. Subsequent to hitting the sample surface, the incident beam generates several types of signals (Figure 1.5). The signal that is rebounded from the specimen is called backscattered electron and is the signal used in the qBSEi. The

interaction of the electron beam with the sample occurs in the first 1 – 3  $\mu\text{m}$  of the surface, depending on the incident energy beam. In order to form an image with backscattered electrons (BSE), a BSE detector is placed on top of the specimen.

The intensity of the BSE signal increases with increasing atomic number ( $Z$ ). Regions of high average atomic number appear brighter than regions of low atomic number. This principle allows the use of BSE to quantify the bone mineral content. In addition to that, BSE also provides information on bone porosity since the pores in bone appear darker in the BSE image.

#### ***1.4.2.1 qBSEi Study of Bone***

Quantitative backscattered electron imaging has been used since the early 80's to study biological tissues [34-36]. However, with the advances in nanotechnology, qBSEi has been recently employed to correlate variation in the bone mineral content with variation in the nanomechanical properties of bone tissue.

Roschger et al. [37] validated a methodology for qBSEi where carbon and aluminum were used as reference materials for backscattered electron signal grey-level calibration and osteoid and hydroxyapatite for calcium concentration standardization. From this research group, two papers correlated the nanoindentation modulus with the bone mineral content [38, 39]; however, this was done in arrays of measurements, and the microstructural factor of bone (e.g. osteonal bone versus interstitial bone) was not taken into consideration.

Ferguson et al. [40] also combined qBSEi with nanoindentation in the study of normal and osteoarthritic human femoral heads. A different methodology was adopted, using halogenated dimethacrylate reference materials. Articular calcified cartilage and the immediate subchondral bone were analyzed and the relationship between bone mineral content and elastic modulus was more distinct in the cartilage.

#### ***1.4.2.2 Cortical Bone Porosity***

Cortical bone porosity is considered as a structural parameter in bone quality [41-44]. High level of porosity, as often found in osteoporosis, weakens the structural bone. A comprehensive analysis of porosity and its distribution across the cortical wall thickness will provide valuable information on bone quality and enable us to better understand the bone apparent density provided by pQCT. The porous portion of bone includes the Haversian canals that extend the length of osteons, the lacunae that are small ellipsoidal pores approximately 20  $\mu\text{m}$  (where bone cells are located) and the canaliculi, which are very delicate channels (less than 1  $\mu\text{m}$  in diameter) branching out from the lacunae.

### **1.5 Nanoindentation Testing of Bone**

Nanoindentation is a widely used technique for determining the material properties of bone. Due to its capability of making indentations in the submicron dimension, nanoindentation allows the analysis of material properties down to an individual Haversian system and even an individual bone lamellae within an osteon. This section will present a description about the theory of nanoindentation as well as a literature review on bone studies with nanoindentation.

### **1.5.1 Theory of Instrumented Indentation Testing**

Nanoindentation is an effective and established technique to assess material properties at the submicron level [45-48]. It has evolved from conventional hardness tests, such as Vickers and Rockwell. The distinguishing feature is the fact that the contact area is calculated by measuring the depth of penetration using an indenter tip of a known geometry, while in conventional tests it is calculated from measurements of the size of the residual indent. For this reason, nanoindentation testing is also called depth-sensing indentation (DSI) or instrumented indentation testing (IIT).

Nanoindentation can be used for several different applications; however, hardness (H) and elastic modulus (E) are the most common material properties measured by nanoindentation tests. These measurements are obtained from the load-displacement curves. Viscoelastic properties like phase angle can also be measured with nanoindentation under the continuous stiffness measurement (CSM) mode [49], described in section 1.5.1.2.

Modulus of elasticity, also known as Young's modulus or elastic modulus, is the most important mechanical property defining the elasticity of a material. It defines the stiffness of a material, which is the resistance of an elastic body to deflection by an applied force. The higher the elastic modulus, the stiffer is the material.

Hardness is defined as the resistance of a solid material to permanent deformation. Hardness is the most common and simplest material property to be measured. Many instruments, such as micro-hardness, are available for this purpose.

The viscoelastic property of bone can be evaluated by the phase angle between the applied force and resultant displacement (measured with the CSM technique). This is usually expressed as loss tangent (the tangent value of the phase angle), which is defined as the ratio of the loss modulus ( $G''$ ) to the storage modulus ( $G'$ ).

#### ***1.5.1.1 Hardness and Modulus calculation***

Nanoindentation testing can be performed with either spherical or pyramidal indenters. The Berkovich indenter, a three-sided pyramidal indenter, and the most commonly employed tip, was used in this research work. The face angle ( $\theta$ ) of the Berkovich indenter is  $65.3^\circ$ . The tip radius is on the order of 50 – 100 nm. The indenter tip material is diamond. The elastic modulus ( $E_i$ ) of diamond is 1141 GPa and the Poisson's ratio ( $\nu_i$ ) is 0.07.

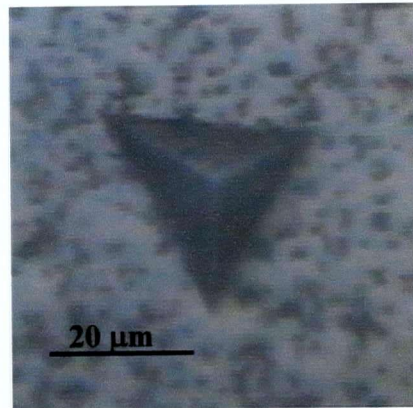


*Figure 1.6 Berkovich indent imprint.*

The projected area of contact for a Berkovich indenter is a function of the depth of penetration ( $h_p$ ) and the face angle ( $\theta$ ):

$$A = 3\sqrt{3}h_p^2 \tan^2 \theta \Rightarrow A = 24.5h_p^2 \quad (1.1)$$

Once  $h_p$  is found, the projected area of contact is calculated and the hardness computed:

$$H = \frac{P}{A} \quad (1.2)$$

As the indenter is driven into the material (loading), both elastic and plastic deformation occurs, once the indenter is withdrawn (unloading), the elastic portion of the deformation is recovered. This recovery allows the elastic properties of the material to be determined. Elastic modulus can be calculated from an analysis of the slope of the initial unloading.

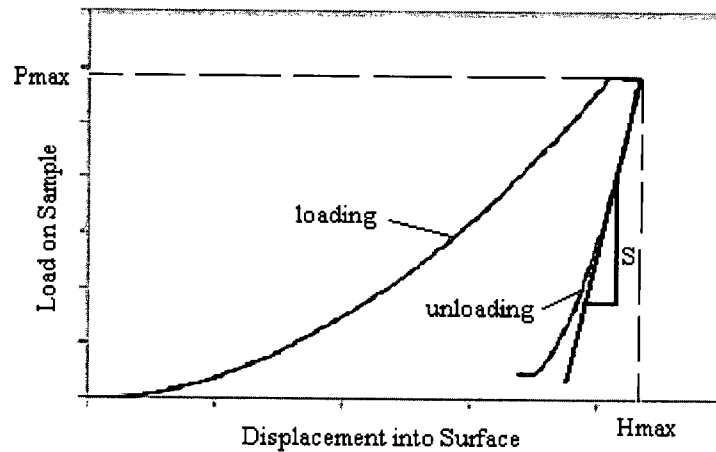


Figure 1.7 Load-displacement curve from where contact stiffness ( $S$ ) is derived.

Contact stiffness ( $S$ ) is measured from the unloading part of the load-displacement curve where  $S = dP/dh$ . Contact stiffness ( $S$ ) along with the indenter geometry  $\beta$  ( $\beta = 1.034$  for Berkovich indenter) and the projected area of contact ( $A$ ) allows the reduced modulus to be calculated:

$$E_r = \frac{(\sqrt{\pi} \cdot S)}{2\beta\sqrt{A}} \quad (1.3)$$

Knowing the Poisson's ratio of the material being tested, allows one to determine its elastic modulus through the following formula:

$$\frac{1}{E_r} = \frac{(1-\nu^2)}{E} + \frac{(1-\nu_i^2)}{E_i} \quad (1.4)$$

where: E and  $\nu$  are the elastic modulus and the Poisson's ratio for bone and  $E_i$  and  $\nu_i$  are the elastic modulus and the Poisson's ratio of the indenter tip, respectively.  $\nu = 0.23$ .

#### ***1.5.1.2 Continuous Stiffness Measurement – CSM***

Continuous stiffness measurement (CSM) is a novel technique that offers a significant improvement in nanoindentation testing. As described in the previous section, contact stiffness is determined from the slope of the unloading portion of the load-displacement curve. However, this technique allows the calculation of material properties at the maximum penetration depth only. The CSM allows the calculation of contact stiffness continuously during the loading and not just at the point of initial unloading. The CSM is accomplished by superimposing a small sinusoidal signal on top of the primary loading signal that drives the motion of the indenter. Data is obtained by analyzing the response of the system by means of a frequency specific amplifier. Some nanoindenter instruments have the option of measuring discrete unloading cycles. However, measuring the discrete unloading cycles is a slower process which may affect experimental results due to possible changes in bone water content.

A continuous stiffness measurement allows the material properties to be obtained as a function of depth penetration, which can better characterize a heterogeneous material like

human bone. In addition, the CSM allows the determination of viscoelastic properties. The storage and loss moduli of the sample can be calculated from the phase difference between load and depth signals. Consequently the loss tangent (related to phase angle) is known, thus providing important data about the viscoelastic behaviour of human bone.

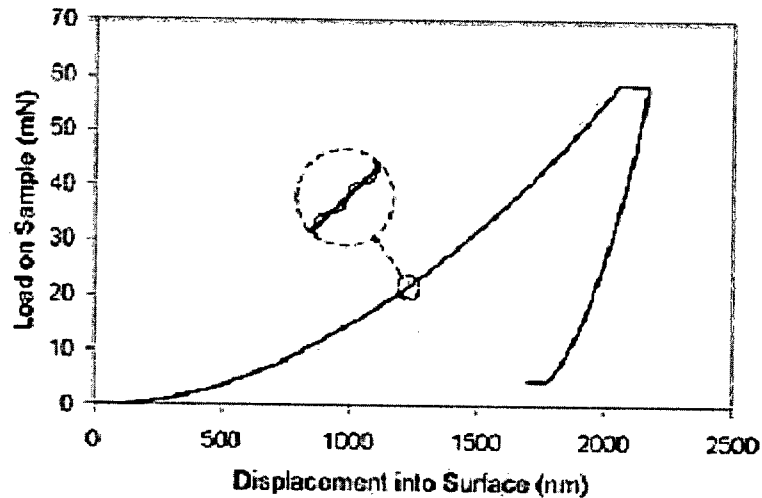


*Figure 1.8 Schematic of the CSM loading cycle.*

The two most important CSM parameters are the frequency and the amplitude of the sinusoidal signal. This will be described in section 2.1.5.

### ***1.5.1.3 Instrumentation of a Nanoindenter***

A nanoindenter instrument consists of four major components: a motorized precision table, an optical microscope, the indenter head, and a displacement sensing system. Combined, these components make nanoindentation an effective technique to measure material properties.

The test locations are selected while scanning the test surface under 100X, 400X and 1000X magnifications, using an optical microscope. After positioning the indentation locations, the

motorized precision table transports the sample between the optical microscope and the indenter. The x-y translation stage is screw-driven and has a theoretical resolution for site selection of 45 nm with a real accuracy of 0.5  $\mu\text{m}$  for a high performance table.

The indenter head transmits the load to the indenter tip. The load applied on the indenter is generated using a coil/magnet assembly, attached to the top of the indenter column, as illustrated in Figure 1.9. The range of load is of 0.1  $\mu\text{N}$  to 10 N with a theoretical load resolution of 50 nN.

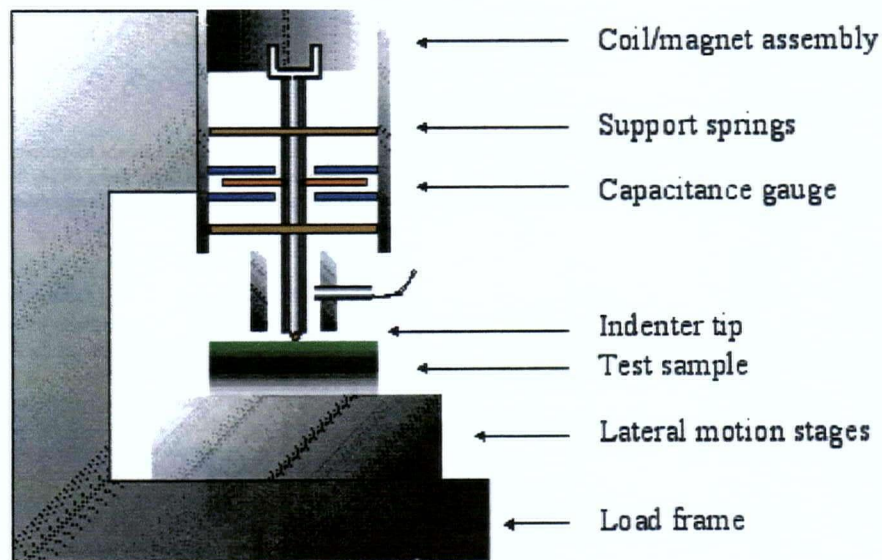


*Figure 1.9 Schematic of a MTS Nano Indenter XP instrument [48].*

The displacement sensing system consists of three capacitive plates (circular disks). The two outside plates are fixed to the head and have an opening that allows the indenter shaft to pass through. The center plate is fixed to the indenter shaft and is free to move vertically between the two other plates. The sensor is calibrated by the nanoindenter manufacturer using laser interferometry. The difference in voltage due to the displacement of the center plate gives the

actual displacement of the indenter. The range of displacement is 20 nm to 500  $\mu\text{m}$  with a theoretical displacement resolution of less than 0.01 nm.

The equipment is placed on a vibration isolation table. All of the components previously described are enclosed by a heavy wooden insulation cabinet to ensure thermal stability of the samples being tested.

### **1.5.2 Current Progress in Nanoindentation of Bone**

Microscopic properties of bone have been extensively documented in the literature. Many researchers have taken advantage of the potential of a nanoindenter to characterize material properties of bone. However, novel developments in the nanoindentation technique, such as the CSM mode, allow this research to be conducted with innovative applications. For example, under the CSM mode, it is possible to measure the viscoelastic properties of bone, as well as the depth dependent material properties.

Bone is an anisotropic material; consequently, measuring bone in the longitudinal direction does not give the same results as the transverse direction. Cowin, S.C. [50] detailed this issue by measuring the elastic modulus in both directions using human and bovine bone specimens. The elastic modulus in the longitudinal direction (17.4 GPa for human bone and 20.4 GPa for bovine bone) is larger than that in the transverse direction (9.6 GPa for human bone and 11.7 GPa for bovine bone). The characterization of cortical and trabecular bone using nanoindentation have been done by quite a few laboratories. Rho et al. [51-53] investigated the anisotropic behaviour of bone using dry human vertebrae and tibiae samples

and concluded that the modulus and hardness values are greater in the longitudinal direction than in the transverse. Furthermore, Rho et al. characterized cortical bone [54] and reported average hardness of 0.614 GPa for osteonal bone and 0.736 GPa for interstitial bone tissue using dry tibia specimens. In the same study, the average elastic moduli were 22.5 GPa for osteonal bone and 25.8 GPa for interstitial bone.

Zysset et al. [55, 56] went one step further and measured the material properties of femoral osteons and interstitial bone in wet and dry conditions. Both modulus and hardness have higher values when measured in dry conditions. Bushby et al. [57] also looked into the effect of water content in the experimental results on modulus. Using equine cortical bone, the authors reported an increase in elastic modulus from  $11.7 \pm 1.7$  GPa to  $15.0 \pm 2.2$  GPa to  $19.4 \pm 2.1$  GPa, for wet, dehydrated in ethanol, and embedded conditions (pores filled with epoxy resin), respectively. The large increases in elastic modulus caused by replacing water with ethanol and ethanol with epoxy resin demonstrate that the role of water in fine pores strongly influences the mechanical behaviour of the tissue. Rho, J.Y. and Pharr G.M. [58] reported the effect of drying on the material properties of bovine femur using nanoindentation. It was reported that drying increases elastic modulus of cortical bone by 9.7% for interstitial bone and 15.4% for osteonal bone. The setting of the experimental conditions for bone test has a great influence on the acquired results.

Because of technical difficulties, such as controlling the water content during testing and extensive time testing, very few nanoindentation tests were performed on human bone under re-wet conditions. Bone is known to be a viscoelastic material, and its water content plays an

essential role in its biological and mechanical behaviour. There is a need to conduct nanoindentation tests in human bone under re-wet conditions so that the data are more representative of *in-vivo* bone. However, there is limited information in the literature on how a specimen should be tested in wet condition with nanoindentation technology.

## **1.6 Objectives of this Research Work**

Much research in bone mechanics has been done in the last decades. With advances in technology, new perspectives can be brought to provide an enhanced understanding about bone tissue, its biology and mechanics, and especially bone fracture. For many years, nanomechanical bone research has been conducted using dried specimens. This research work will present the effect of water content on the material properties of human bone.

Empowered by the data provided by nanoindentation, a correlation will be established between nanoindentation modulus and bone mineral content measured by qBSEi. As mentioned before, such correlations have been done in arrays of measurements, without considering the microstructure of cortical bone. A microstructural differentiation between osteonal and interstitial bone will bring a clear understanding to this topic.

The pQCT data provided by our partners at the Vancouver General Hospital (VGH) was re-analyzed for the cortical bone. The comprehension of bone mineral content and porosity distribution across the cortical wall thickness is extremely important to establish a correlation with clinical evaluative tools such as pQCT.

Therefore, these are the objectives for this research work:

- The effect of water content on the elastic modulus, hardness and loss tangent;
- Establish a correlation between elastic modulus and bone mineral content;
- The modulus of elasticity distribution across the cortex;
- The bone mineral content and porosity distribution across the cortex;
- The effect of porosity and bone mineral content in the apparent density measured by pQCT.

The following chapter will present the materials and methodology used in this research work to achieve the objectives aforementioned.

### **1.7 Scope of this Research**

The scope of this research is to characterize the modulus of elasticity, bone mineral content and porosity across the cortical wall of the 25% distal medial human cadaveric tibiae. Two techniques were used for this purpose: nanoindentation and quantitative backscattered electron imaging, which allows a correlation of the aforementioned parameters with the apparent density provided by pQCT.

## **Chapter 2 Materials and Methodology**

To achieve the objectives for this research, three methodological steps were employed during the experimental period of this thesis: material property characterization by Nanoindentation, measurement of the bone mineral content by Quantitative Backscattered Electron Imaging (qBSEi), and measurement of the degree of porosity in cortical bone, also using qBSEi. This chapter presents the technical information concerning these three methodological steps as well as the procedure for pQCT – qBSEi correlation and a description of the statistical analysis used in this work.

### **2.1 Bone Nanoindentation**

A nanoindentation system (Nano Indenter XP System, MTS Nano Instruments, Oak Ridge, TN, USA) was used to evaluate the material properties of both osteonal and interstitial cortical bone. Material properties such as modulus of elasticity, hardness, and phase angle were measured with a Berkovich diamond tip (AccuTip™) using continuous stiffness measurement mode (CSM). The amplitude of the sinusoidal signal was 5 nm. The measurements were displacement controlled with penetration depth of 2000 nm for dry conditions and 3000 nm for re-wet conditions. The strain rate (loading rate / load) was set to  $0.05 \text{ s}^{-1}$ , and the allowable drift rate was set to 0.2 nm/s for increased accuracy.

Figure 2.1 presents a typical load-displacement curve for nanoindentation test, as well as the material properties evaluated with their depth dependence. The values for hardness, modulus of elasticity and phase angle were averaged from point M to point N, which are the initial and final average points respectively.

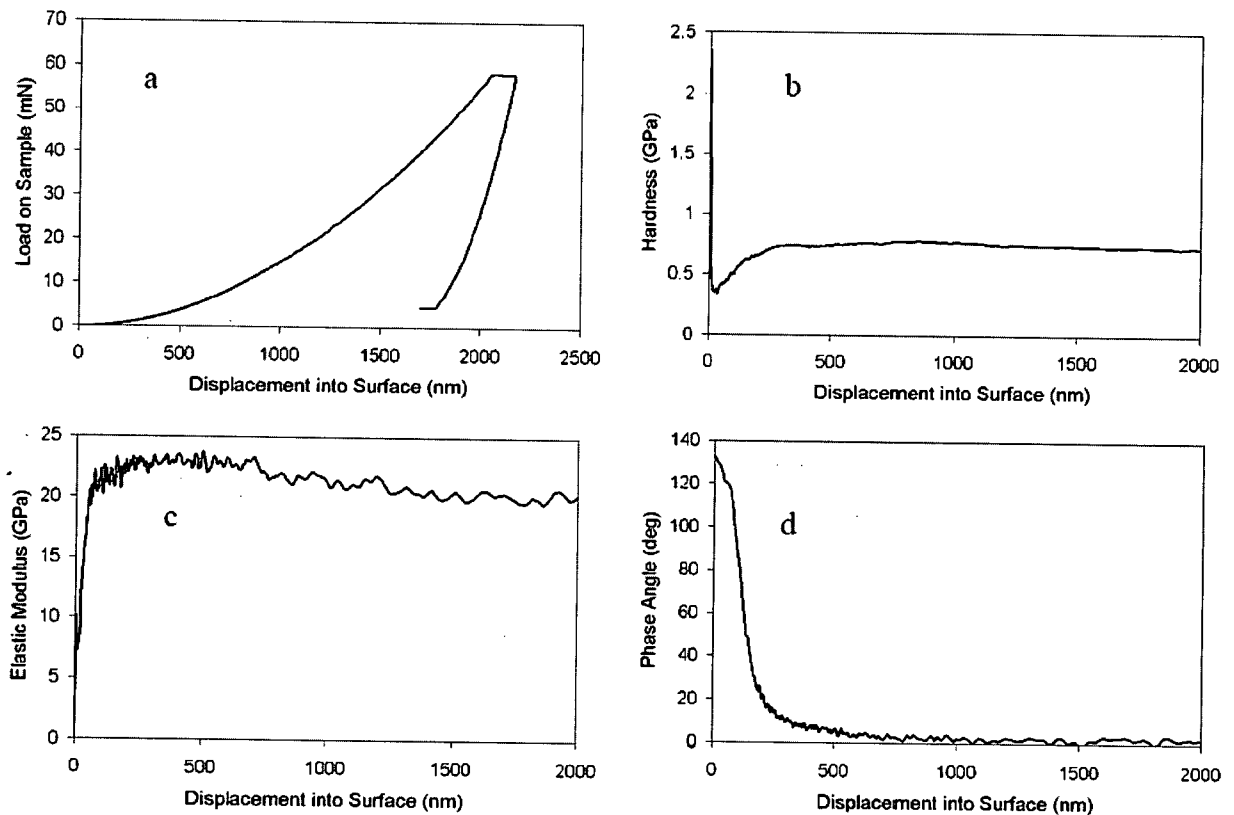


Figure 2.1 Results from a typical nanoindentation test. a) Load on sample; b) Hardness; c) Elastic modulus; d) Phase angle vs. displacement into surface.

### 2.1.1 Sample Preparation

The specimens used in this work were human tibiae from fresh unembalmed human cadavers. A total of 17 bone specimens, ranging from 67 to 88 years old, both male and female were used in this research work. They were obtained from the Body Donation Program through the University of British Columbia – Department of Anatomy. The specimens were stored at  $-20^{\circ}\text{C}$ .

The bone samples were sectioned transversely at the 25% distal end, using a diamond band saw under continuous water irrigation. The sample thickness was approximately 3 mm. The

specimens were then embedded in epoxy resin (Epothin, Buehler). The surface was ground using incremental fine grits of silicon carbide paper and polished to a mirror finish with both 6 and 1 micron diamond suspensions followed by 0.05  $\mu\text{m}$  colloidal silica. The sample preparation was finished with a vibration polishing machine (Buehler Vibromet2) for 1.5 hours using colloidal silica.

### 2.1.2 Positioning of the Nanoindentations

At the 25% distal site, the tibia sample is mainly cortical bone with a minor amount of trabecular bone. Even though trabecular bone is important to the overall strength of long bones, the focus in this work is on cortical bone.

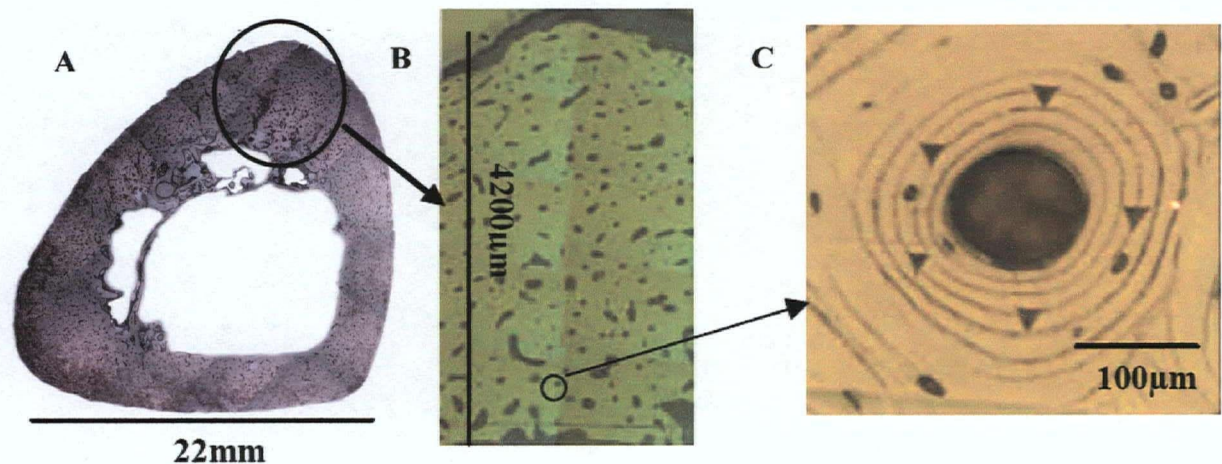


Figure 2.2 a) Cross-section of the distal tibia; b) Detailed view cortical wall – anterior site; c) Detailed view of an individual osteon with five indents.

As detailed in section 1.1 Structural Organization of Bone, the microstructure of cortical bone is composed of two parts, named osteonal and interstitial bone. Nanoindentation was used to measure the material properties from periosteum to endosteum. Selected osteons across the entire thickness of the cortical bone were measured. The analysis for osteonal

bone consisted of five indentations symmetrically distributed around the Haversian canal (Figure 2.2c). The average of these indentations represented the value for the Haversian system. In a similar manner, numerous indentations were done on the interstitial bone throughout the entire cortex wall. This analysis enabled the distribution of material properties across the cortical bone wall to be studied.

### ***2.1.2.1 Tibia Medial Aspect Testing***

The anatomy of a 25% distal tibia can be seen in Figure 2.2a. It has a triangular shape with three extremity tips (the anterior one is highlighted in the picture) and three uniform flat areas. The medial aspect is the longest one (the hypotenuse of the triangle), just left of the anterior aspect in the picture. The medial aspect was chosen due to its uniformity in shape, which may minimize the potential effect of bone geometry and bone response in the material properties.

A total of 15 samples were tested under a controlled dry condition, resulting in 1644 indentations (Table 2.1). These indentations covered both osteonal and interstitial bone. Each osteonal value corresponded to an average of five indentations in the Haversian system. All the indentations were positioned in the third lamellae from the Haversian canal to avoid a possible discrepancy in results due to different lamellae mineralization. The interstitial measurements were randomly positioned, covering the entire cortical bone thickness from periosteum to endosteum.

Appendix B presents a preliminary study on the variation of material properties according to different anatomical sites within the same bone specimen, to investigate the effect that bone response might have on material properties.

*Table 2.1 List of human medial tibia samples.*

Sample	Gender	Age	Length, mm	Side	# of indentations
1067	F	88	325	L	107
			334	R	92
1095	F	73	334	L	112
			323	R	100
1090	F	73	376	R	95
1088	M	73	406	L	107
1096	F	unknown	412	L	120
			412	R	119
1094	M	77	360	R	106
1091	M	72	363	L	108
			371	R	96
1097	M	69	373	L	126
			373	R	124
1069	M	67	350	L	112
			350	R	120

### **2.1.3 Wet Measurements**

This section describes the development of the wet testing protocol used in this research work and explains the effect of water on the indenter tip during the experimentation.

#### ***2.1.3.1 Effect of water on the Indenter Tip***

In order to keep the bone sample wet throughout the entire experiment, a small reservoir was created to surround and immerse the bone sample in a phosphate buffered solution (PBS, 0.05 M, pH = 7.2). Nanomechanical testing of bone in re-wetted conditions could potentially increase the risk of inaccuracy in the experimental results, due to the effect of water

surrounding the indenter tip. The MTS Nano Indenter XP applies load through a coil and magnet assembly and has a load resolution of 50 nN. Such a high resolution raised the concern that even a thin layer of water could affect the stability of the indenter tip.

This effect of water on the measurement accuracy was evaluated using a MTS standard fused silica sample. The sample was tested in both dry and wet conditions, and since fused silica is not a viscoelastic material, no difference in terms of material properties was expected. Any difference between these two conditions could be directly related to the effect of water surrounding the indenter tip.

Fused silica is a remarkable material in terms of its homogeneity and has an elastic modulus value of 72 GPa and a hardness value of 9 GPa. Nine indentations of 2000 nm in depth were made for both wet and dry conditions, and the results are listed in Table 2.2.

*Table 2.2 Elastic modulus and hardness for both dry and wet fused silica.*

Fused Silica	Elastic Modulus	Hardness
Dry	$72.5 \pm 0.5$	$9.7 \pm 0.1$
Wet	$72.1 \pm 0.3$	$9.4 \pm 0.1$

The water reservoir did not affect the measurement stability for the standard fused silica. However, the forces involved in the measurement of fused silica were considerably higher than those applied in human bone testing, and that might affect the stability of the indenter. For a 2000 nm penetration depth, the highest load on the fused silica sample was approximately 430 mN, while it was approximately 50 mN on human bone.

Dental composite (Z100, 3M Dental Products) is a homogeneous material with material properties similar to human bone. This material was also used to test the effect of water on the force measurement stability of the indenter tip. Consequently, the same analysis as previously described for fused silica, was performed on dental composite samples to address this issue.

A significant difference was found between dry and re-wetted conditions (Table 2.3) and additional tests were carried out to better understand this fact. Such tests were performed on specimens that were air-dried for 24 and 48 hours after the wet testing (Table 2.4).

*Table 2.3 Nanoindentation results of Z100 composite in dry and re-wetted conditions.*

	Dry 2nm	Dry 10nm	Re-wet 2nm	Re-wet 10nm
Modulus	$19.7 \pm 0.3$	$19.4 \pm 0.2$	$16.6 \pm 0.2$	$16.2 \pm 0.2$
Hardness	$0.80 \pm 0.03$	$0.81 \pm 0.02$	$0.62 \pm 0.01$	$0.59 \pm 0.01$
Phase Angle	$0.7 \pm 0.2$	$0.8 \pm 0.1$	$1.4 \pm 0.1$	$1.7 \pm 0.1$

*Table 2.4 Nanoindentation results of Z100 composite in re-dried conditions.*

	Re-dried 2nm (24hours)	Re-dried 10nm (24hours)	Re-dried 2nm (48hours)	Re-dried 10nm (48hours)
Modulus	$19.0 \pm 0.3$	$18.8 \pm 0.2$	$19.3 \pm 0.3$	$19.1 \pm 0.2$
Hardness	$0.76 \pm 0.03$	$0.76 \pm 0.02$	$0.79 \pm 0.03$	$0.78 \pm 0.01$
Phase Angle	$0.9 \pm 0.2$	$1.0 \pm 0.1$	$0.9 \pm 0.2$	$0.9 \pm 0.1$

Figure 2.3, presents the measurement curves for the elastic modulus of dental composite samples in dry, re-wetted, re-dried (24 hours), and re-dried (48 hours) conditions.

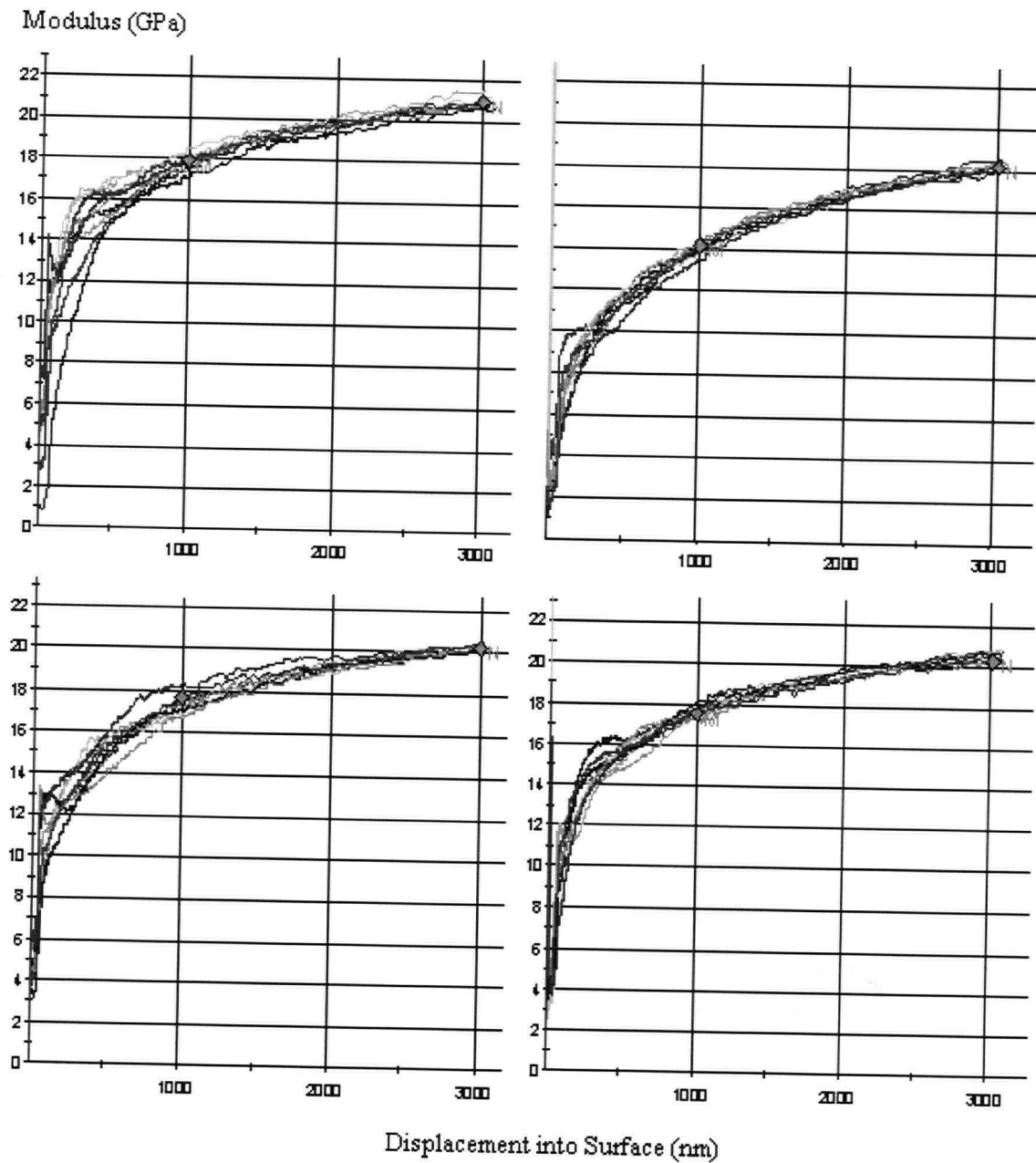


*Figure 2.3 Modulus for dental composite using 10 nm CSM amplitude (dry, re-wetted, re-dried (24 hours) and re-dried (48 hours)).*

As can be seen from these curves, there was a drop in elastic modulus of approximately 2 GPa when measured in wet conditions. In addition to this, it seems that the initial part of the curve exhibited an additional decline in material properties, which might be caused by surface hydration. Testing in re-dried conditions (after 24 hours of air-drying) revealed a

recovery of the material properties, but still 3-4% less than dry testing. After 48 hours, the material properties from the initial dry conditions appeared to be fully recovered, with a difference of about of 1%. These tests on dental composite confirmed that the indenter tip was stable throughout the entire measurement. The absorption of water by the dental composite decreased the elastic modulus and enhanced the viscoelasticity of the material.

Based on the above protocol, a complete experimental batch with 325 indentations was made in individual Haversian systems and interstitial bone. The sample was a tibia from a 73 year old female (sample 1061L). The goal was to better understand the viscoelastic behaviour of human cortical bone in a microstructural level.

#### **2.1.4 Dry Measurements**

As water content affects the material properties of bone, controlled testing conditions need to be established to test bone in dry conditions. In order to determine the right dry condition for bone testing, one tibia sample was first hydrated in a phosphate buffered solution (PBS) for 48 hours and tested six hours after the re-hydration (sample 1061R). Subsequent measurements were taken at regular intervals of 24 hours up to five days. Following this, fifteen days and thirty days measurements were also obtained.

Figure 3.5 in the Results section shows that the elastic modulus increased with air-drying time within the first 48 hours. After this period, the curve reached a plateau with little variation. Consequently, 48 hours were used as a constant period of time prior to bone testing.

## **2.1.5 CSM Frequency and Amplitude**

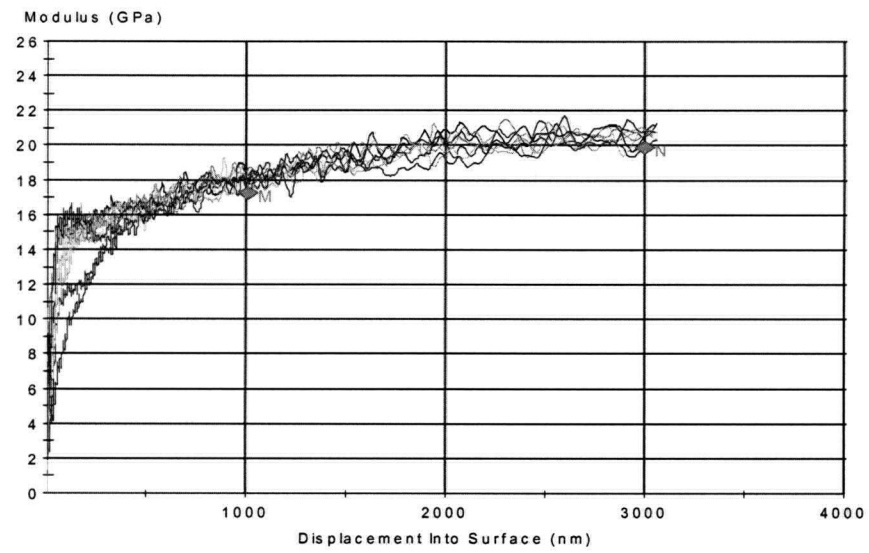
As mentioned previously, the continuous stiffness measurement technique (CSM) requires inputs of both the frequency and the amplitude of the sinusoidal load signal. Both parameters may affect measurement and need to be evaluated.

### ***2.1.5.1 CSM Frequency***

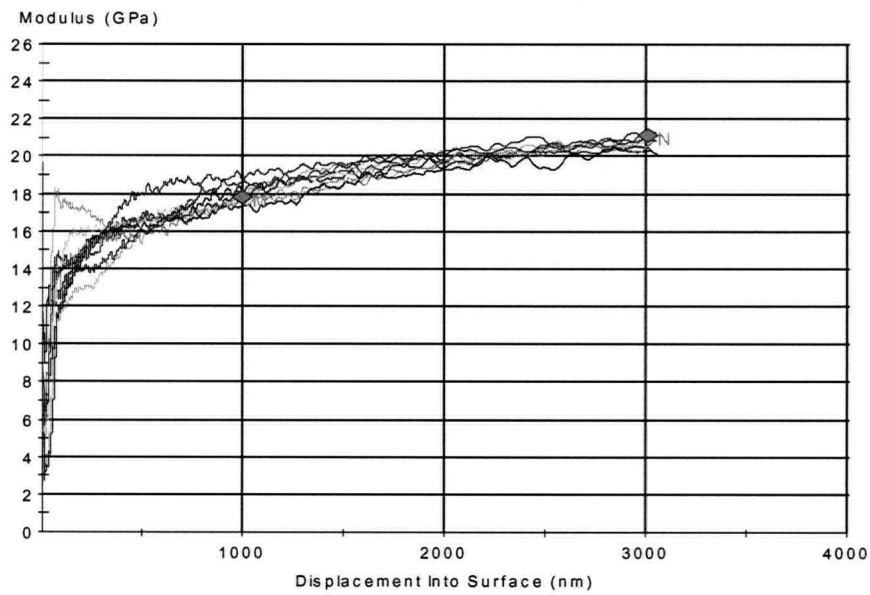
The frequencies created during human gait are fairly low (1-5 Hz). Consequently, testing bone in this range of frequency would be representative of *in-vivo* loading. A complete set of measurements was conducted with 4.5 Hz and compared to 45 Hz to investigate the effect of frequency on the material properties of bone. The frequency of 45 Hz was used to characterize the elastic modulus distribution across the cortex.

### ***2.1.5.2 CSM Amplitude***

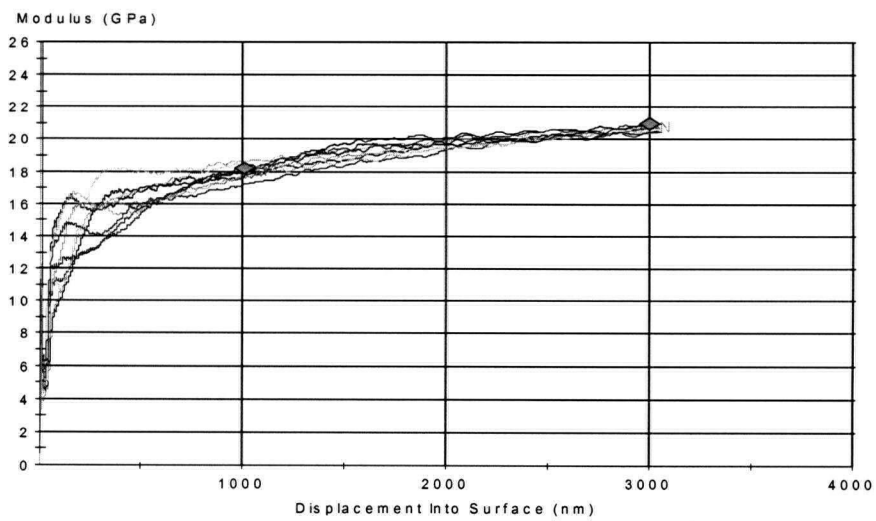
The plots of elastic modulus versus displacement into surface are shown in Figure 2.4. Three CSM amplitude values were compared on dental composite: 2 nm, 5 nm, and 10 nm. The 2nm CSM amplitude had more noise in the measurements. A slight reduction in the elastic modulus was observed when the CSM amplitude was increased from 2 nm to 10 nm. Therefore, as a compromise, 5 nm was used at the suggestion of the technical support from MTS Nano Instruments. Table 2.5 provides the average value for modulus, hardness and phase angle using 2 nm, 5 nm and 10 nm CSM amplitudes.



A



B



C

Figure 2.4 Modulus for dental composite: A) 2 nm, B) 5nm and C) 10 nm CSM amplitudes.

*Table 2.5 Modulus, Hardness and Phase Angle: 2 nm, 5nm and 10 nm CSM amplitude.*

	Dry 2nm	Dry 5nm	Dry 10nm
Modulus	19.5 ± 0.3	19.4 ± 0.3	19.3 ± 0.3
Hardness	0.80 ± 0.02	0.79 ± 0.02	0.79 ± 0.02
Phase Angle	0.8 ± 0.2	0.9 ± 0.1	0.9 ± 0.1

## **2.2 Bone Mineral Content and Porosity Quantification**

This section describes the methodology used to quantify bone mineral content and porosity of bone tissue. Quantitative Backscattered Electron Imaging (qBSEi) technique was employed in this research work.

### **2.2.1 Quantitative Backscattered Electron Imaging (qBSEi)**

An important advantage of quantitative backscattered electron imaging (qBSEi) was that the same samples that were previously polished for nanoindentation were used with qBSEi as well. Since bone is not an electrical conductive material, the samples were carbon coated by vacuum evaporation (JEE-4B Vacuum Evaporator, JEOL – Japan Electron Optics Laboratory Co. Ltd., Tokyo Japan) to create a conductive surface layer to avoid charging during the scanning electron microscopy session. Images of the medial site were taken using a scanning electron microscope (Hitachi S-3000N, Hitachi Ltd., Tokyo, Japan). The settings of the SEM instrument for qBSEi are noted below.

#### **2.2.1.1 Calibration of the BSE signal**

The atomic number dependence of the BSE signal was calibrated before any bone mineral quantification. Two standard materials were used for this purpose: carbon (C, Z = 6) and

aluminum (Al,  $Z = 13$ ). The linearity of the atomic number versus BSE grey-level curve was evaluated with magnesium fluoride ( $\text{MgF}_2$ ,  $Z = 10.17$ ) and hydroxyapatite (HA,  $Z = 14.43$ ). HA is similar to the mineral present in human bone and was also used in the standardization step.

The calibration curve provided a correlation between the BSE grey-level (GL) and the atomic number ( $Z$ ) as seen in Figure 2.5. The atomic number dependence was a linear function with  $R^2 = 0.9999$ .

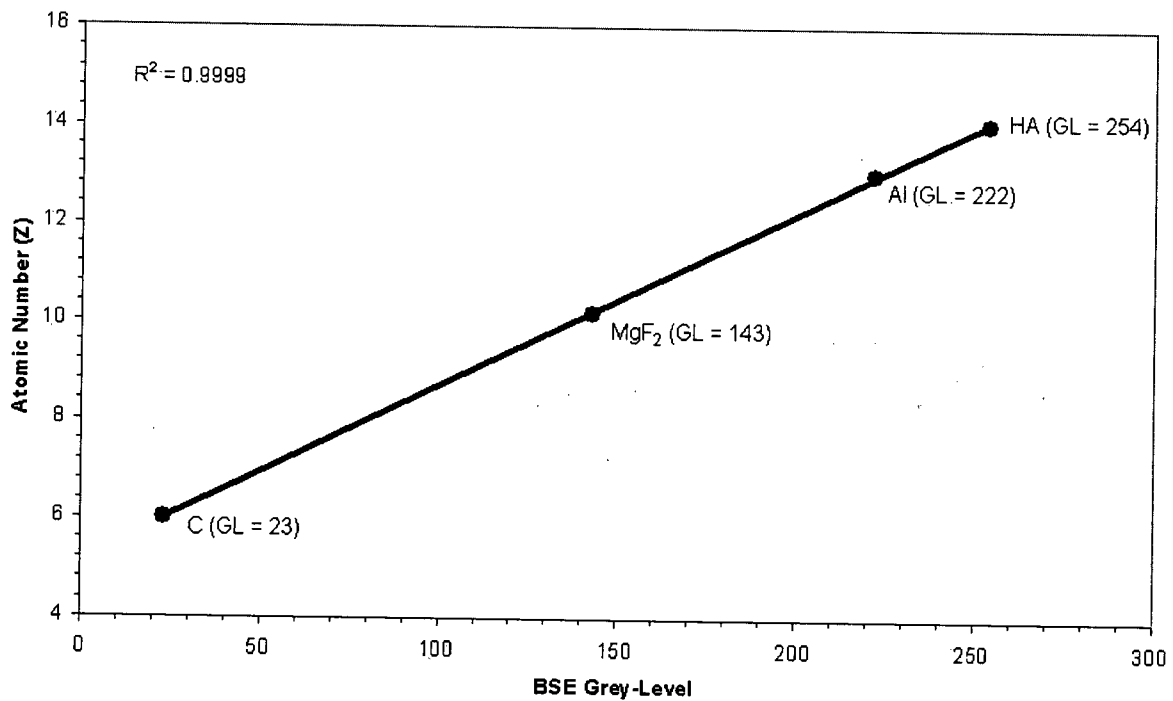


Figure 2.5 Calibration of BSE signal.

Contrast and brightness were adjusted so that the grey levels of carbon and aluminum were separated from each other ( $\sim 25$  for C and  $\sim 225$  for Al) to provide a larger range for measurements of bone. The stability of the SEM equipment is critical to acquire reliable

quantifications, and the probe current was monitored throughout the entire SEM analysis session.

The calibration was a critical step for Quantitative Backscattered Electron Imaging. The settings of the scanning electron microscope were as follows:

- Electron beam energy → 20 kV
- Working Distance → 15 mm
- Magnification → 100X
- Objective Aperture → 2
- Current → controlled
- Contrast and brightness → fixed

#### ***2.2.1.2 Standardization of the BSE signal***

The standardization provides a correlation (equation in Figure 2.6) between BSE grey-level (GL) and the calcium content of the sample (Wt% Ca). This curve is established using the two major components of bone: osteoid (bone matrix) and hydroxyapatite (bone mineral). Osteoid was prepared using the same tibia cortical bone. After being fixed in 10% buffered neutral formalin, the bone specimen was demineralised for 5 weeks using a 4% EDTA solution (ethylene diamine tetra-acetic acid). Hydroxyapatite contains 39.86 wt % of calcium in its structure, while osteoid (after demineralization) has less than 0.2 %. For calculation purposes, it was taken as 0 Wt % of calcium.

The grey-level for osteoid was very similar to the carbon reading. Carbon and osteoid were measured under four different settings of contrast and brightness and the average percentage difference in grey-level between both of them was less than 3%. This is due to the composition of the collagen fibres, which are mainly carbon based. Consequently, the carbon BSE signal reading was also applied to osteoid in the standardization curve. Figure 2.7 shows BSE images as the one used for calibration and standardization (these are 200X magnification for illustration purposes). It is remarkable the similarity between the grey-level of osteoid and carbon.

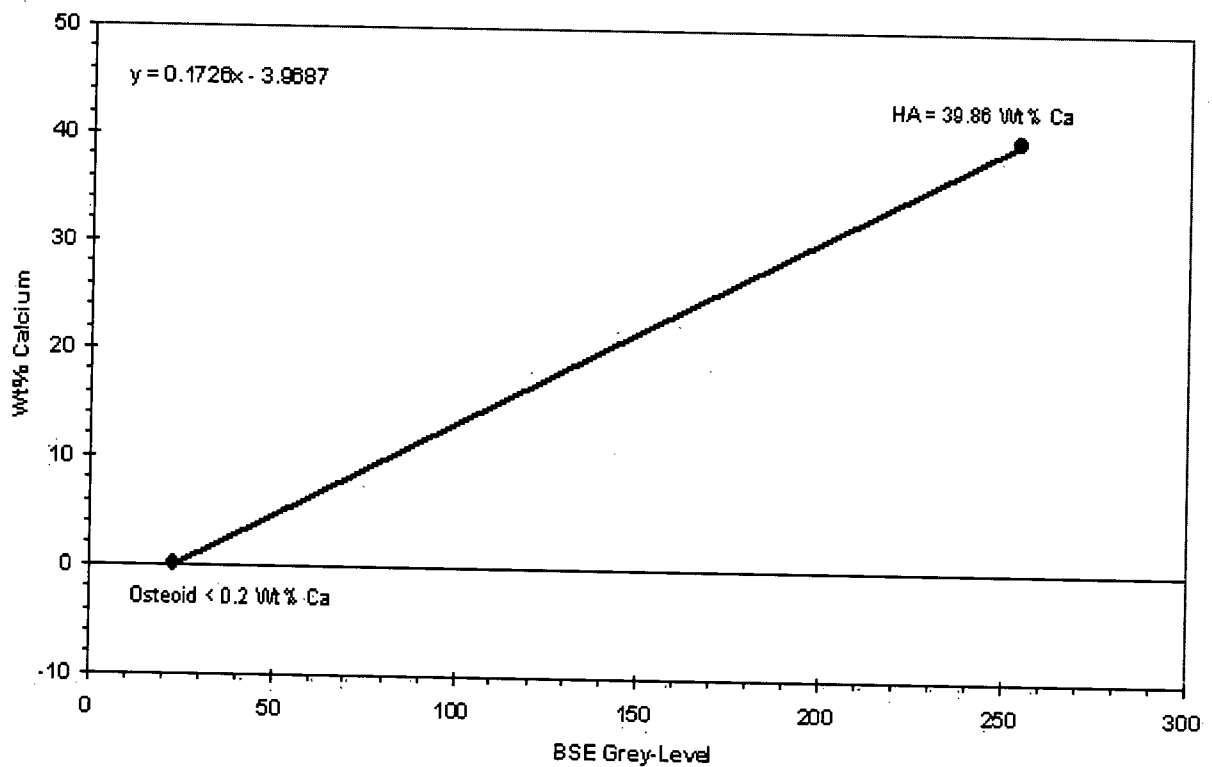


Figure 2.6 Standardization of BSE signal.

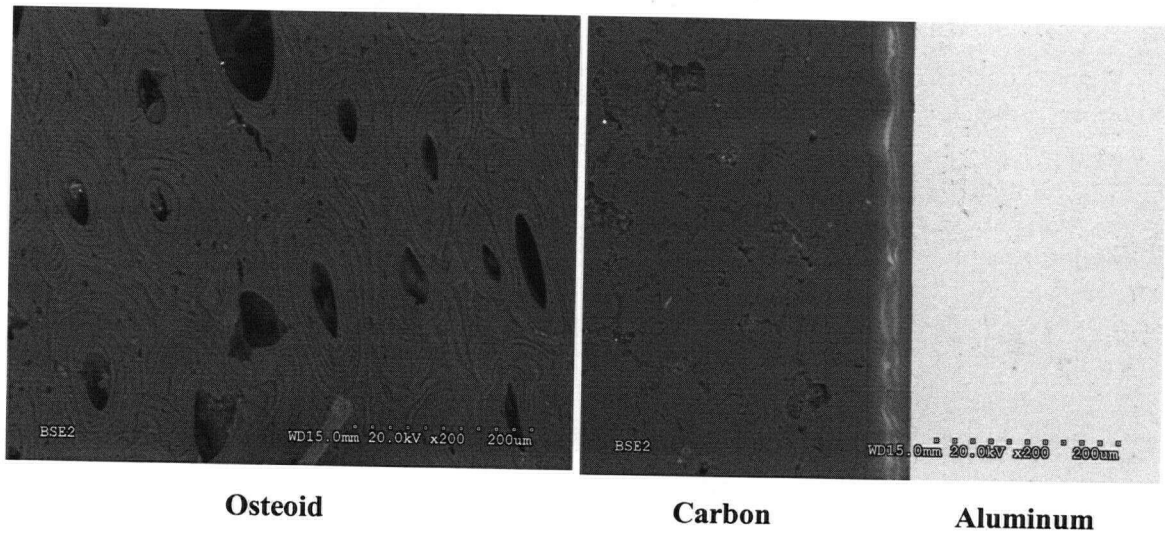


Figure 2.7 Osteoid, carbon and aluminum standard samples used in qBSEi technique.

### 2.2.1.3 BSE Image Grey-level Analysis

The digital image processing and analysis was performed using Adobe Photoshop image analysis software and Microsoft Excel with custom-made routines. Grey-level histograms (Figure 2.8) were used to read the quantitative backscattered electron images of bone (Figure 2.9) and allow subsequent calculations of calcium content.

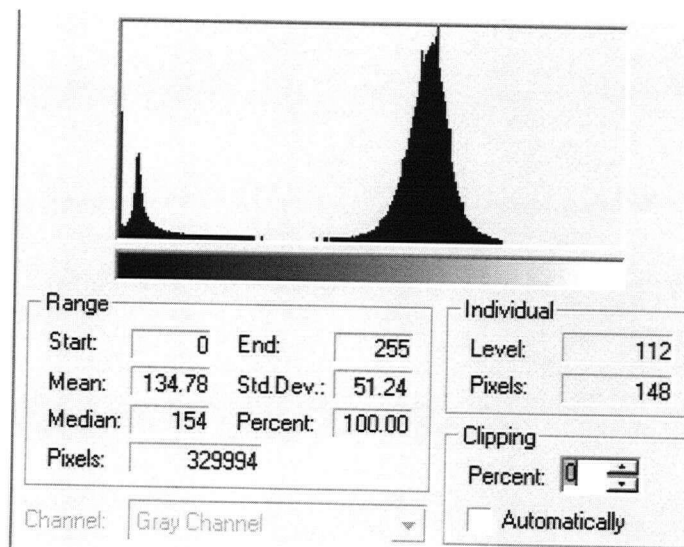
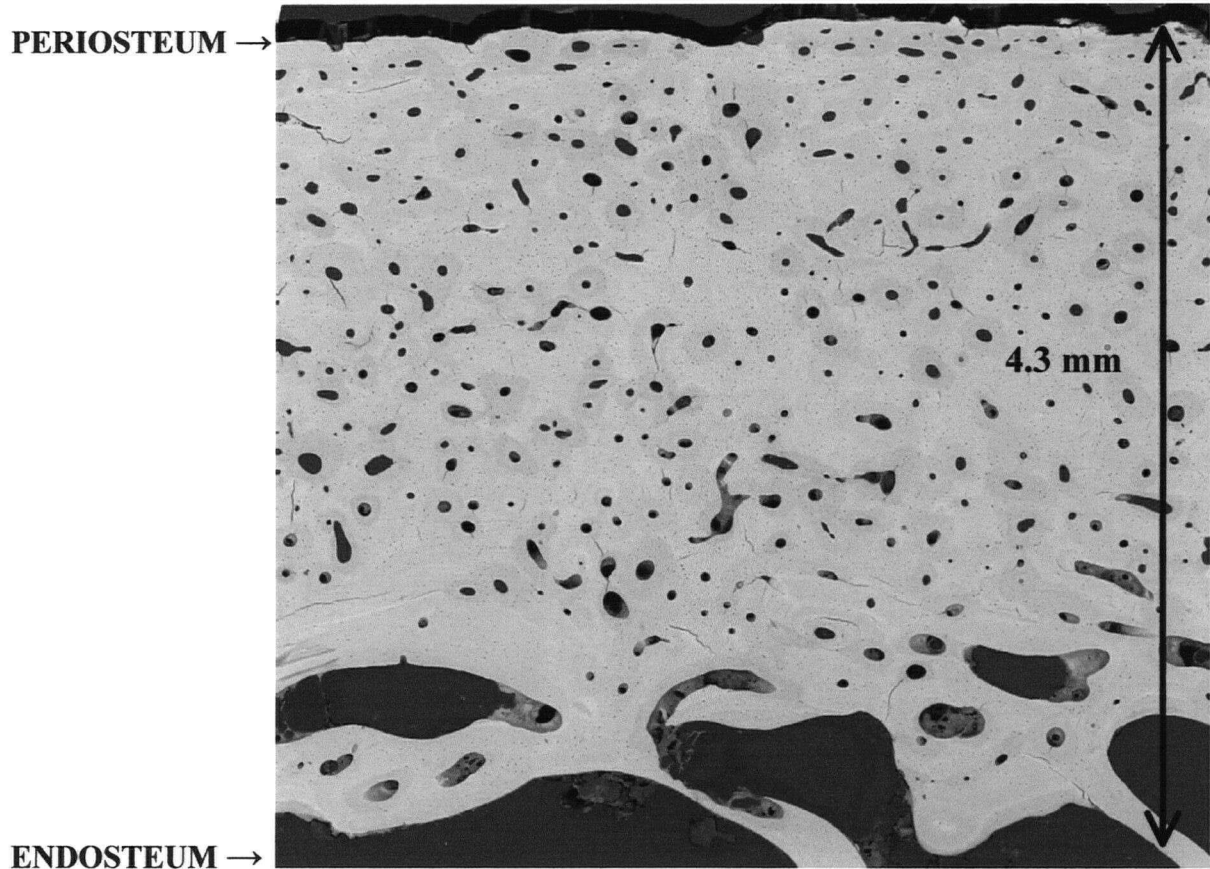


Figure 2.8 Grey-level histogram for image analysis.

The indentation imprints, from previous nanoindentation testing (Figure 2.10), were still evident on the samples. Therefore, the grey-level histograms were taken in the bone surrounding the imprints.

Subsequently, the grey-level measured by the histograms were converted into weight percentage (Wt %) of calcium using the standardization method described previously. This analysis provided the distribution of calcium content across the cortical wall and a correlation with material properties measured by nanoindentation.



*Figure 2.9 qBSEi of medial aspect of tibia 1096L.*

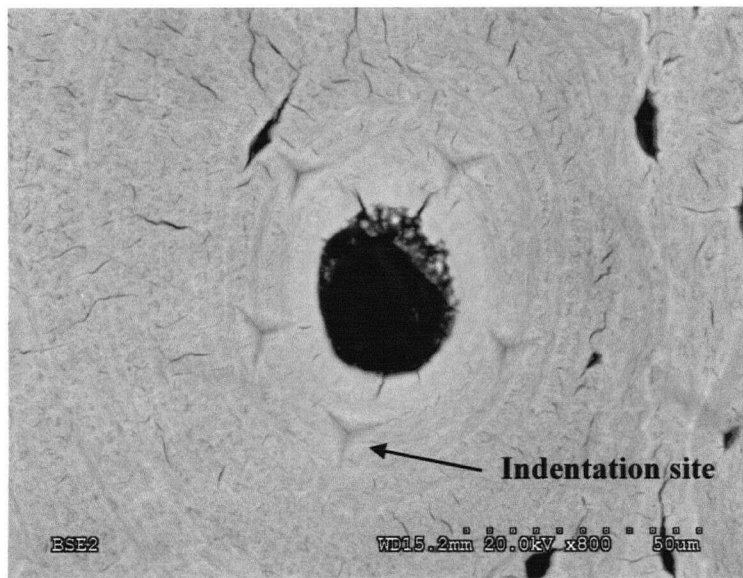


*Figure 2.10 Osteonal indentations (total 5; one labelled) in an image used for bone mineral content analysis.*

### **2.2.2 Porosity Analysis**

The Backscattered Electron Imaging (BSEi) technique was also used for porosity analysis as it gives an excellent grey-level contrast for further image analysis. In order to cover the entire medial aspect with fewer images a magnification of 45X was used. The images were merged together and had their porosity distribution across the cortex evaluated.

The image analysis software Clemex Vision Professional Edition with custom-made routines was used to analyze the degree of porosity within the cortical bone. A grey-level threshold was used to differentiate porosity from mineralized bone matrix. Porosity was defined as the percentage area of pores (i.e. bone cells (osteocytes), Haversian canals, and clusters Haversian canals). Porosity was measured from the BSE image throughout the entire medial cortical wall thickness, which was divided into five subregions (0-20%, 20-40%, 40-60%, 60-80% and 80-100%, where 0-20% is the periosteal zone and 80-100% is the endosteal

zone) to facilitate the correlation with apparent density provided by pQCT data. Figure 2.11, above, presents the BSE image for specimen 1097L and the threshold defining porosity and mineralized bone matrix.



*Figure 2.11 Medial aspect of sample 1097L (top) and threshold for porosity quantification (bottom). Horizontal length – 3350  $\mu\text{m}$ .*

### **2.3 pQCT – qBSEi Correlation Procedure**

The five samples used for bone mineral content and porosity analyses (1067L, 1069L, 1095L, 1096L and 1097L), were also used to establish a correlation between these two parameters aforementioned and the bone apparent density provided by pQCT. The pQCT data was obtained by Danmei Liu at the Vancouver General Hospital (VGH), using the Stratec XCT2003 (XCT2000, Stratec GbmH, Pforzheim, Germany). Combining bone

material density with its level of porosity enables the apparent density provided by pQCT to be better understood and quantified. Consequently it can be determined if either porosity, bone mineral content or perhaps a combination of both is influencing the bone density reading provided by pQCT.

Figure 2.12 shows the bone density reading provided by pQCT for the tibia sample 1096L. Five profiles were measured across the medial aspect of the tibia, covering the entire cortex wall thickness from periosteum to endosteum. The endosteal zone corresponds to the zero distance.

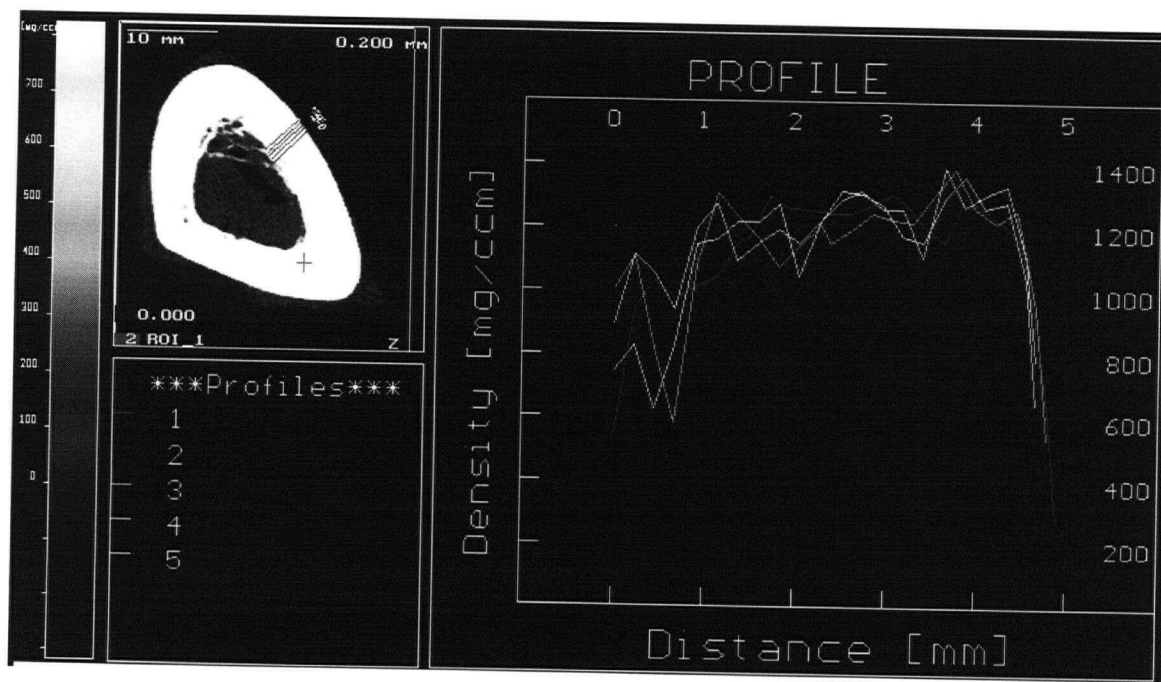


Figure 2.12 Bone density reading provided by pQCT – tibia sample 1096L.

The medial cortex thickness from the calibrated qBSEi was divided into five equal zones (0-20%, 20-40%, 40-60%, 60-80% and 80-100%, where 0-20% is the periosteal zone and 80-100% is the endosteal zone). The mean grey-level was measured for each zone and the

calcium content calculated from qBSEi. Therefore, the bone mineral density (BMD) can be determined, with an assumption that bone has a constant density of 1850 mg/cm<sup>3</sup> and that hydroxyapatite is composed of 39.7% of calcium. BMD is here called  $\rho_B$  and is calculated as follows:

$$\rho_B = \frac{Wt\%Ca \times 1850}{39.7} \quad (2.1)$$

Through a rule of mixture, porosity can be included in the calculation and bone density ( $\rho_T$ ) determined:

$$V_T \cdot \rho_T = V_{Por} \cdot \rho_{Por} + V_B \cdot \rho_B \quad (2.2)$$

where, V is the volume and  $\rho$  is the density. T is related to the total (porous bone structure), Por is related to the porosity and B is related to the bone material and. Since,  $\rho_{Por} = 0$  the equation becomes:

$$\rho_T = \left(1 - \frac{V_{Por}}{V_T}\right) \cdot \rho_B \quad (2.3)$$

The pQCT data, as provided in Figure 2.11, was also divided into five equal segments to provide the same base of comparison with bone mineral content and porosity. The sensitivity factor reveals how these two parameters affect bone densitometry as provided by pQCT.

## 2.4 Statistical Analysis

T-test, ANOVA and linear regressions were used to statistically analyze the data in this research work.

### **2.4.1 Basic Material Properties t-test**

The basic material properties of bone were statistically analyzed with t-test. The t-test assesses whether the means of two groups are statistically different from each other. For each material property (modulus, hardness and loss tangent) two t-tests were used, one comparing dry and wet at 45 Hz, and another one comparing 4.5 Hz and 45 Hz in wet condition. A Bonferroni correction ( $n = 2$ ) was applied to the threshold of P-value (0.05), resulting in a new threshold of 0.025. This analysis was carried out in an osteonal tibia from a female 73 years old (specimen 1061L) in both dry and re-wet conditions using 4.5 and 45 Hz CSM frequency.

### **2.4.2 Modulus and Bone Mineral Content Distribution across Medial Cortex**

Both elastic modulus distribution and bone mineral content distribution across cortical tibial bone were statistically analyzed. A two-way repeated measures analysis of variance (ANOVA) was used to calculate the P-value, which represents the significance of the observed data [59, 60]. The P-value is a probability, with a value ranging from zero to one. A small P-value means that the difference between samples is unlikely to be a coincidence. The threshold of P-value was set to 0.05. The factors used in this analysis were: microstructure (osteonal or interstitial) and cortical wall location (percentage distance from periosteum). A post-hoc Newman-Keuls analysis was also used to calculate the P-value for paired variables.

The analysis for elastic modulus was performed on 13 specimens. Samples 1069R and 1069L were not included because of the abnormal behaviour; however they are extremely important

in this research work. The statistical analysis for bone mineral was performed on 4 specimens (1067L, 1095L, 1096L and 1097L).

### **2.4.3 Linear Regression and Correlation**

The correlation between x and y was detailed by a linear regression and correlation analysis. Linear regression is the process of finding the best straight line that fits the data and follows the equation:  $y = m x + b$  (where m is the slope of the curve and b is the intercept in the y-axis). The Pearson product-moment correlation coefficient (R) gives a measure of the linearity. It ranges from -1 (inverse correlation) to +1 (perfect correlation). The P-value was also calculated and provides a measure of how good the linear regression fits the data.

The linear regression was used for the following correlations:

- Wet – dry elastic modulus;
- Elastic modulus – calcium content;
- pQCT density – porosity;
- pQCT density – calcium content;
- pQCT density – calculated density.

## Chapter 3 Results

### 3.1 Basic Material Properties of Bone

Material properties of bone depended on both bone conditions and the testing parameters. For instance, both water content of bone and CSM frequency had an effect on the material properties measurements.

The results presented in Figure 3.1 show the three basic material properties of bone measured in this research work, namely modulus of elasticity (E), hardness (H) and phase angle that allowed the loss tangent ( $\tan \delta$ ) to be calculated. They were acquired in both dry and re-wet conditions. Bone in re-wet conditions provided a better estimate of the material properties of *in-vivo* bone. *In-vivo* has an optimal water content in its microstructure.

The data was acquired using depth-dependence measurements with continuous stiffness measurement (CSM) and Figure 3.1 shows the modulus of elasticity, hardness and phase angle measured to a penetration depth of 2000 nm in re-wet conditions. These curves correspond to the Haversian system seen in Figure 2.2c.

As the indenter tip was driven into the material bone, a small oscillation was observed in the material properties of bone. This is especially observed in the modulus of elasticity, where a drop of about 5% was found from the depth of 400 nm to 2000 nm.

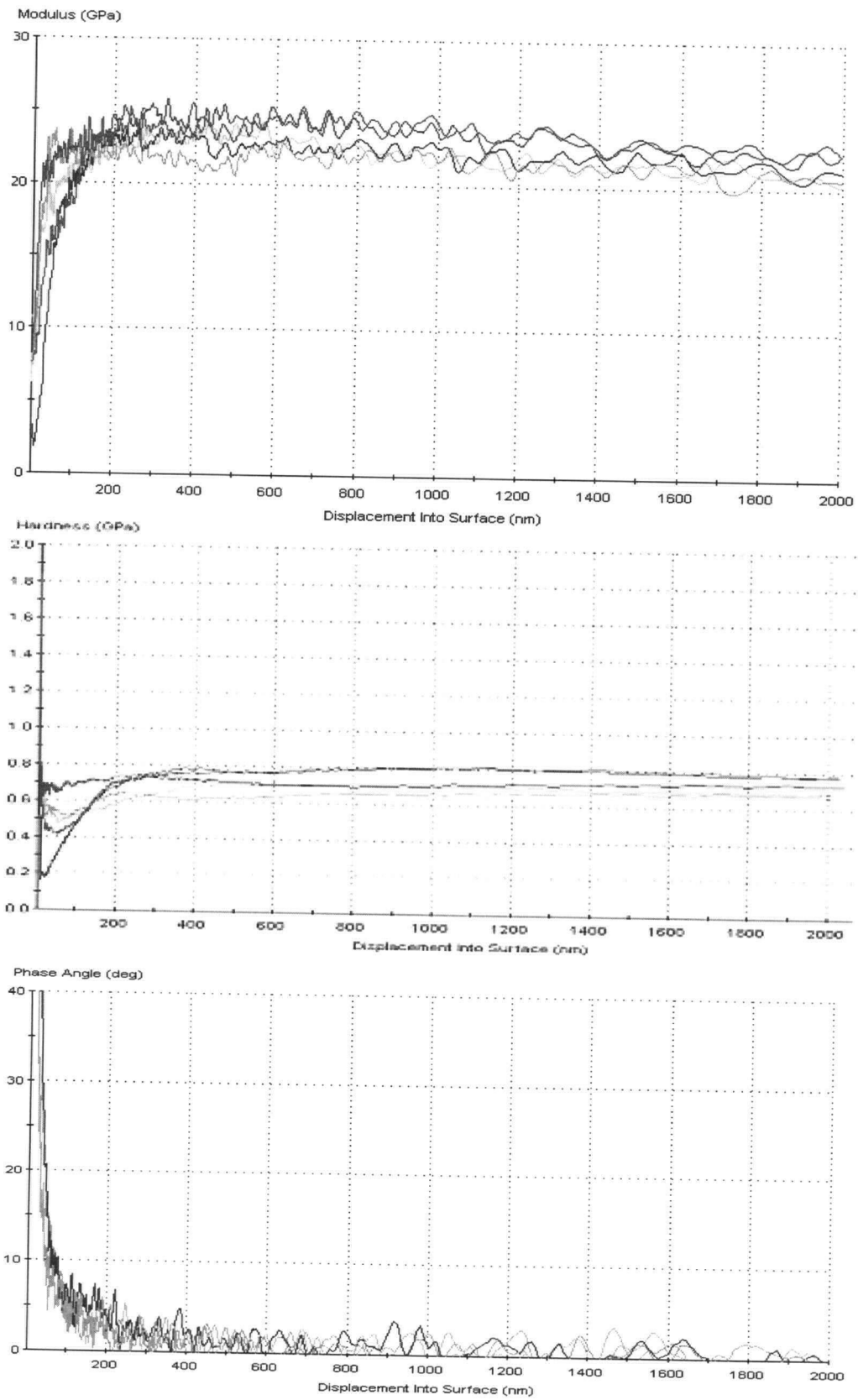


Figure 3.1 Modulus, Hardness and Phase angle with depth-dependence measurements.

### 3.1.1 Effect of Water Content, Harmonic Frequency, and Air-Drying Time

This section aims to demonstrate the effect of water content, air-drying time and the harmonic frequency used by CSM mode on the material properties measured by nanoindentation. Figures 3.2 to 3.4 illustrate the effect of water content and harmonic frequency on the elastic modulus, hardness and loss tangent, respectively.

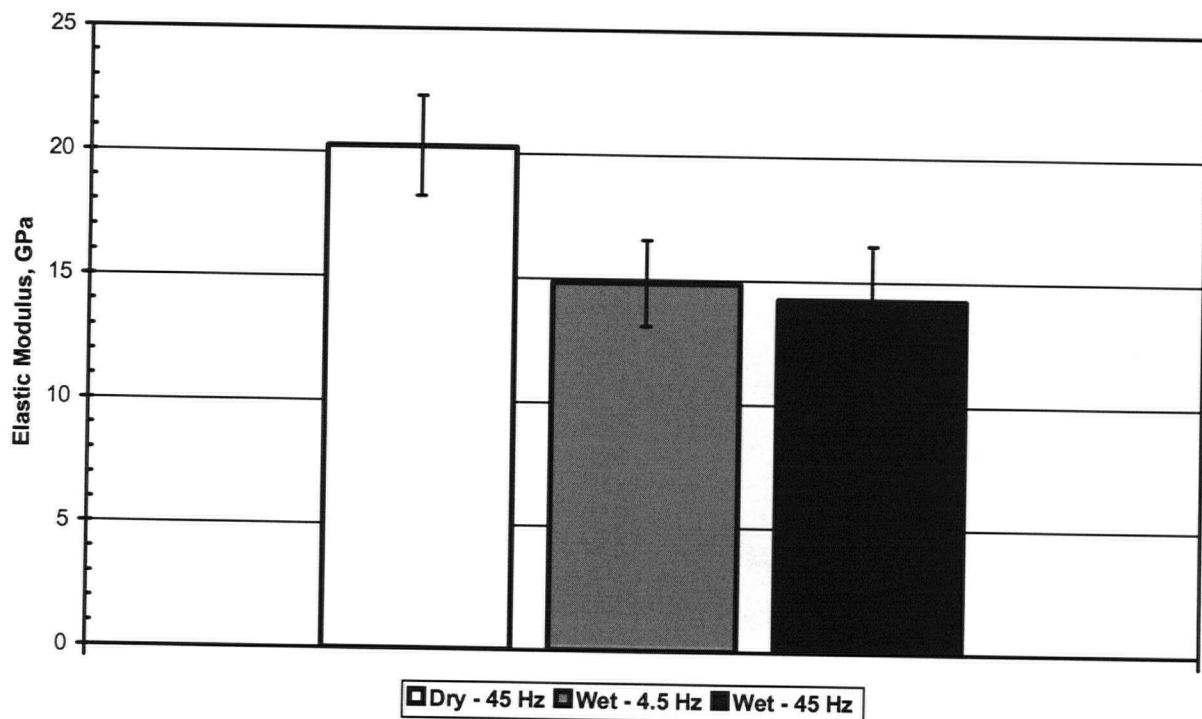


Figure 3.2 Effect of water content and harmonic frequency on Elastic Modulus.

#### 3.1.1.1 Water Content Effect on Modulus, Hardness and Phase Angle

Water had a dramatic effect on the material properties of bone. After rehydration, the measured elastic modulus and hardness in osteonal bone (CSM frequency constant – 45 Hz) decreased considerably. The average elastic modulus for osteonal bone during wet measurements  $14.3 \pm 2.2$  GPa was 29.7% lower than the average for dry measurements  $20.3 \pm 2.0$  GPa ( $P < 0.0001$ ) (Figure 3.2). The average hardness for osteonal bone in wet

conditions  $0.31 \pm 0.08$  GPa was less than half the value of the dry bone  $0.67 \pm 0.07$  GPa ( $P < 0.0001$ ) (Figure 3.3). Water also had a fundamental effect in the viscoelastic behaviour of bone. Bone in dry state had a value of loss tangent as low as 0.009, indicating a more elastic nature. After rehydration, osteonal bone presented a more viscoelastic behaviour, as the loss tangent increased to 0.036 at 45 Hz ( $P < 0.0001$ ) (Figure 3.4).

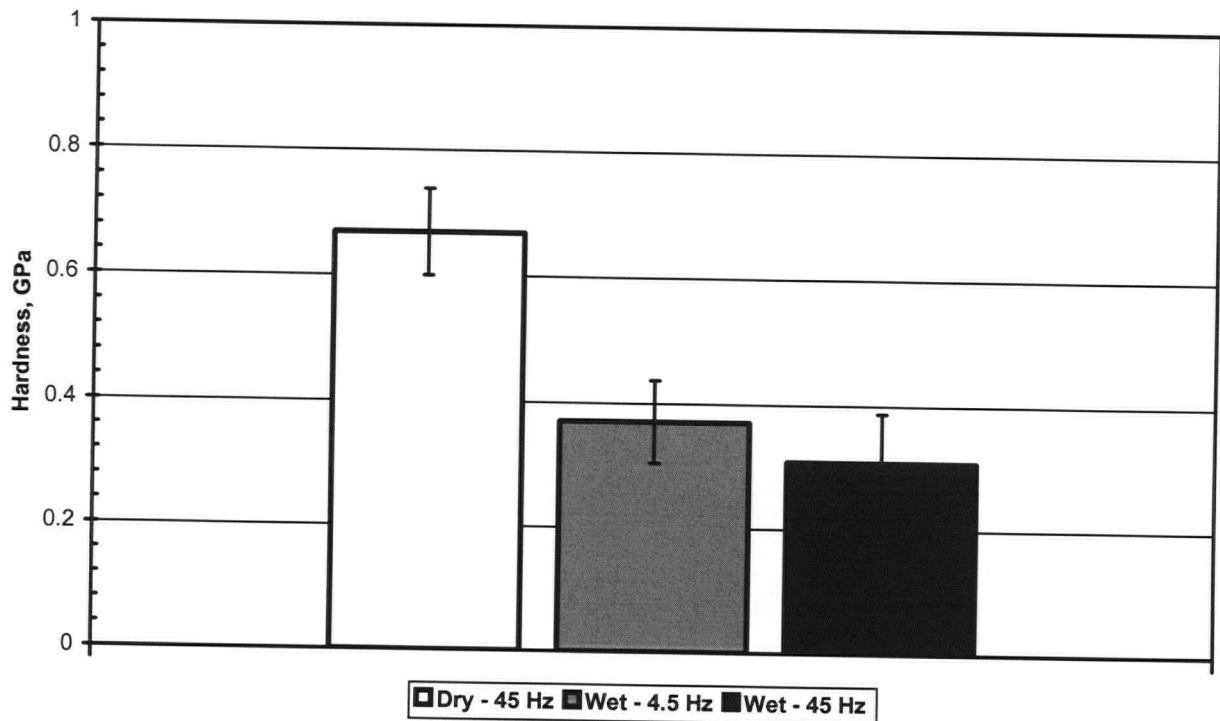


Figure 3.3 Effect of water content and harmonic frequency on Hardness.

### 3.1.1.2 CSM Frequency Effect on Modulus, Hardness and Phase Angle

The CSM harmonic frequency had a major effect on the viscoelastic behaviour of bone (loss tangent); however, no significant effect on elastic modulus and hardness was observed. The average elastic modulus for osteonal bone at 4.5 Hz CSM harmonic frequency  $14.9 \pm 1.7$  GPa was 4.1% higher than the average for 45 Hz  $14.3 \pm 2.2$  GPa ( $P = 0.64$ ) (Figure 3.2). The average hardness for osteonal bone at 4.5 Hz CSM harmonic frequency  $0.37 \pm 0.07$  GPa was

17.0% higher than the average for 45 Hz  $0.31 \pm 0.08$  GPa ( $P = 0.07$ ) (Figure 3.3). These results were almost negligible when compared to the frequency effect on viscoelastic properties of bone. Increasing the harmonic frequency from 4.5 Hz to 45 Hz dramatically decreased the loss tangent more than half, from 0.075 to 0.036 ( $P = 0.02$ ) (Figure 3.4). The frequency dependence confirmed the viscoelastic nature of wet-bone.

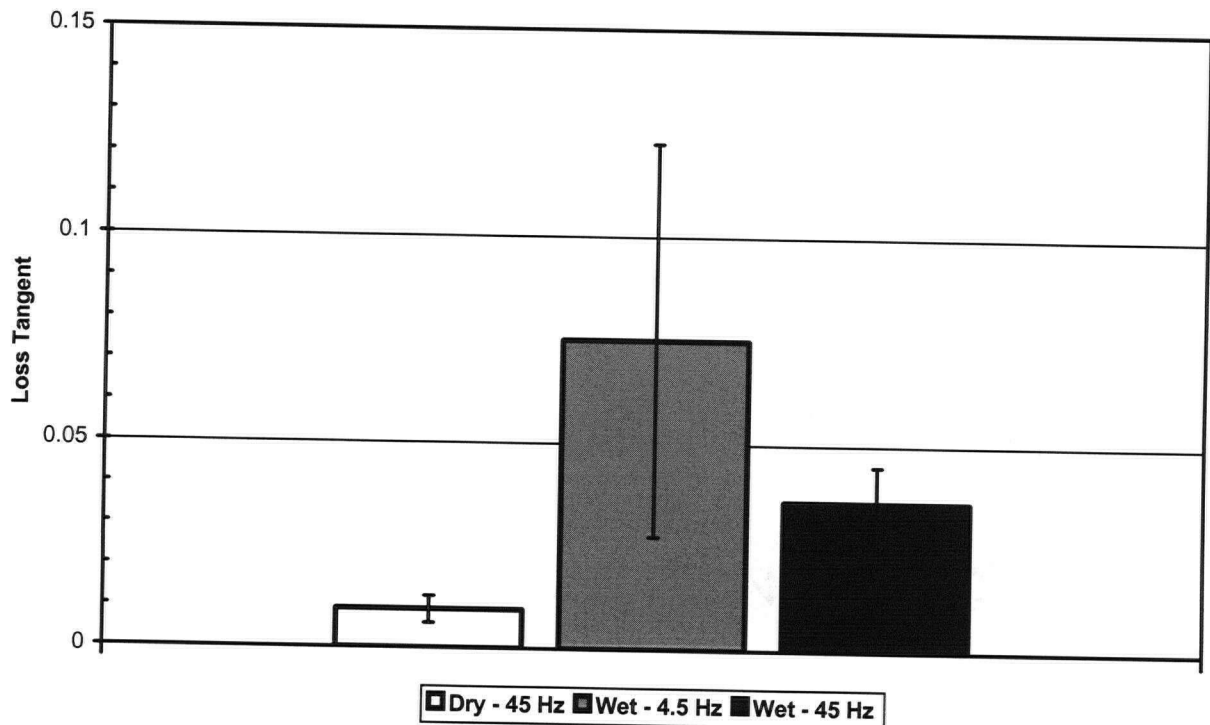


Figure 3.4 Effect of water content and harmonic frequency on Loss Tangent.

### 3.1.1.3 Air-Drying Time Effect on Modulus, Hardness and Phase Angle

Another important parameter when measuring material properties of bone is the subsequent air-drying time after rehydration. As seen in Figure 3.2, there was a considerable drop in elastic modulus from dry to wet measurements. To monitor the change in material properties with drying time and to seek a stable testing condition, the same bone was first rehydrated in

phosphate buffered solution (PBS) at pH 7.2 (equivalent to body fluid pH) for 48 hours and then tested in air at different time intervals.

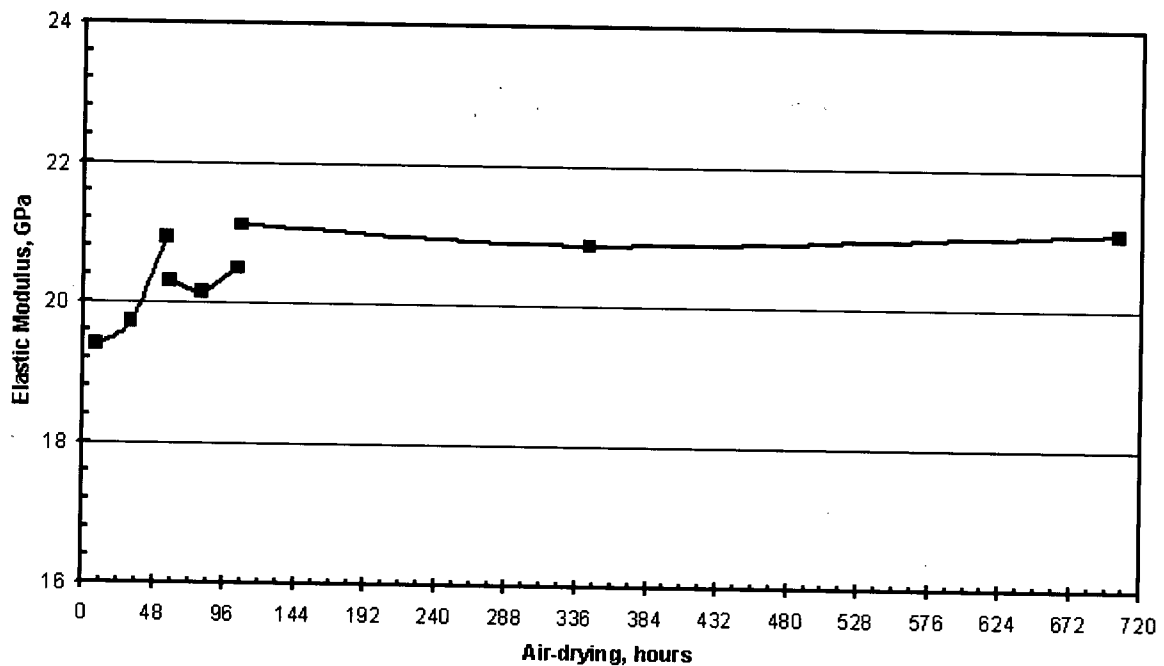


Figure 3.5 Effect of air-drying (time) on elastic modulus.

A group of five large osteons were selected and indented over three consecutive days. The indentation depth was slight smaller (1500nm) and only four indentations were made in each day. In the first 48 hours, there was a clear increase in elastic modulus as bone dried out (Figure 3.5). After 48 hours a relatively stable plateau was achieved. The discontinuity in the graph was due to measurements in different osteons. It can be concluded that the measured average modulus of elasticity achieved a stable value at 48 hours of air-drying. Therefore, to avoid discrepancy in results due to water content present in the bone, the investigation was carried out with 48 hours of bone rehydration followed by 48 hours of air drying to assure the same testing conditions for both osteonal and interstitial bone. These results will be presented in the section 3.2 Modulus of Elasticity Distribution

### 3.1.2 Wet-Dry Correlation

A correlation between the two experimental conditions (dry and re-wet bone) is presented in this section. Such correlation allows the data acquired in dry conditions to be reprocessed, taking into account water content of bone, thus resulting in re-wet bone conditions.

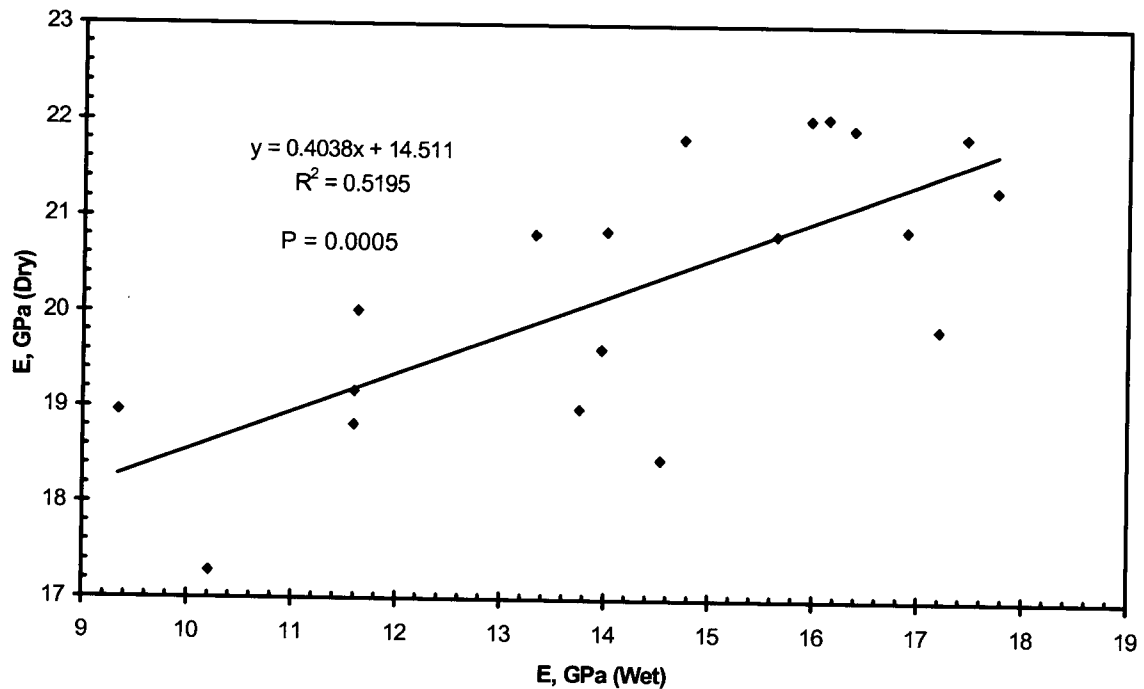


Figure 3.6 Wet-dry elastic modulus correlation.

The  $R^2$  value for the correlation between dry and wet measurements was 0.52, providing a correlation coefficient of 0.72. The P-value for this linear regression was 0.0005, which was highly statistical significant.

### 3.2 Modulus of Elasticity Distribution across Medial Cortical Wall

A typical modulus distribution across the cortical wall thickness is shown in Figure 3.7. The elastic modulus varied from 13 GPa to 23 GPa. In general, it appeared that interstitial bone

had higher values of modulus than osteonal bone. In addition to that, the elastic modulus at the periosteal and the endosteal zones were lower than the central part of the cortical bone.

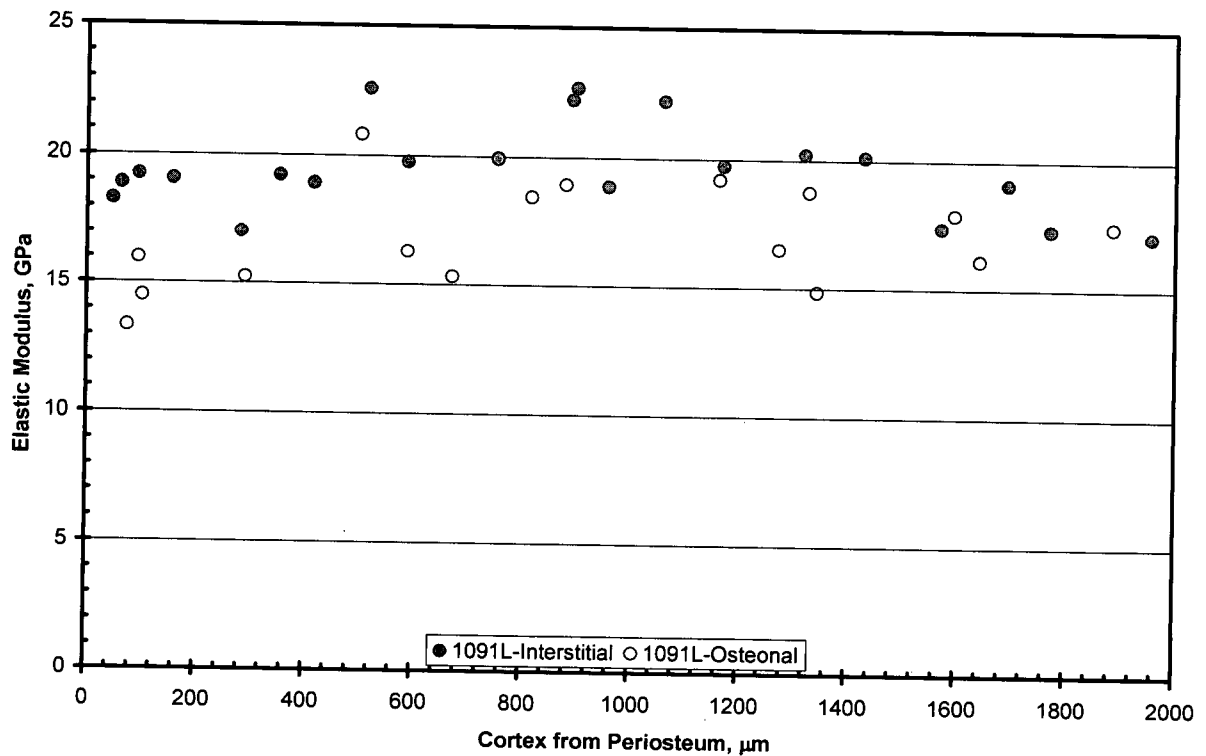


Figure 3.7 Typical modulus distribution across medial cortical wall.

Different specimens had different geometry, with cortical wall thickness varying from 1800  $\mu\text{m}$  to 4200  $\mu\text{m}$ . Figure 3.8 shows the normalized elastic modulus distribution across the cortical wall for all the 13 specimens (total of 26 distribution curves – osteonal and interstitial). Two samples (1069L and 1069R) were not included as they were abnormal bones; however they were extremely important specimens in this research work.

The elastic modulus varied from approximately 12 GPa to 26 GPa, and a decrease of the modulus of elasticity was once again observed in the periosteal and endosteal zones. However, this aspect has to be confirmed statistically.

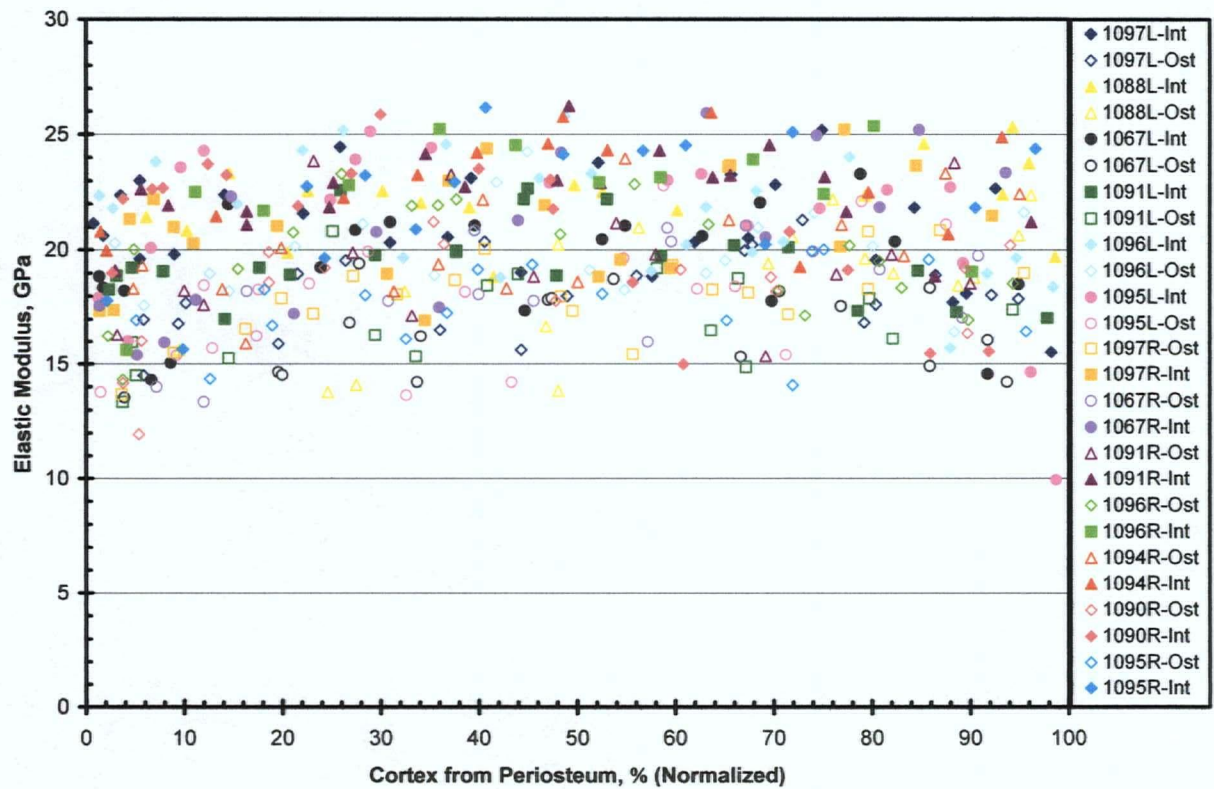


Figure 3.8 Normalized modulus distribution across medial cortical wall.

From Figure 3.9, the difference between osteonal and interstitial bone became more evident. On average in all the subregions, (with the exception of the endosteal zone) the osteonal bone presented 15.2% inferior modulus values when comparing to interstitial bone. In the endosteal zone, the same trend was seen, even though the decrease in modulus was only 7.3%. The two-way repeated measures ANOVA analysis of all the data in Figure 3.8 found the modulus difference between osteonal and interstitial bone to be highly significant ( $P < 0.0001$ ).

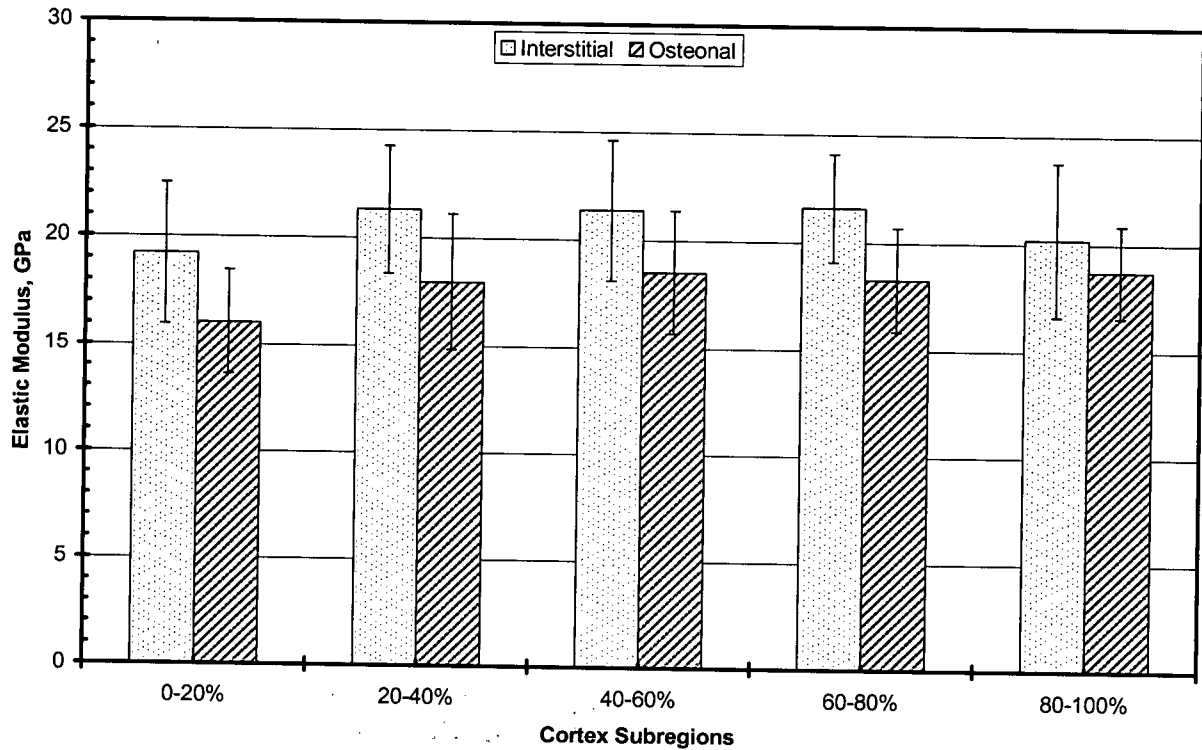


Figure 3.9 Mean ( $\pm$ SD) elastic modulus distribution for five cortical wall subregions (periosteum – 0 – 20%).

The central zone (20 – 80%) in cortical wall exhibited a uniform modulus distribution for both osteonal and interstitial bone. The average modulus value for interstitial bone in this region was 21.4 GPa, while that of osteonal bone was 18.3 GPa. The periosteal zone revealed a significant decrease of 11% (to 19.2 GPa and 16.2 GPa for osteonal and interstitial bone respectively) compared to the central zone. The endosteal zone presented a different trend, where there was no change in osteonal bone, but a slight reduction (5.7%) in interstitial bone (to 20.2 GPa). The modulus differences among the cortex subregions were also analyzed by ANOVA analysis. In general, this difference was also highly significant ( $P < 0.0001$ ), meaning that the elastic modulus did change within the cortex subregions.

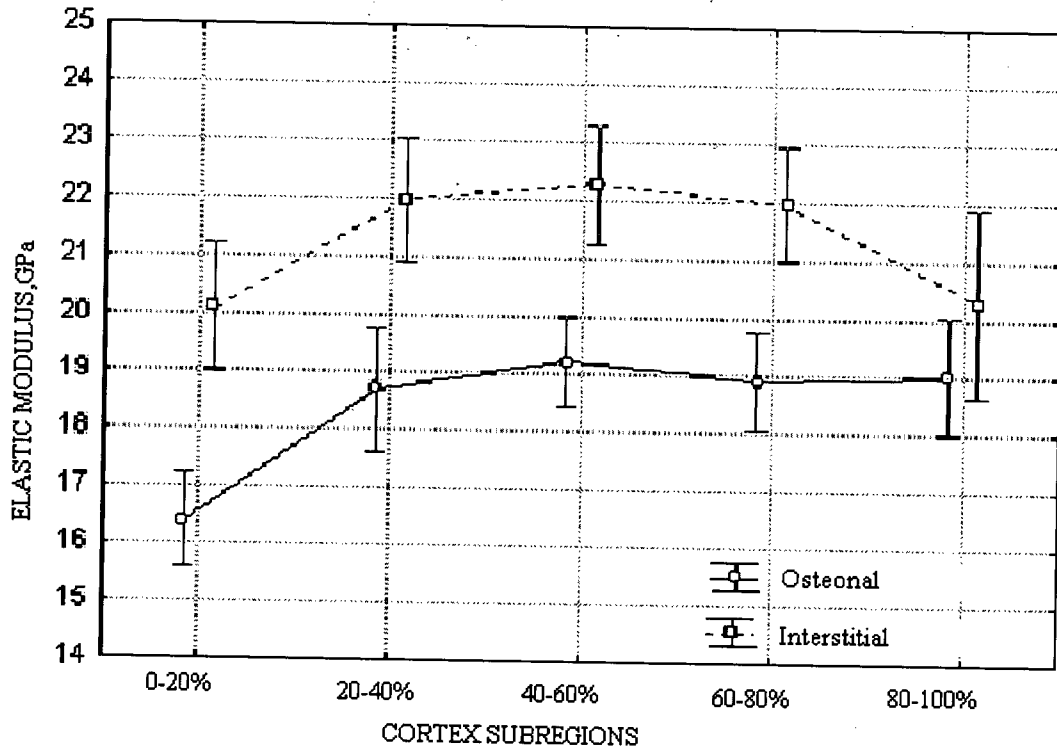


Figure 3.10 Modulus two-way repeated measures ANOVA.

When considering the interaction between the two factors (microstructure and position), the P-value demonstrated a significant effect ( $P = 0.034$ ) (Figure 3.10). The Newman-Keuls post-hoc analysis (Appendix C – Table C1) calculated all the pairwise combinations of the P-value for the two factors (the microstructural factor between osteonal and interstitial bone, and the position factor among the cortex subregions). The table correlates the ten variables (O-Osteonal and I-Interstitial for the five subregions 1-5) and the significant statistical results are highlighted. This analysis confirmed that the 60% central zone revealed no statistical significant variation ( $0.59 < P < 0.85$ ). The periosteal zone displayed a drop in both osteonal bone ( $P = 0.0002$ ) and interstitial bone ( $P = 0.007$ ) when compared to the 20 – 40% subregion. The endosteal zone had a decline in interstitial bone only, with a P-value of 0.004

(I4-I5), while for osteonal bone the P-value was 0.84 (O4-O5). This finding also confirmed the significance of the interaction between the two factors.

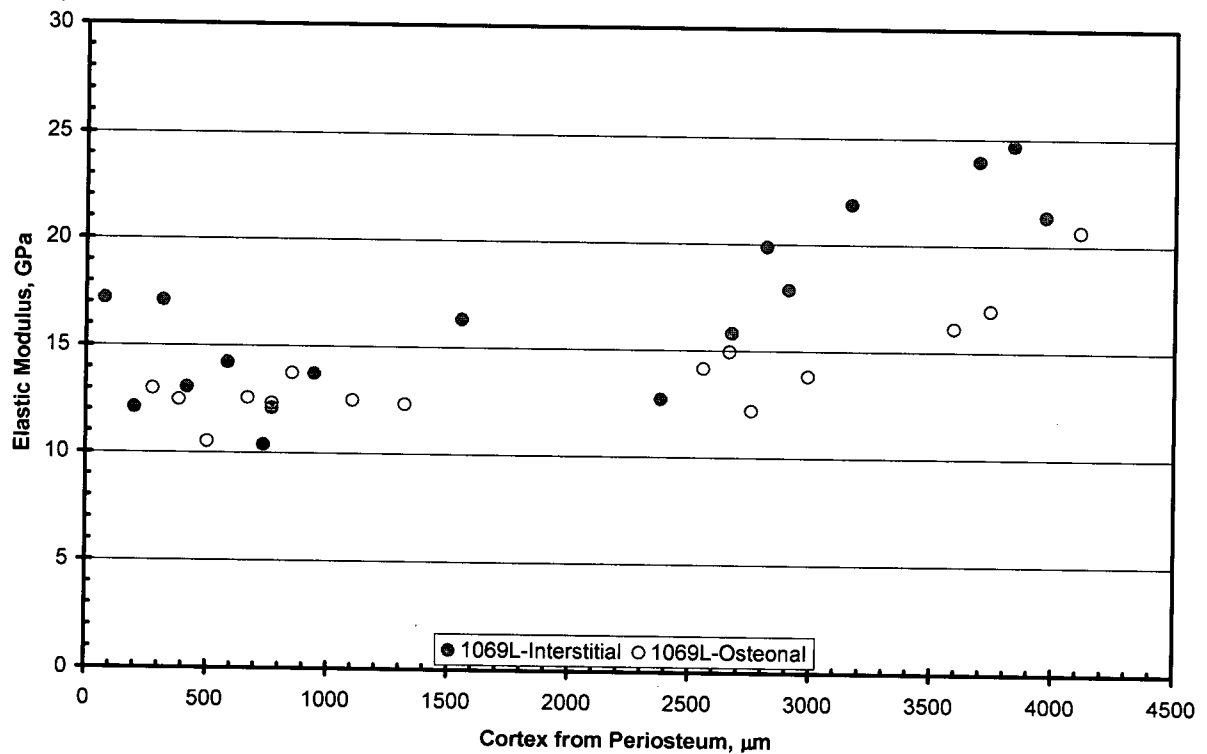


Figure 3.11 Abnormal modulus distribution across medial cortical wall.

As previously mentioned, the pair of tibiae from specimen 1069 was analyzed separately as it presented an abnormal behaviour. The distribution curves for these two specimens (1069L and 1069R) were very alike. Figure 3.11 shows the results of 1069L. These two specimens revealed totally different behaviour when compared to the other samples. The elastic modulus was low from periosteum to approximately 3000 μm inside the cortex, which equalled about two thirds of the cortical wall thickness. Interstitial bone still presented higher modulus than osteonal bone; however, a smaller difference was observed.

### 3.3 Bone Mineral Content Distribution across Medial Cortical Wall

From the grey-level reading obtained from Figure 3.12, the distribution curve of a typical sample 1097L was drawn (Figure 3.13). Interstitial bone appeared to have a higher bone mineral content than osteonal bone.

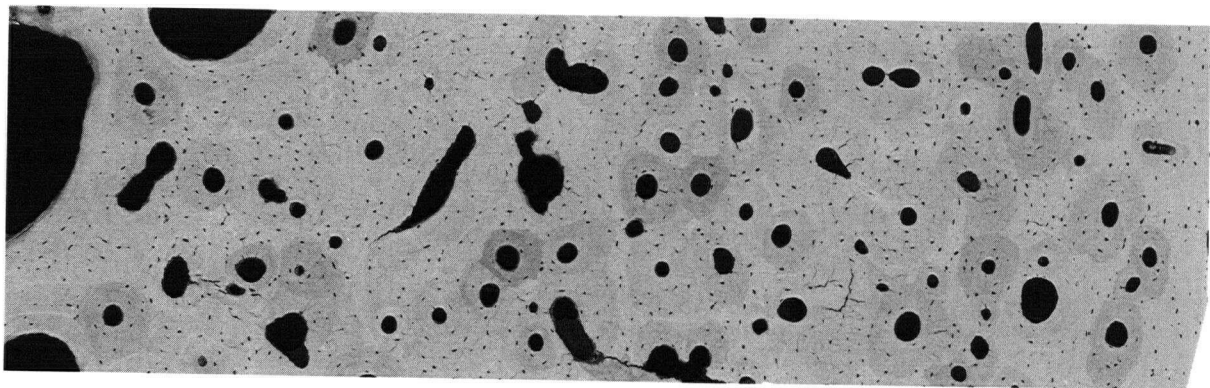


Figure 3.12 *qBSEi* of sample 1097L used to map bone mineral content distribution. Horizontal length – 3350  $\mu\text{m}$ .

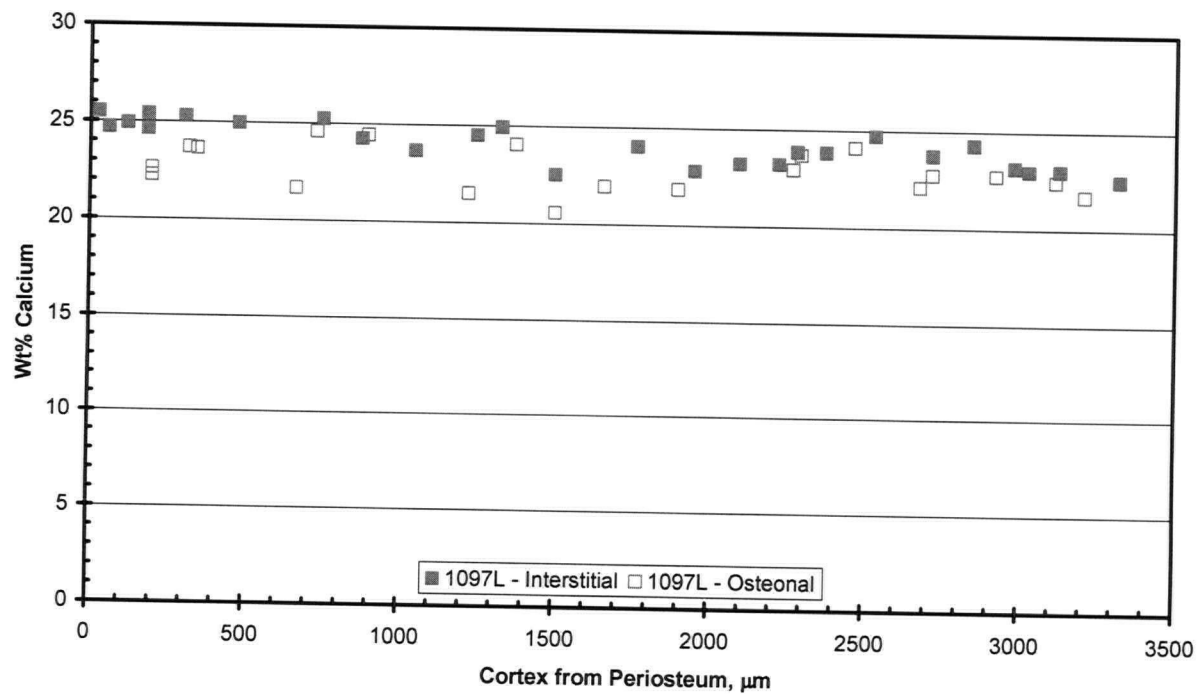


Figure 3.13 Typical calcium content distribution across medial cortical wall.

Figure 3.14 shows the calcium content distribution for four out of the five specimens aforementioned (total of 8 distribution curves – osteonal and interstitial). Once again, sample 1069L was not included as it reveals a different behaviour (Figure 3.15) with lower bone mineral content. Once again, a normalized cortical thickness was used for comparative analysis between all the medial cortical tibiae, as they had different geometry and cortical wall thickness.

Other than a few outliers, the scatter of the data was remarkably small (approximately 5 percentage points), varying from 20.5 to 25.7%. A consistent distribution was found for all samples throughout the entire cortical wall thickness with a small drop in the endosteal zone.

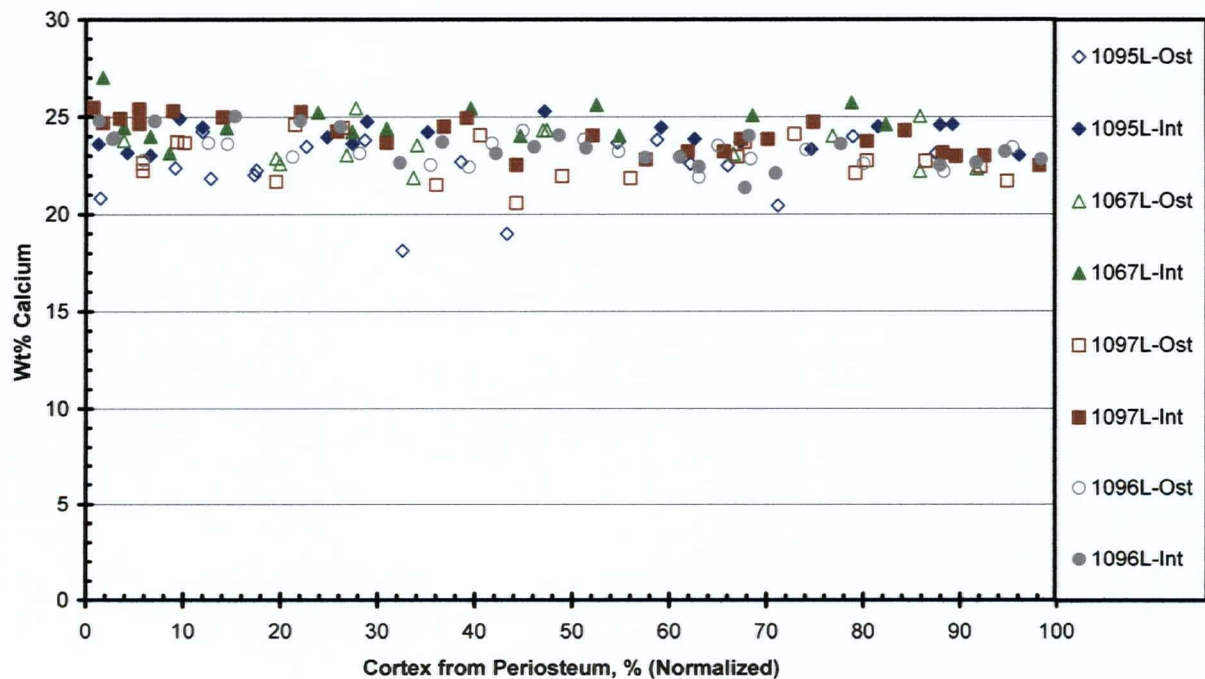


Figure 3.14 Normalized calcium content distribution across medial cortical wall.

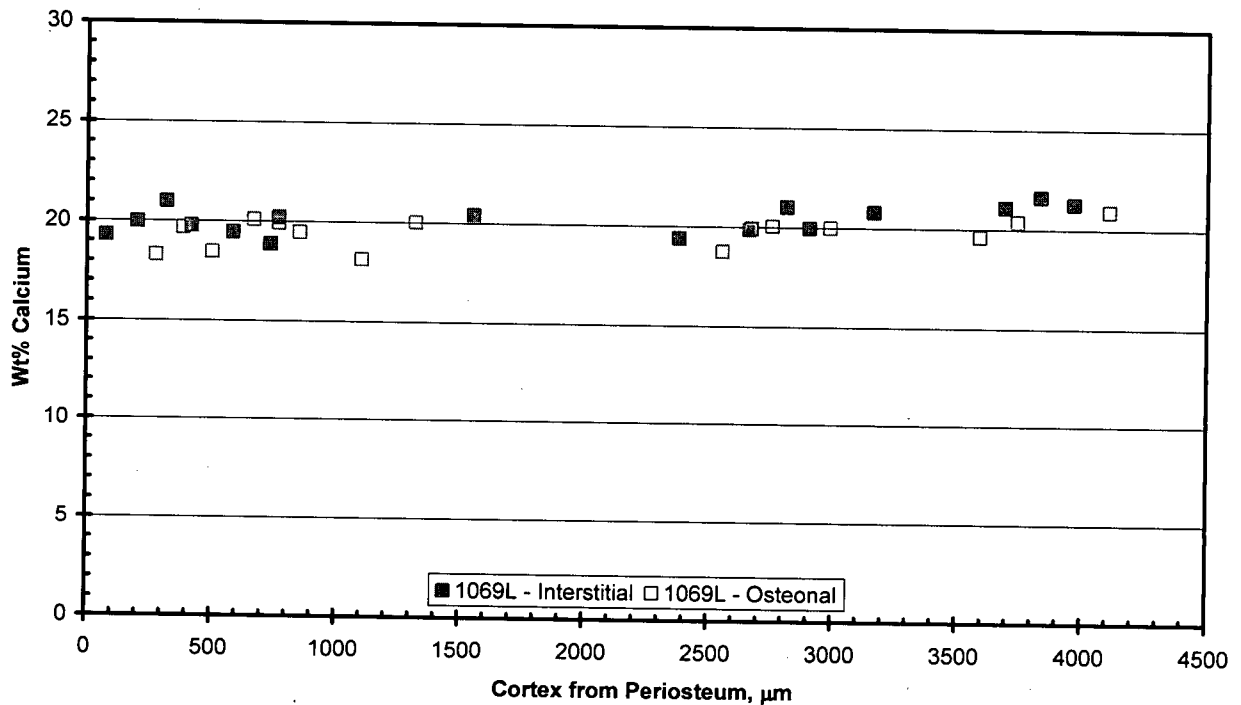


Figure 3.15 Abnormal calcium content distribution across medial cortical wall.

Figure 3.16 presents the mean value and standard deviation of calcium content for the five cortex subregions. Osteonal bone appeared to have an inferior value of bone mineral content than interstitial bone, as well as being more uniformly distributed across the cortical wall, varying from 22.78% Ca to 22.97% Ca, a difference of only 0.8% that can be considered as negligible. Interstitial bone, on the other hand, had a different trend, varying all the way through the cortex, from a higher bone mineral content in the periosteum (24.57% Ca) to a lower bone mineral content in the endosteum (23.48% Ca), resulting in an variation of 4.6%, also a very small discrepancy. The difference between osteonal and interstitial bone was higher in the periosteal zone, where it corresponded to 7.2%.

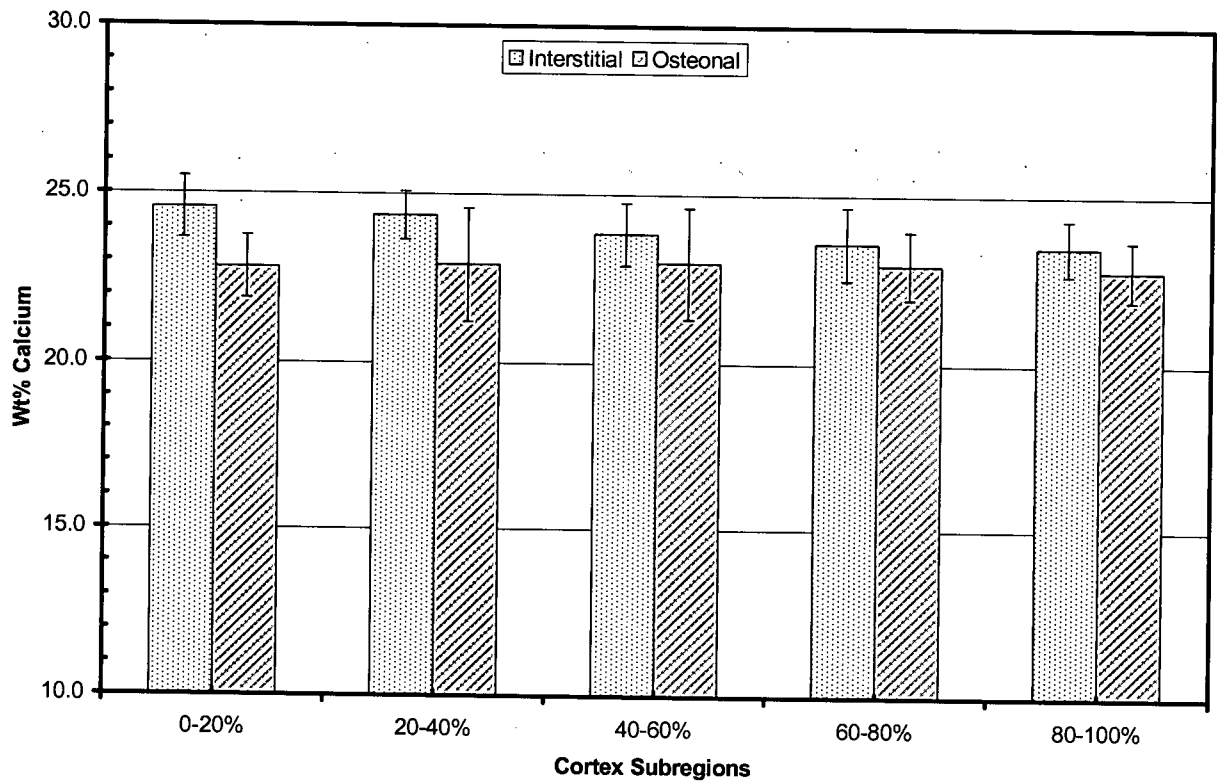


Figure 3.16 Mean ( $\pm$ SD) calcium content modulus distribution for five cortical wall subregions (periosteum – 0 – 20%).

The two-way repeated measures ANOVA confirmed that the calcium content difference between osteonal and interstitial bone was also statistically significant ( $P = 0.029$ ). When considering the five cortex subregions, a  $P$ -value of 0.78 was found, which means that no significant difference was observed in this factor. Furthermore, the interaction between the two variables (microstructure and position), had no significant difference either ( $P = 0.35$ ) as seen in Figure 3.17.

The Newman-Keuls post-hoc analysis for calcium content distribution is presented in Appendix C – Table C2.

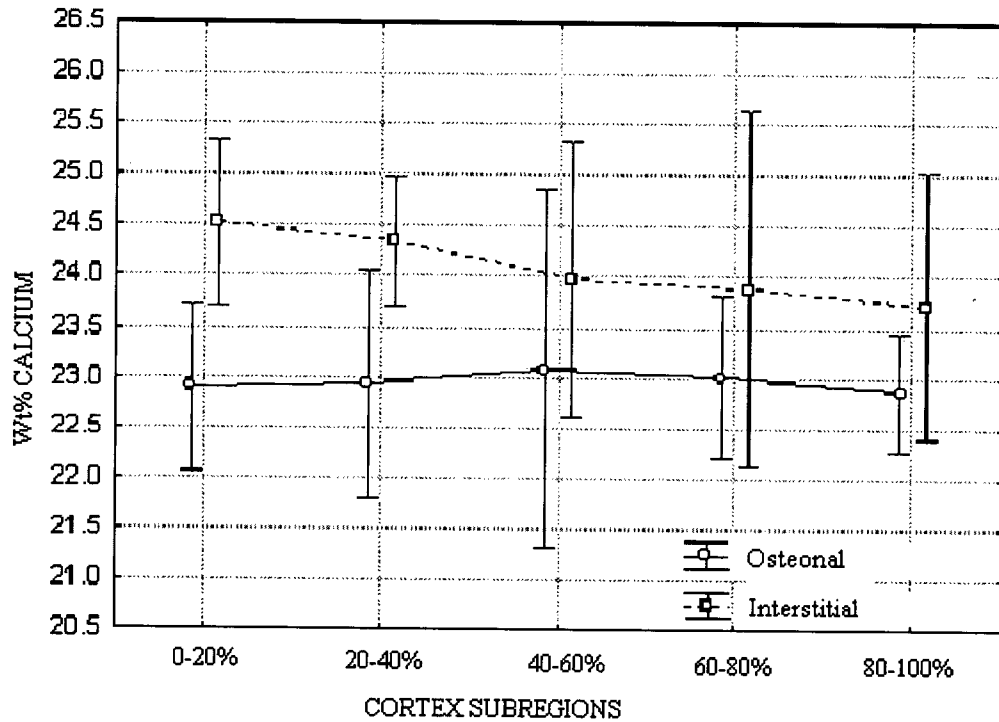


Figure 3.17 Bone Mineral content two-way repeated measures ANOVA.

### 3.3.1 Modulus versus Bone Mineral Content Correlation

Figure 3.18 shows a scatterplot between nanoindentation modulus and bone mineral content of data from the five samples (1067L, 1069L, 1095L, 1096L and 1097L). The general trend, as expected, was that elastic modulus increased with increasing bone mineral content. Once more, specimen 1069L presented the lowest calcium content (19.7 Wt% Ca) and specimen 1095L showed the largest range of calcium content (from 16.6 to 25.3 Wt% Ca). The three other samples were more consistent to each other and had a higher calcium content (average of 23.3 Wt% Ca).

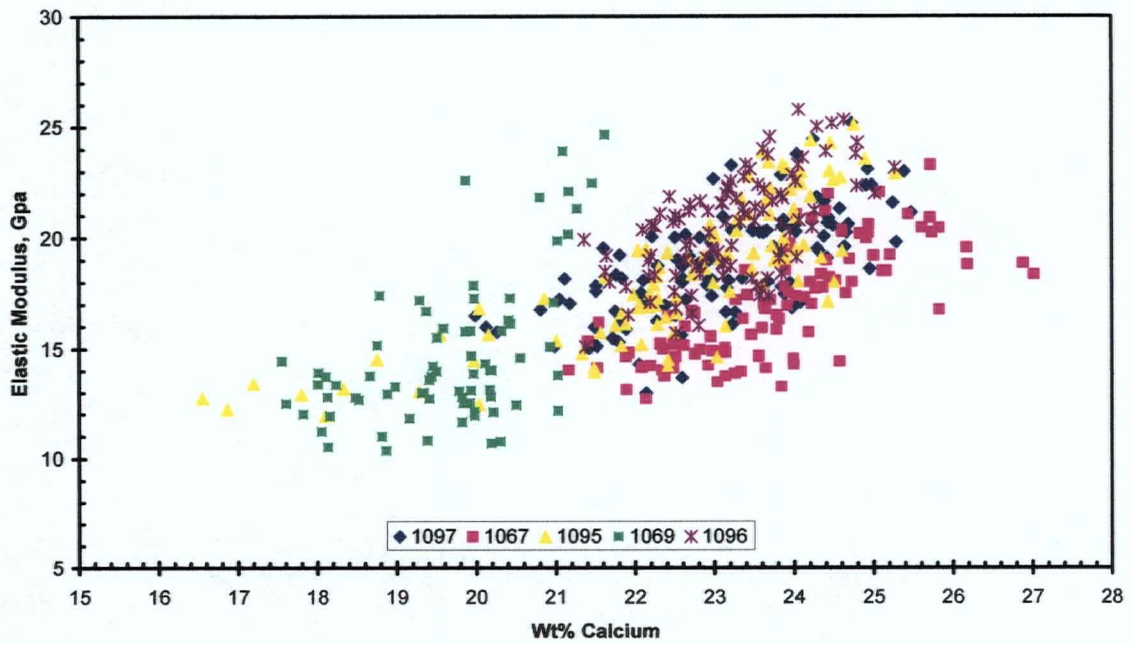


Figure 3.18 Scatterplot of modulus versus bone mineral content.

Figure 3.19 shows a linear regression that was fit to these data. Even though there was a relationship between these two parameters ( $R^2 = 0.45$ ), such correlation was not completely linear. The correlation coefficient was 0.67 with a P-value that was less than 0.0001.

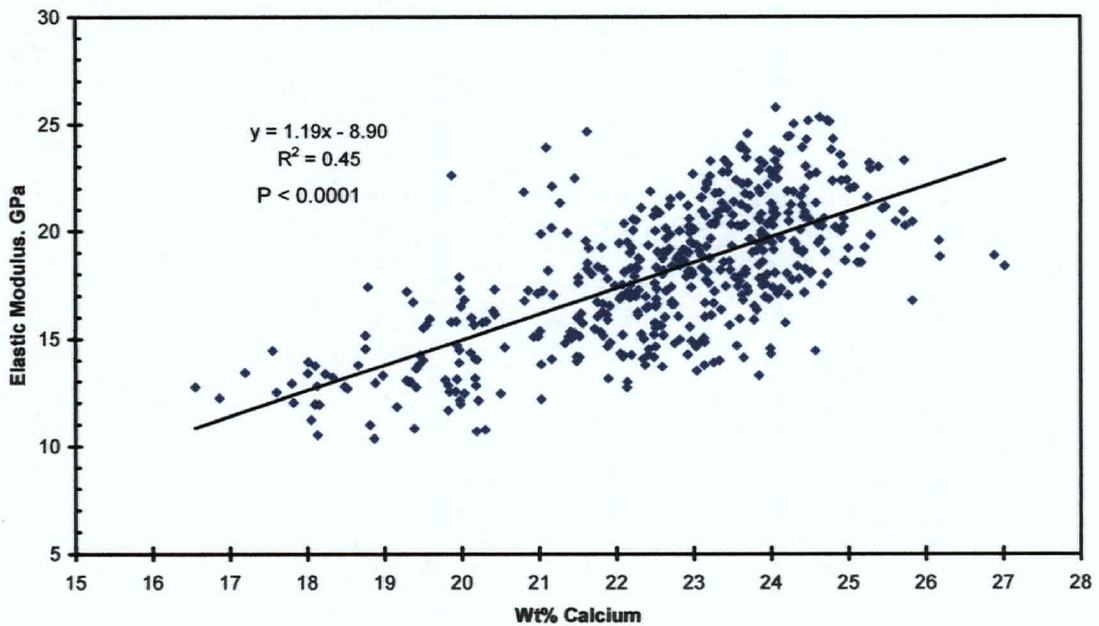


Figure 3.19 Linear regression for the modulus versus bone mineral content correlation.

### 3.4 pQCT Imaging – qBSEi Correlation

This section will be divided in three sub-sections, the first one regarding the mean bone mineral content across the cortical wall and the second one related to the porosity across cortical wall. The analysis for both was made using a five zone division for the cortex with subsequent correlation to pQCT, seen in the third sub-section.

#### 3.4.1 Mean Bone Mineral Content across Cortical Wall

The mean bone mineral content across the medial cortical wall was measured using calibrated qBSE images. Figure 3.20 presents the calcium content for the five tibia samples analyzed by qBSEi. The data were divided in five equal subregions from periosteum to endosteum.

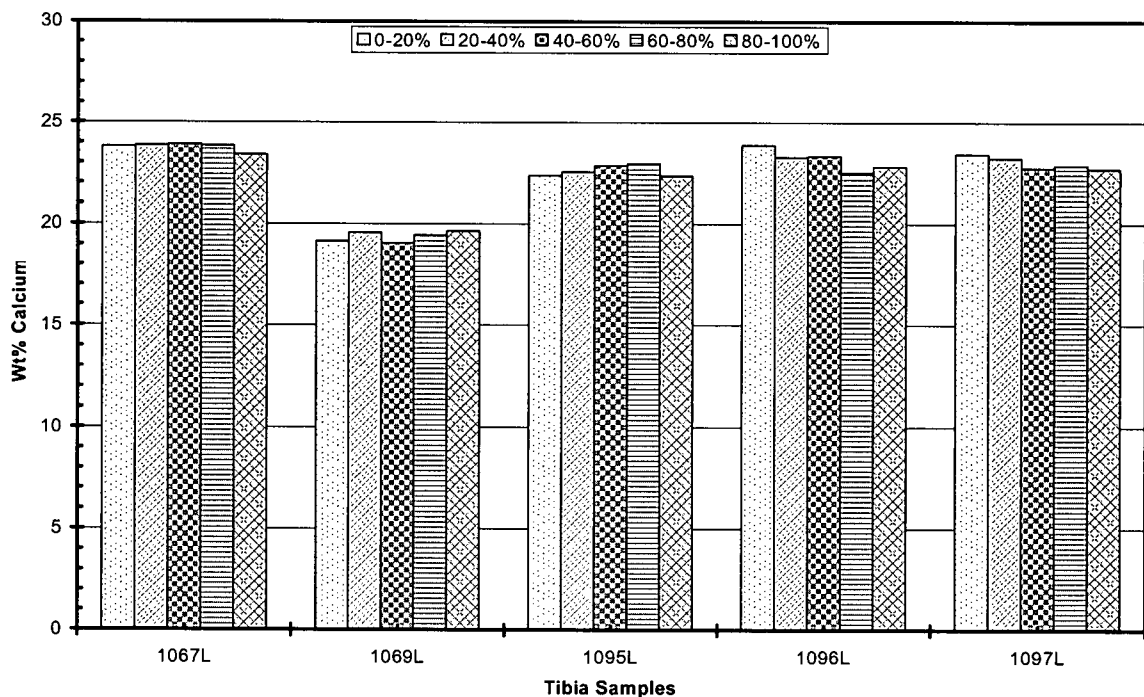


Figure 3.20 Mean bone mineral content for five zones division cortex.

The largest intrapersonal variation was observed for sample 1096L between the periosteal zone and fourth zone (5.83%). Besides that, all the samples had a percentage difference lower than 3.2% and the smallest variation was found for the sample 1067L (2.15%).

Apart from sample 1069L, the interpersonal variation was not evident, with the greatest discrepancy between samples 1067L, which had 23.74% in calcium content, and 1095L, which had 22.61% (a difference of 4.74%). Sample 1069L had 18.49% less calcium than sample 1067L.

### 3.4.2 Porosity across Cortical Wall

The porosity across the medial cortical wall was also calculated using calibrated qBSEi. Figures 3.21, 3.22 and 3.23 show the qBSEi for samples 1095L, 1096L and 1069L respectively. The periosteal zone is located in the right side of the page. Sample 1069L had the highest degree of porosity. Figure 3.24 presents the porosity for the five tibia samples analyzed by qBSEi. The data were divided in five equal subregions from periosteum to endosteum.

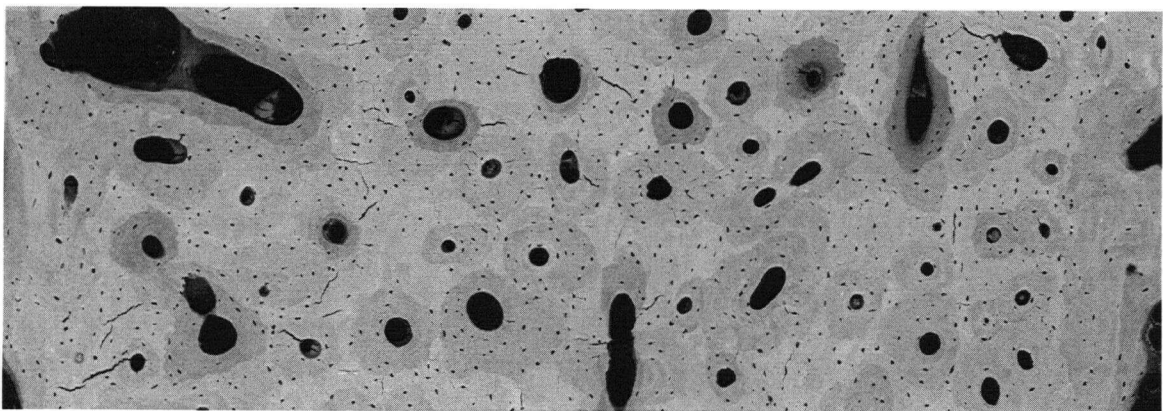


*Figure 3.21 qBSEi for sample 1095L. Horizontal length – 3100  $\mu$ m.*

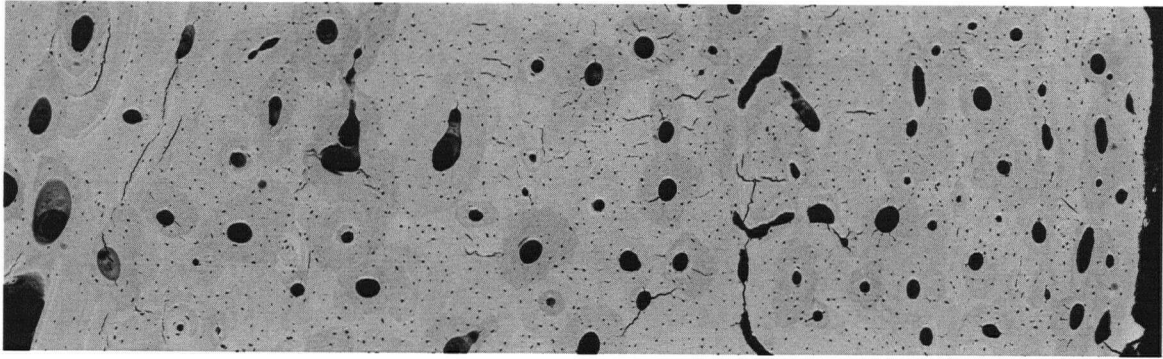


*Figure 3.22 qBSEi for sample 1096L. Horizontal length – 4300  $\mu\text{m}$ .*

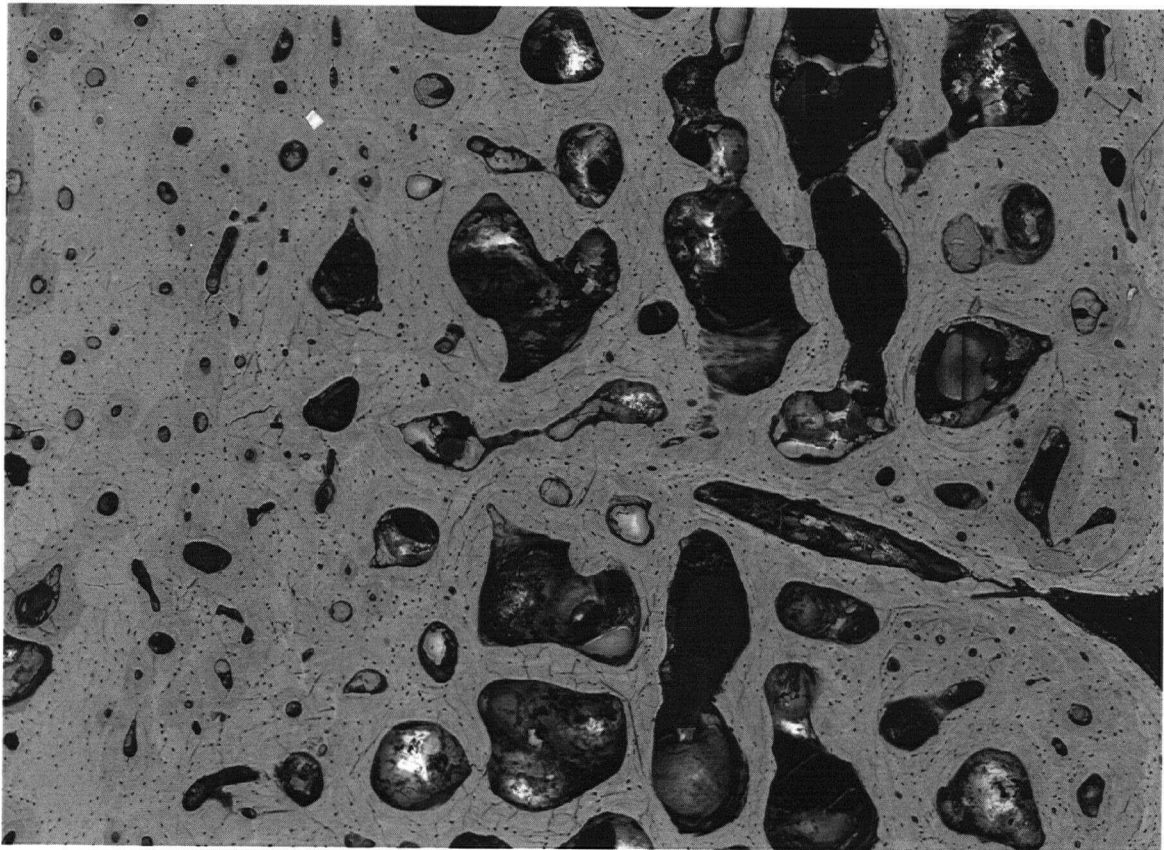


*Figure 3.23 qBSEi for sample 1069L. Horizontal length – 4100  $\mu\text{m}$ .*

The degree of porosity varied from sample to sample and also within the same sample had different distribution trends. However, sample 1069L presented much higher porosity (29.72% on average, with a peak of 47.20% in the zone adjacent to the periosteum). The other samples had an average degree of porosity of approximately 10% or less. Sample 1096L contained only 6% porosity (average) and its endosteal zone was the lowest of all the samples with merely 5%. No trend was observed among all the samples; however, the degree of porosity was expected to greatly affect the bone density reading provided by pQCT.

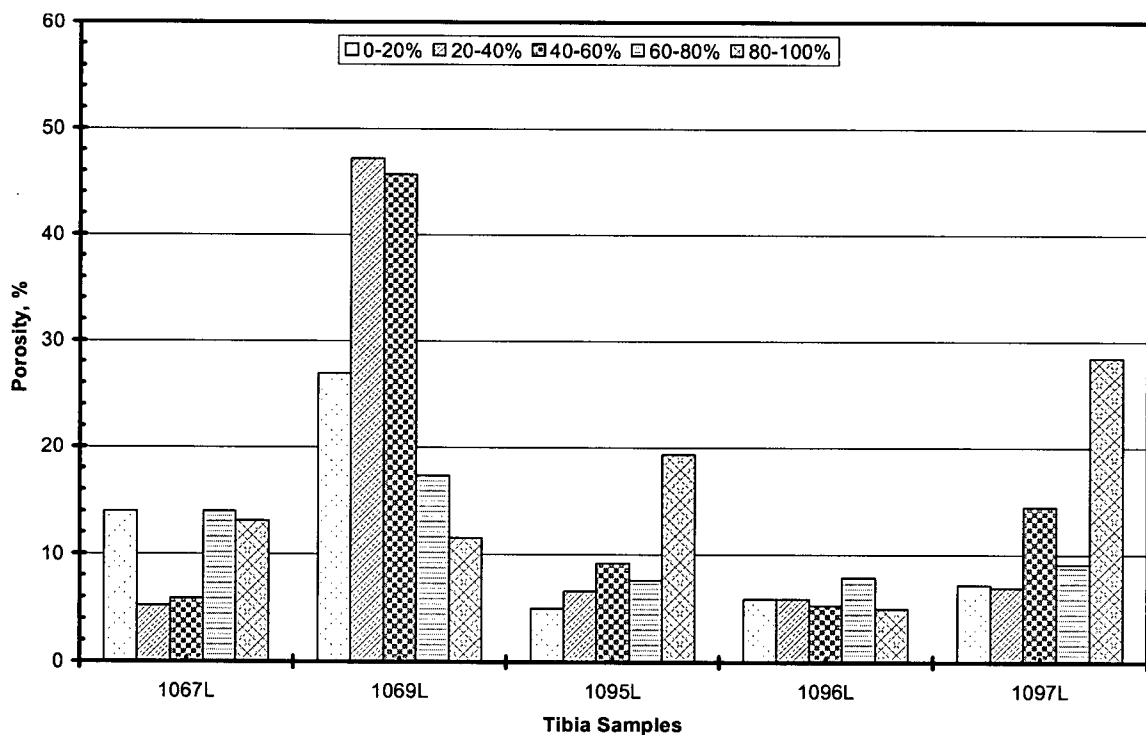


Figure 3.24 Porosity variation for five zones division cortex.

### 3.4.3 pQCT Reading and Correlation

The bone density reading provided by pQCT was measured on the same five samples used above. From the pQCT reading (as seen in Figure 2.12), a five zone division (Figure 3.25) was applied to allow a correlation with the individual parameters that characterize the

apparent density measured by pQCT. These parameters are bone mineral content and porosity as described in the two previous sub-sections.

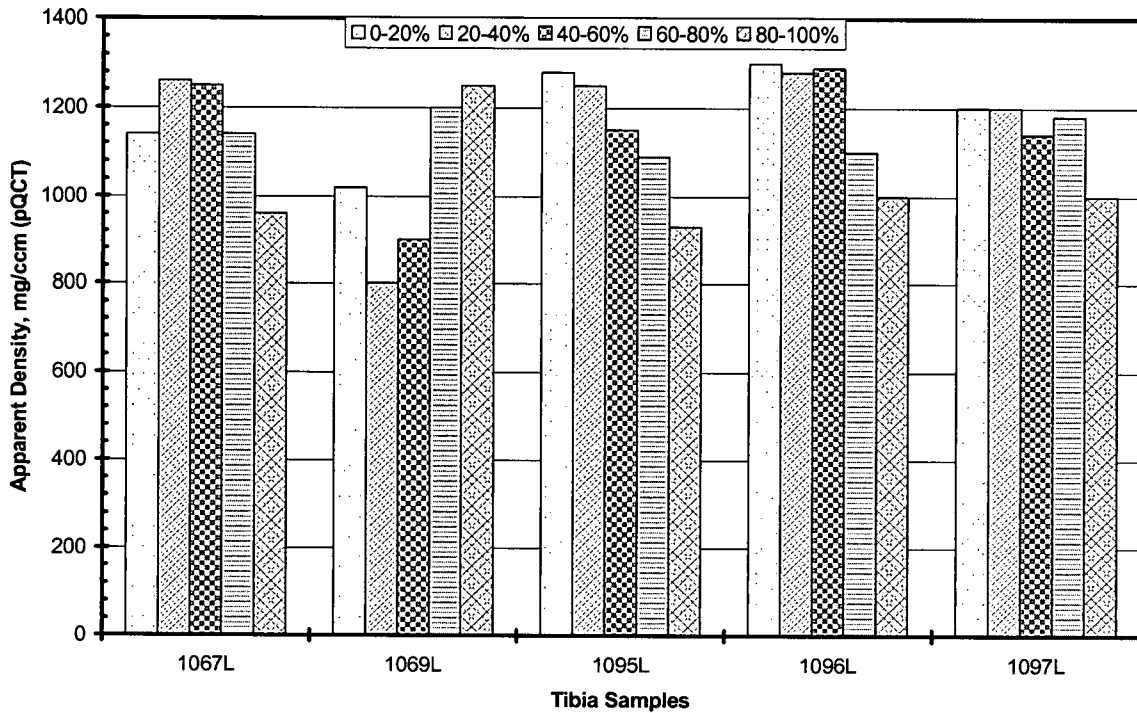


Figure 3.25 Apparent density by pQCT for five zones division cortex.

As observed in section 3.4.2, the pQCT reading also did not reveal any characteristic trend for the five samples. However, pQCT readings had an inverse relation with the porosity (Figure 3.26), meaning that porosity had a major influence in the bone apparent density provided by pQCT. The zones with higher degree of porosity revealed a lower apparent density.

The influence of each factor was investigated by plotting a linear regression from the apparent density data versus each density factor (bone mineral content and porosity). Figure 3.26 provides the information concerning the effect of porosity and Figure 3.27 is related to the bone mineral content.

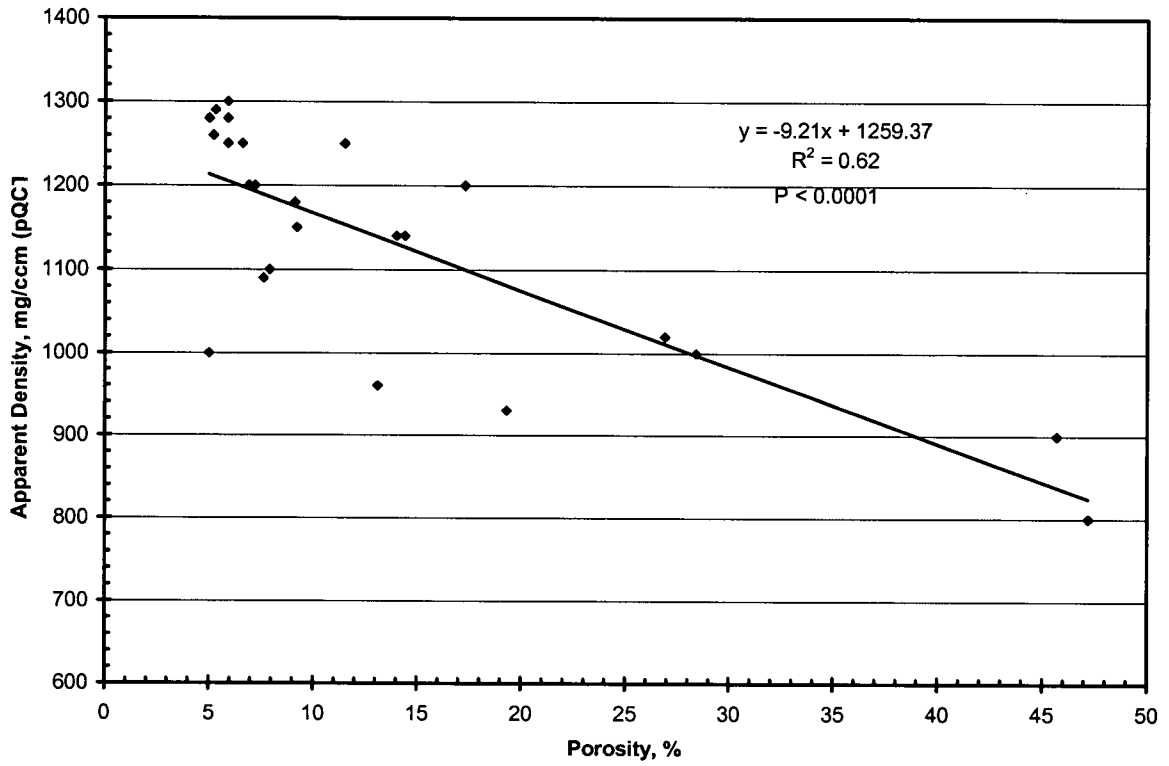


Figure 3.26 Effect of porosity in the apparent density measured by pQCT.

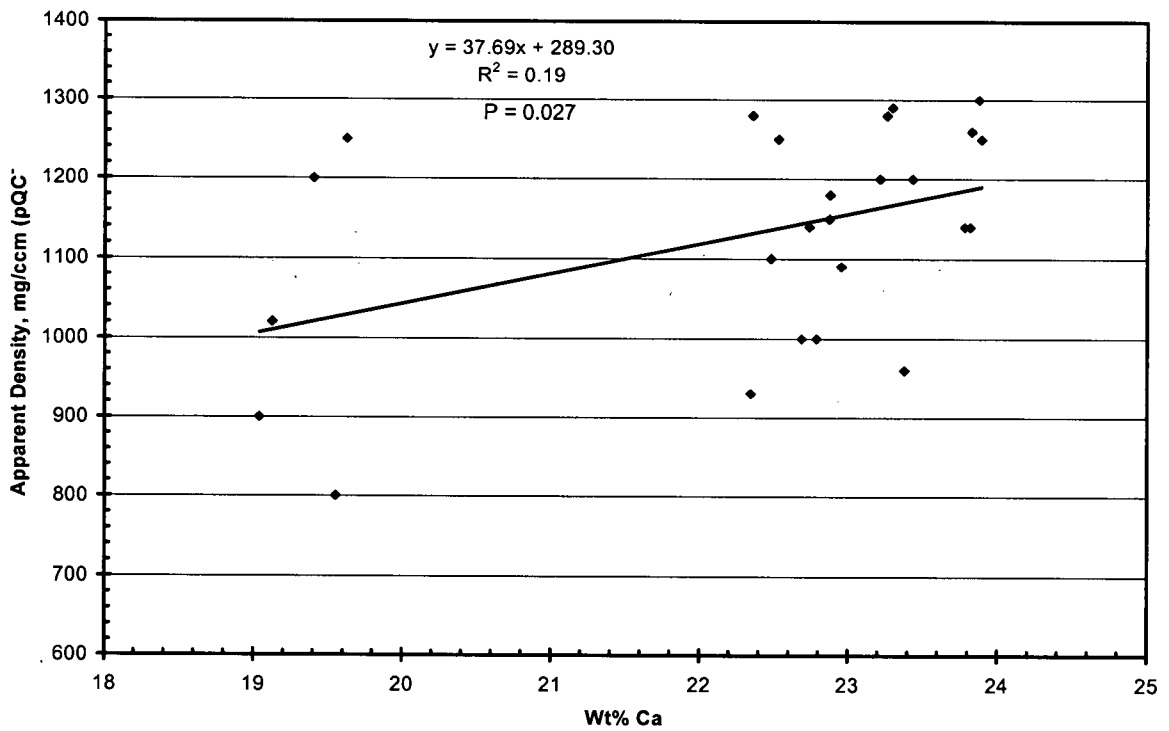


Figure 3.27 Effect of bone mineral content in the apparent density measured by pQCT.

The  $R^2$  provided by linear regression for the effect of porosity ( $R^2 = 0.62$ ) was considerably higher than the one obtained from the effect of bone mineral content ( $R^2 = 0.19$ ). The correlation coefficient for porosity ( $R = -0.79$  and  $P < 0.0001$ ) was almost twice as large as the one for bone mineral content ( $R = 0.44$  and  $P = 0.027$ ), indicating that the porosity outweighed the overall bone apparent density measured with pQCT and can be considered as a good indicator of bone quality.

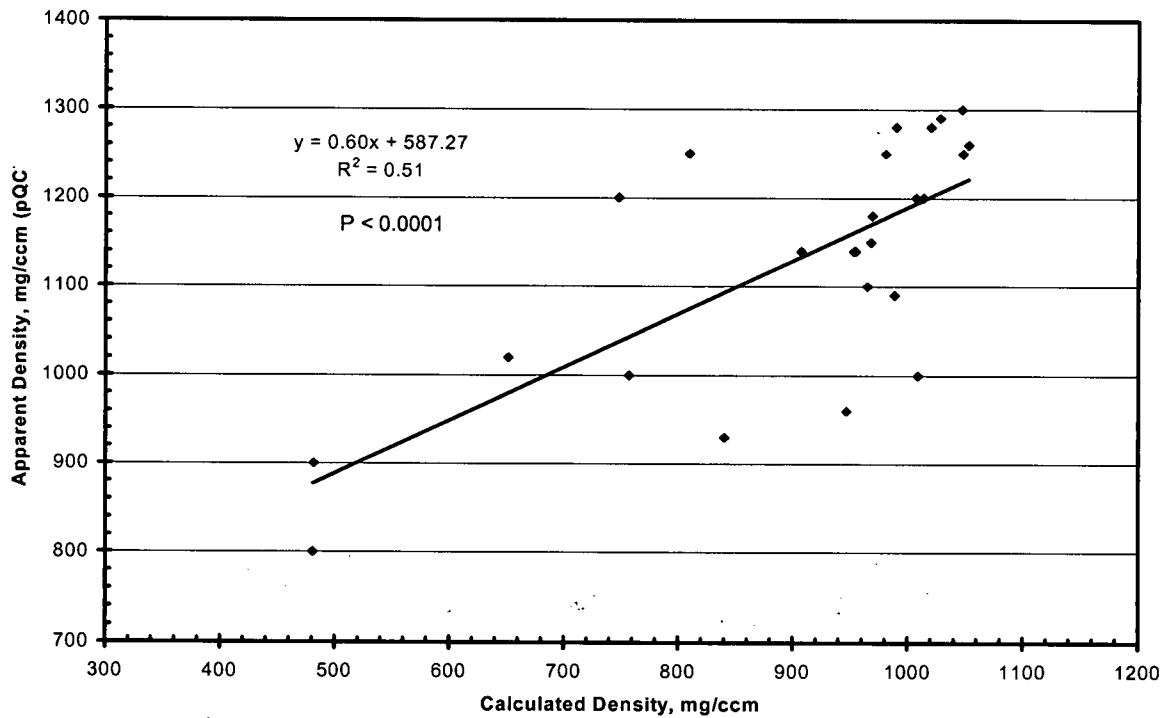


Figure 3.28 Calculated density compared to the apparent density measured by pQCT.

The calculated material density from bone mineral content and porosity was also compared to the apparent density provided by pQCT (Figure 3.28). The  $R^2$  provided by linear regression for the calculated material density was 0.51, resulting in a correlation coefficient of 0.72 with a P-value less than 0.0001. The calculated apparent density of cortical bone is a mixture of bone material and porosity. Consequently, the  $R^2$  dropped, due to the low correlation between pQCT and bone mineral content.

## **Chapter 4 Discussions**

This chapter will be divided in the following sections: Basic Material Properties of Bone; Modulus and Bone Mineral Content Distribution and the pQCT Imaging – qBSEi Correlation.

Ideally, a larger age range for the bone specimens would be desired; however, young cadaveric bone is difficult to acquire. The human bone specimens used in this research were fairly old (between 67 and 88 years) and two of them presented a significant bone mass loss (specimens 1069L and 1069R).

### **4.1 Basic Material Properties of Bone**

Depth-dependence measurements acquired with the Continuous Stiffness Measurement (CSM) proved to be a valid way for detecting faulty measurements that might occur due the heterogeneity of bone microstructure. This was due to the sinusoidal signal that is superimposed on top of the primary loading signal, resulting in several unloading data during a single measurement. On the other hand, traditional nanoindentation is based on only one unloading test. CSM also provided faster measurements for viscoelastic properties as it was not necessary to perform loading cycles.

The experimental conditions proved to be very important in the nanomechanical testing, as it dramatically affected the material properties of the bone tissue being measured. Particularly, water content of bone, had a major effect on the material properties of bone tissue. Rho et al.

reported a value of 22.5 GPa for the elastic modulus of dried human tibia bone. In our work, it was reported a value of 20.3 GPa for dried human tibia bone. However, Rho et al. used ethanol dehydrated samples, which in turn decreased even further the water content of bone.

When comparing dry measurements to wet measurements, a decrease of 29.7% was found for elastic modulus after rehydration. This value seems much larger than what the literature presented. The wet conditions in this work were fully wet, meaning that bone was completely submerged in water during experimental testing. From Figure 3.5, a decrease of 8.8% was found between the first day (19.4 GPa) and the plateau region of the curve (21.1 GPa). The first day was approximately eight hours from a soaked bone state.

The correlation between dry and wet modulus provided a fairly significant correlation coefficient ( $R = 0.72$ ). A higher correlation coefficient was expected, as the mineral phase was thought to contribute the most to the material properties of bone. The two main constituents of bone in dry state are the collagen fibres and the carbonated apatite minerals. Possibly, after rehydration, the collagen fibres became more malleable, and as a result, bone became less stiff as a structure. Consequently, from a brittle material in dry state, bone became a more ductile, viscoelastic material in re-wet state.

A drawback of wet measurements was that it is extremely time-consuming and complex to keep bone moist without affecting the stability of the nanoindenter. In addition to that, the safety of the nanoindenter drove the research to be conducted in a controlled dry state.

## 4.2 Modulus and Bone Mineral Content Distribution

qBSEi technique was chosen over contact microradiography in this work. The setting of the electron beam energy to 20 kV created a backscattered electron that is scattered back from the top 3  $\mu\text{m}$  of the bone surface. Consequently, this data was in the same range as the penetration depth in nanoindentation testing. Contact microradiography also provided the bone mineral content; however required a bone cross section of approximately 100  $\mu\text{m}$ . The main advantage of contact microradiography was that it required only one radiographic image to map the entire cross-section of human tibial bone. Using qBSEi, even at a low magnification, it is required to take few images to cover one entire anatomical site.

The stability of the current in the SEM instrument was a great concern as it can drastically alter the beam energy. However, the current was monitored which allowed us to quantify the bone mineral content to correlate to nanoindentation modulus, and also the degree of porosity for pQCT correlation.

Comparing the distribution curves for elastic modulus and bone mineral content, it is observed that they do not present the same trend. At first, this was thought to be due the different number of samples that could perhaps be affecting the statistical analysis (elastic modulus:  $n = 13$ ; bone mineral content:  $n = 4$ ). Thus, the data for elastic modulus distribution across the cortex was re-analyzed for the same four samples as in the bone mineral content distribution (Figure 4.1). The P-values of the statistical analysis were less significant than before, but the same trend was remarked and the P-values still highly significant. The microstructure factor had a highly significant P-value of 0.005. The position factor had a

significant P-value of 0.001. The interaction between both factors also resulted in a highly significant P-value of 0.005.

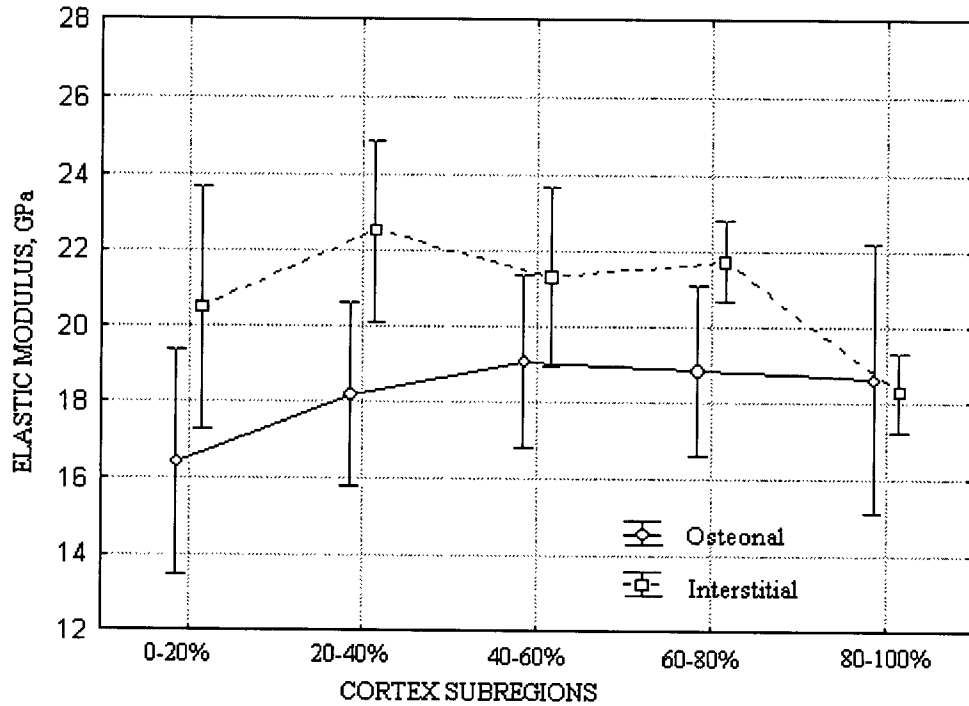


Figure 4.1 Modulus two-way repeated measures ANOVA.

The linear regression between nanoindentation modulus and bone mineral content measured by qBSEi showed a fairly significant correlation coefficient ( $R = 0.67$  and  $P < 0.0001$ ). However, these results are more accurate than the previous research done in the literature. Based on their set of data, the correlation coefficient found by Roschger et al. [37] was approximately  $R = 0.48$ .

A log-log plot with logarithmic regression (Figure 4.2) was also fit to the scatterplot and provided a slightly higher correlation coefficient ( $R = 0.69$  and  $P < 0.0001$ ). The correlation was not completely linear; however there was a clear trend, especially when analysing the

cortical bone microstructure, where the higher mineralized interstitial bone also had higher modulus of elasticity.

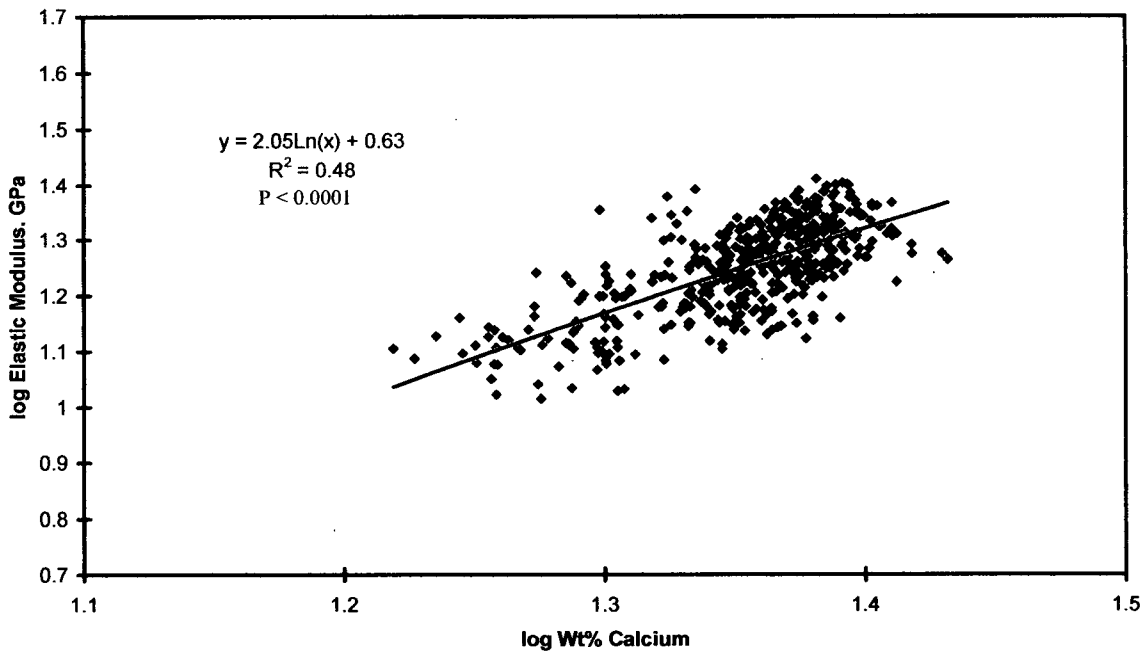


Figure 4.2 Log-log correlation between modulus and bone mineral content.

### 4.3 pQCT Imaging – qBSEi Correlation

pQCT is an excellent instrument to assess bone mineral density and to provide clinical evaluation of bone health quality. As it measures an apparent density of bone, due to the porous structure of bone, it becomes necessary to understand what pQCT is measuring in reality.

With a correlation coefficient of -0.79, porosity appeared to be an important indicator of bone health macroscopically. The pQCT data of sample 1069L (Figure 4.3) was a clear example of this observation. From Figure 3.23, which shows the qBSEi of sample 1069L,

and Figure 4.3, which shows the pQCT data of the same sample, the decrease in apparent density caused by the highly porous structure was observed. Overall, all the bones presented high average apparent density (higher than 1140 mg/ccm). Sample 1069L, as expected due to its excessively porous microstructure had the lowest density (1034 mg/ccm). The sample 1096L, which contained only 6% of porosity, exhibited the highest average apparent density (1194 mg/ccm).

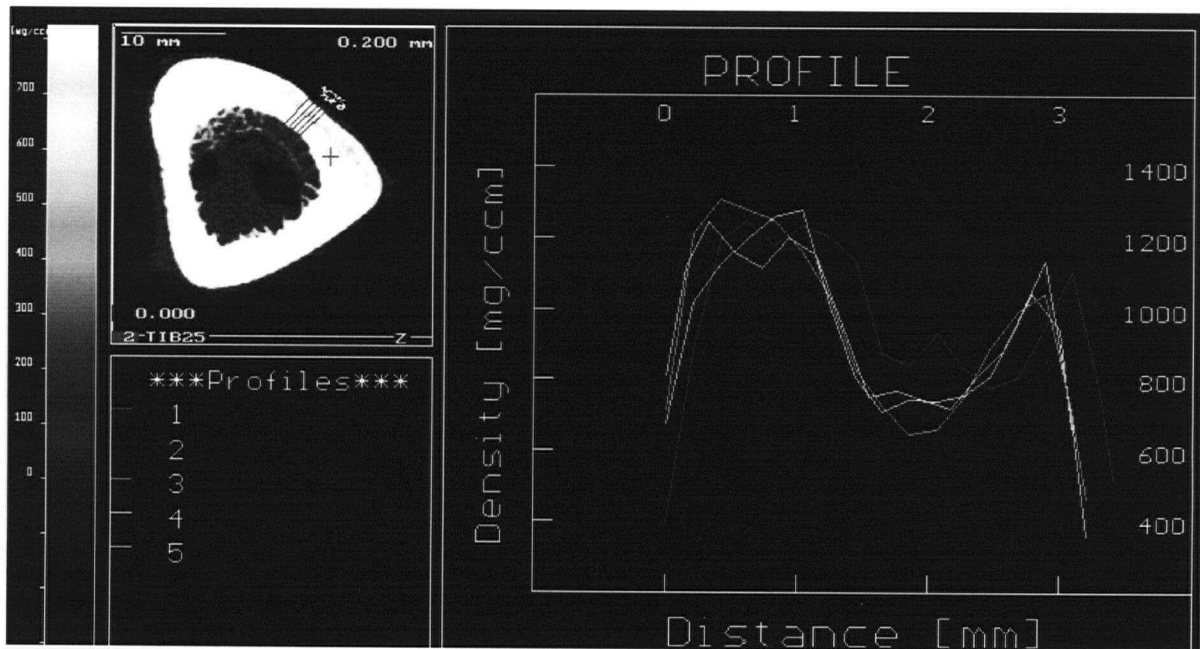


*Figure 4.3 Bone density reading provided by pQCT – sample 1069L*

From the endosteal zone and the adjacent zone, where porosity was not excessive, the apparent density was just as high as any other sample, meaning that bone mineral content had a minor influence in the overall bone density.

The apparent density provided by pQCT was approximately 20% higher than the calculated density based on the experimental measures of bone mineral content and porosity. The

calculated density was based on a surface measurement of bone mineral content using qBSEi. pQCT had a voxel depth of 2.2 mm. The microstructure changes possibly affected these results. Furthermore, pQCT data was measured in fresh unembalmed cadaveric bone, which was still moist. For qBSEi technique, bone was dry, after dehydration in 100% ethylic alcohol. The water content might also affect these results.

The coefficient correlation for the calculated density ( $R = 0.72$ ) was less than what was found for porosity factor only ( $R = -0.79$ ). This is possible due to the fact that the calculated density formula takes into account the bone mineral content. As bone mineral content did not vary across cortical wall thickness as pQCT did, a weak correlation was found ( $R = 0.44$ ), which reduced the calculated density correlation coefficient.

## Chapter 5 Conclusions

1. The material properties measured in this research work appear to be well characterized using a depth dependence measurement provided by continuous stiffness measurement (CSM) mode. This technique allows us to carry out faster and more reliable measurements of both elastic and viscoelastic properties of bone tissue.
2. It can be concluded that water content is very important to the mechanical behaviour of bone, not only from the elasticity aspect, but also the viscoelasticity of bone. The water content during experimental testing enhanced the loss tangent of bone. Bone is viscoelastic down to the level of the individual Haversian system and interstitial bone. The presence of water and the viscoelasticity of bone may thus play important roles in dissipating energy and resisting fracture.
3. Nanoindentation and qBSEi tests found that the elastic modulus of bone increases with the bone mineral content. Regression analyses showed that the relationship between the two parameters was not completely linear. Therefore, the bone mineral content present in bone microstructure is an indicator of quality at the microscale level.
4. It is concluded that interstitial bone was more mineralized than osteonal bone and also had higher elastic modulus.

5. The modulus and bone mineral content distribution across cortical wall presented a different trend, which confirmed the non-linear relationship between these two parameters as seen in the regression analyses. The elastic modulus of bone greatly varied across the cortex; however, the BMC distribution across the cortical wall thickness was fairly uniform.
  
6. The degree of porosity in bone greatly influenced the pQCT measurement of apparent density; however, BMC did not contribute as much as porosity. It is concluded that even though the bone mineral content appeared as an indicator of bone quality at the microscale level, it becomes less obvious at the macroscale level. At this level porosity becomes the major factor affecting bone density.

## Chapter 6 Recommendations for Future Work

Based on the previous work published on the literature of bone and this current research work, some recommendations for future work can be recommended:

- Femoral neck investigation of bone response on the microstructural level to evaluate the effect that bone response to load has in the material properties of bone tissue (Appendix B);
- Conduct the qBSEi analysis of bone mineral content and porosity in all the tibia samples to provide more statistics regarding these data;
- Correlate the pQCT data to all the samples analyzed by qBSEi to enable a more statistical significant correlation;
- Apply the nanoindentation and quantitative backscattered electron imaging techniques as described in this research work to investigate femoral human bone at the hip site, which is one of the main sites of fractures due to osteoporosis disease.

## References

1. NIH Consensus Development Panel on Osteoporosis Prevention, Diagnosis, and Therapy, March 7-29, 2000: highlights of the conference. *South Med J*, 94, (6), p 569-573 (2001).
2. Statistics Canada Report - <http://www.statcan.ca> (1999).
3. Health Canada Report - <http://www.hc-sc.gc.ca> (2000).
4. Cowin, S. C., Bone Mechanics Handbook. Second ed.; CRC Press: 2001; p 1-68.
5. Weiner, S.; Wagner, H. D., The material bone: structure-mechanical function relations. *Annu Rev Mater Sci*, 28, p 271-298 (1998).
6. Weiner, S.; Traub, W.; Wagner, H. D., Lamellar bone: structure-function relations. *J Struct Biol*, 126, (3), p 241-255 (1999).
7. Rho, J. Y.; Kuhn-Spearing, L.; Zioupos, P., Mechanical properties and the hierarchical structure of bone. *Med Eng Phys*, 20, (2), p 92-102 (1998).
8. Currey, J. D., The Mechanical Adaptations of Bones. First ed.; Princeton University Press: 1984; p 24-37.
9. Currey, J. D., Bones: Structure and Mechanics. Second ed.; Princeton University Press: 2002; p 3-26.
10. Mann, S., Biomineralization: the form(id)able part of bioinorganic chemistry. *J Chem Soc*, p 3953-3961 (1997).
11. Lowenstam, H. A.; Weiner, S., On Biomineralization. Oxford University Press: 1989.

12. Mann, S.; Weiner, S., Biomineralization: structural questions at all length scales. *J Struct Biol*, 126, (3), p 179-181 (1999).
13. Wasnich, R. D., A new, standardized approach to fracture risk interpretation. *Hawaii Med J*, 55, (8), p 141-143 (1996).
14. Favus, M. J., Primer on the Metabolic Bone Diseases and Disorders of Mineral Metabolism. Fourth ed.; Lippincott/Williams & Wilkins: 1999.
15. Wasnich, R., Bone mass measurement: prediction of risk. *Am J Med*, 95, (5A), p 6S-10S (1993).
16. Zioupos, P.; Currey, J. D., Changes in the stiffness, strength, and toughness of human cortical bone with age. *Bone*, 22, (1), p 57-66 (1998).
17. National Osteoporosis Foundation - <http://www.nof.org>
18. Frost, H. M., Osteoporoses: a rationale for further definitions? *Calcif Tissue Int*, 62, (2), p 89-94 (1998).
19. Frost, H. M., Changing views about 'Osteoporoses' (a 1998 overview). *Osteoporos Int*, 10, (5), p 345-352 (1999).
20. Frost, H. M., Defining osteopenias and osteoporoses: another view (with insights from a new paradigm). *Bone*, 20, (5), p 385-391 (1997).
21. WHO, Assessment of fracture risk and its applications to screening for postmenopausal osteoporosis. *WHO Technical Report Series 843*, (1994).

22. Kanis, J. A., Assessment of fracture risk and its application to screening for postmenopausal osteoporosis: synopsis of a WHO report. WHO Study Group. *Osteoporos Int*, 4, (6), p 368-381 (1994).
23. Richmond, B., DXA scanning to diagnose osteoporosis: do you know what the results mean? *Cleve Clin J Med*, 70, (4), p 353-360 (2003).
24. Muller, A.; Ruegsegger, E.; Ruegsegger, P., Peripheral QCT: a low-risk procedure to identify women predisposed to osteoporosis. *Phys Med Biol*, 34, (6), p 741-9 (1989).
25. Schneider, P.; Borner, W., Peripheral quantitative computed tomography for bone mineral measurement using a new special QCT-scanner. Methodology, normal values, comparison with manifest osteoporosis. *Rofo*, 154, (3), p 292-299 (1991).
26. Ito, M.; Tsurusaki, K.; Hayashi, K., Peripheral QCT for the diagnosis of osteoporosis. *Osteoporos Int*, 7 Suppl 3, p 120S-127S (1997).
27. Schneider, P.; Butz, S.; Allolio, B.; Borner, W.; Klein, K.; Lehmann, R.; Petermann, K.; Tysarczyk-Niemeyer, G.; Wuster, C.; Zander, C.; et al., Multicenter German reference data base for peripheral quantitative computer tomography. *Technol Health Care*, 3, (2), p 69-73 (1995).
28. Tysarczyk-Niemeyer, G., New noninvasive pQCT devices to determine bone structure. *Jpn Soc Bone Morphom*, (7), p 97-105 (1997).
29. Boivin, G.; Meunier, P. J., Methodological considerations in measurement of bone mineral content. *Osteoporos Int*, 14 Suppl 5, p 22-28 (2003).

30. Dickson, G. R., *Methods of Calcified Tissue Preparation*. First ed.; Elsevier: 1984; p 251-307.
31. Boivin, G.; Meunier, P. J., The degree of mineralization of bone tissue measured by computerized quantitative contact microradiography. *Calcif Tissue Int*, 70, (6), p 503-511 (2002).
32. Meunier, P. J.; Boivin, G., Bone mineral density reflects bone mass but also the degree of mineralization of bone: therapeutic implications. *Bone*, 21, (5), p 373-377 (1997).
33. Goldstein, J. I., *Scanning electron microscopy and x-ray microanalysis*. Third ed.; New York: Kluwer Academic/Plenum Publishers: 2003.
34. Skedros, J. G.; Bloebaum, R. D.; Bachus, K. N.; Boyce, T. M.; Constantz, B., Influence of mineral content and composition on graylevels in backscattered electron images of bone. *J Biomed Mater Res*, 27, (1), p 57-64 (1993).
35. Boyde, A.; Reid, S. A., A new method of scanning electron microscopy for imaging biological tissues. *Nature*, 302, (5908), p 522-523 (1983).
36. Skedros, J. G.; Bloebaum, R. D.; Bachus, K. N.; Boyce, T. M., The meaning of graylevels in backscattered electron images of bone. *J Biomed Mater Res*, 27, (1), p 47-56 (1993).
37. Roschger, P.; Fratzl, P.; Eschberger, J.; Klaushofer, K., Validation of quantitative backscattered electron imaging for the measurement of mineral density distribution in human bone biopsies. *Bone*, 23, (4), p 319-326 (1998).

38. Gupta, H. S.; Schratte, S.; Tesch, W.; Roschger, P.; Berzlanovich, A.; Schoeberl, T.; Klaushofer, K.; Fratzl, P., Two different correlations between nanoindentation modulus and mineral content in the bone-cartilage interface. *J Struct Biol*, 149, (2), p 138-148 (2005).
39. Weber, M.; Schoeberl, T.; Roschger, P.; Klaushofer, K.; Fratzl, P., Relating local bone stiffness and calcium content by combined nanoindentation and backscattered electron imaging. *Mater. Res. Soc. Symp. Proc. Vol. 874* (2005).
40. Ferguson, V. L.; Bushby, A. J.; Boyde, A., Nanomechanical properties and mineral concentration in articular calcified cartilage and subchondral bone. *J Anat*, 203, (2), p 191-202 (2003).
41. Ito, M., [Assessment of bone quality--present and future]. *Clin Calcium*, 14, (12), p 27-32 (2004).
42. Dalle Carbonare, L.; Giannini, S., Bone microarchitecture as an important determinant of bone strength. *J Endocrinol Invest*, 27, (1), p 99-105 (2004).
43. Ammann, P.; Rizzoli, R., Bone strength and its determinants. *Osteoporos Int*, 14 Suppl 3, p S13-8 (2003).
44. Ammann, P., [Determining factors of bone mechanical resistance]. *Therapie*, 58, (5), p 403-407 (2003).
45. Bhushan, B.; Li, X., Nanomechanical Characterization of Solid Surfaces and Thin Films. *International Materials Reviews*, 48, (3), p 125-164 (2003).

46. Haque, F., Application of Nanoindentation to Development of Biomedical Materials. *Surface Engineering*, 19, (4), p 255-268 (2003).
47. VanLandingham, M. R., Review of Instrumented Indentation. *Journal of Research of the National Institute of Standards and Technology*, 108, (4), p 249-265 (2003).
48. MTS - NanoIndenter XP User's Manual.
49. Li, X.; Bhushan, B., A review of nanoindentation continuous stiffness measurement technique and its applications. *Materials Characterization*, 48, p 11-36 (2002).
50. Cowin, S. C., Bone Mechanics. Second ed.; CRC Press: 1988.
51. Fan, Z.; Swadener, J. G.; Rho, J. Y.; Roy, M. E.; Pharr, G. M., Anisotropic properties of human tibial cortical bone as measured by nanoindentation. *J Orthop Res*, 20, (4), p 806-810 (2002).
52. Rho, J. Y.; Roy, M. E., 2nd; Tsui, T. Y.; Pharr, G. M., Elastic properties of microstructural components of human bone tissue as measured by nanoindentation. *J Biomed Mater Res*, 45, (1), p 48-54 (1999).
53. Swadener, J. G.; Rho, J. Y.; Pharr, G. M., Effects of anisotropy on elastic moduli measured by nanoindentation in human tibial cortical bone. *J Biomed Mater Res*, 57, (1), p 108-112 (2001).
54. Rho, J. Y.; Tsui, T. Y.; Pharr, G. M., Elastic properties of human cortical and trabecular lamellar bone measured by nanoindentation. *Biomaterials*, 18, (20), p 1325-1330 (1997).

55. Zysset, P. K.; Guo, X. E.; Hoffler, C. E.; Moore, K. E.; Goldstein, S. A., Elastic modulus and hardness of cortical and trabecular bone lamellae measured by nanoindentation in the human femur. *J Biomech*, 32, (10), p 1005-1012 (1999).
56. Hengsberger, S.; Kulik, A.; Zysset, P., Nanoindentation discriminates the elastic properties of individual human bone lamellae under dry and physiological conditions. *Bone*, 30, (1), p 178-184 (2002).
57. Bushby, A. J.; Ferguson, V. L.; Boyde, A., Nanoindentation of bone: Comparison of specimens tested in liquid and embedded in polymethylmethacrylate. *J Mater Res*, 19, (1), p 249-259 (2004).
58. Rho, J. Y.; Pharr, G. M., Effects of drying on the mechanical properties of bovine femur measured by nanoindentation. *J Mater Sci Mater Med*, 10, (8), p 485-488 (1999).
59. Glantz, S. A., Primer of Bio-statistics. Fourth ed.; Mc Graw Hill: p 32-107 and 282-322.
60. Altman, D. G., Practical statistics for medical research. p 325-364 (1999).

## Appendices

### Appendix A – Contact Microradiography

Even though contact microradiography was not fully used in this research work, a preliminary study was conducted with this technique. The following picture was taken with an exposure of 30 minutes using a radiographic beam of 25 kV and 50 mA. The x-ray source was located 30 cm away from the sample. Following the exposure to the radiographic beam, the radiographic film was developed in a Kodak D-19 developer for 5 minutes. Rinsed, fixed in an acidic fixative for 15 minutes and rinsed again in water.

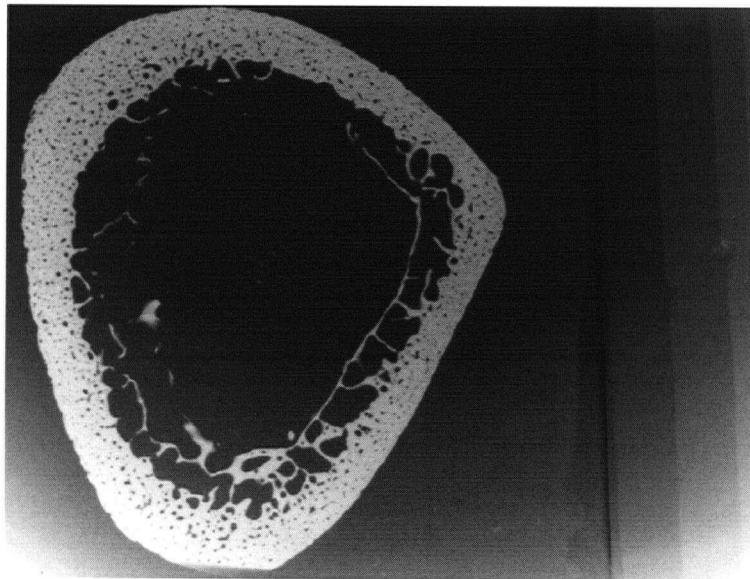


*Figure A1 Contact microradiograph picture with aluminium step-wedge calibration.*

However, the thickness of 100  $\mu\text{m}$  was much larger than the thickness penetrated by the indenter tip (2  $\mu\text{m}$ ). There was also technical difficulty of achieving homogeneous irradiation across the specimen as the x-ray source did not emit parallel beams.

## Appendix B – Anatomical Site Testing

In addition to the Medial Analysis described above, two samples were tested on six anatomical sites, including the three extremity tips and the three uniform flat areas (medial, posteromedial, posterior, posterolateral, lateral, and anterior – Figure 2.2a). The selected specimens had very distinct characteristics (Table B1). Sample 1096R was a large and strong, while 1067R was a small and weaker specimen. Each of the six sites in the sample 1067R had 75 indentations and in the sample 1096R had 96 indentations. A total of 1026 indentations were made for this set of measurements.

The area measurement in Table B1 comes from Peripheral Quantitative Computed Tomography (pQCT) measurements and the energy to failure values from macromechanical compressive testing. These two measurements were provided by Cecilia Tang at the Vancouver General Hospital.

*Table B1 Bone specimens for anatomical site testing.*

Sample	Gender	Age	Area, mm <sup>2</sup>	Energy to Failure (mJ)	# of indentations
1067R	F	73	304.4	4528.1	450
1096R	M	73	402.7	18576.1	576

An essential and remarkable feature of bone is its ability to respond to load. Bone is able of adapting its macrostructure to external loading in order to avoid fracture. However, little is known about that bone adaptation in a material level, the response of an individual osteon or interstitial bone to loading. This appendix provides a preliminary study on this topic.

Figures B1 and B2 present the elastic modulus distribution for sample 1067R and 1096R, respectively. The distribution curves cover the six anatomical sites of the 25% distal tibia, namely, medial, posteromedial, posterior, posterolateral, lateral, and anterior.

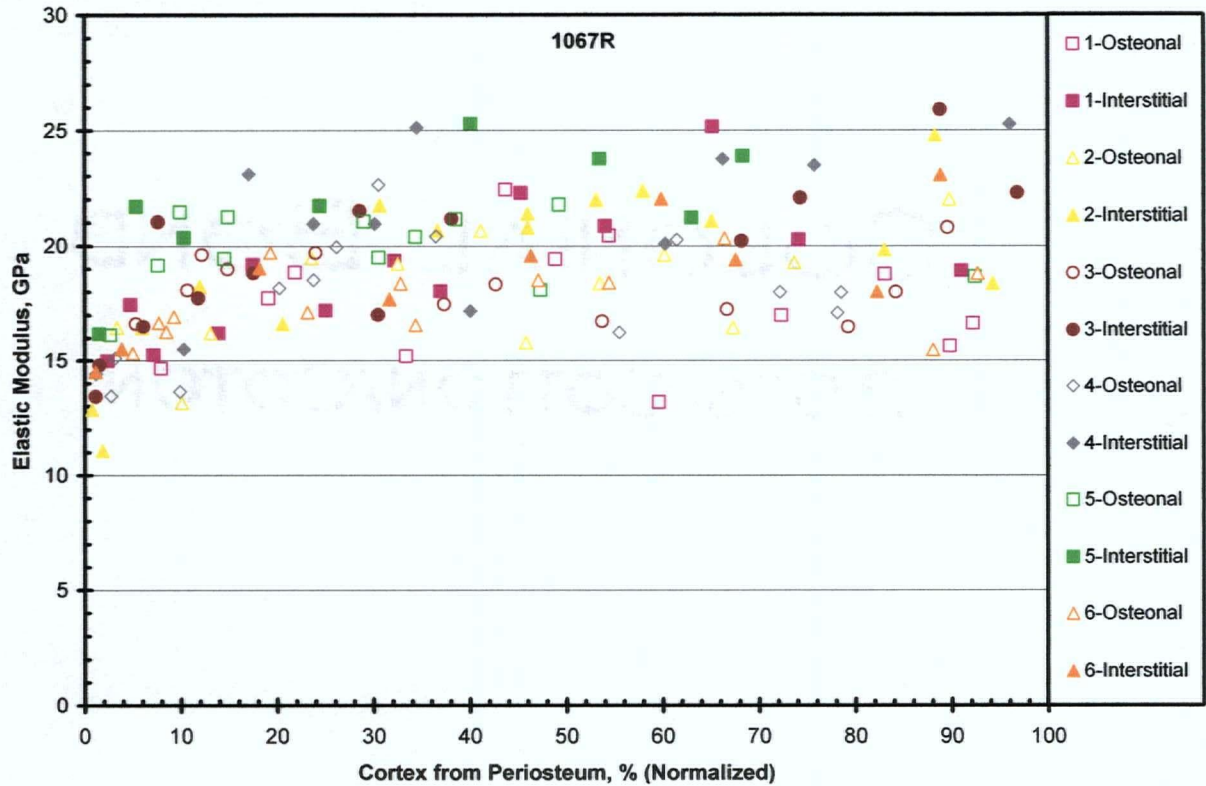


Figure B1 Modulus distribution – 1067R – all anatomical sites.

The modulus distribution curves for specimen 1067R (Figure B1) revealed a large scattering of data, from 11 GPa to 26 GPa; however, most of the data were between 16 GPa and 22 GPa. There was no remarkable alteration among the six different anatomical sites. The same tendency was observed for sample 1096R (Figure B2). An increase of about 2 GPa was found in sample 1096R, where most of the data were between 18 GPa and 24 GPa. There were some indications that the intraindividual variation (among different anatomical sites) was less significant than the interindividual variation (person to person).

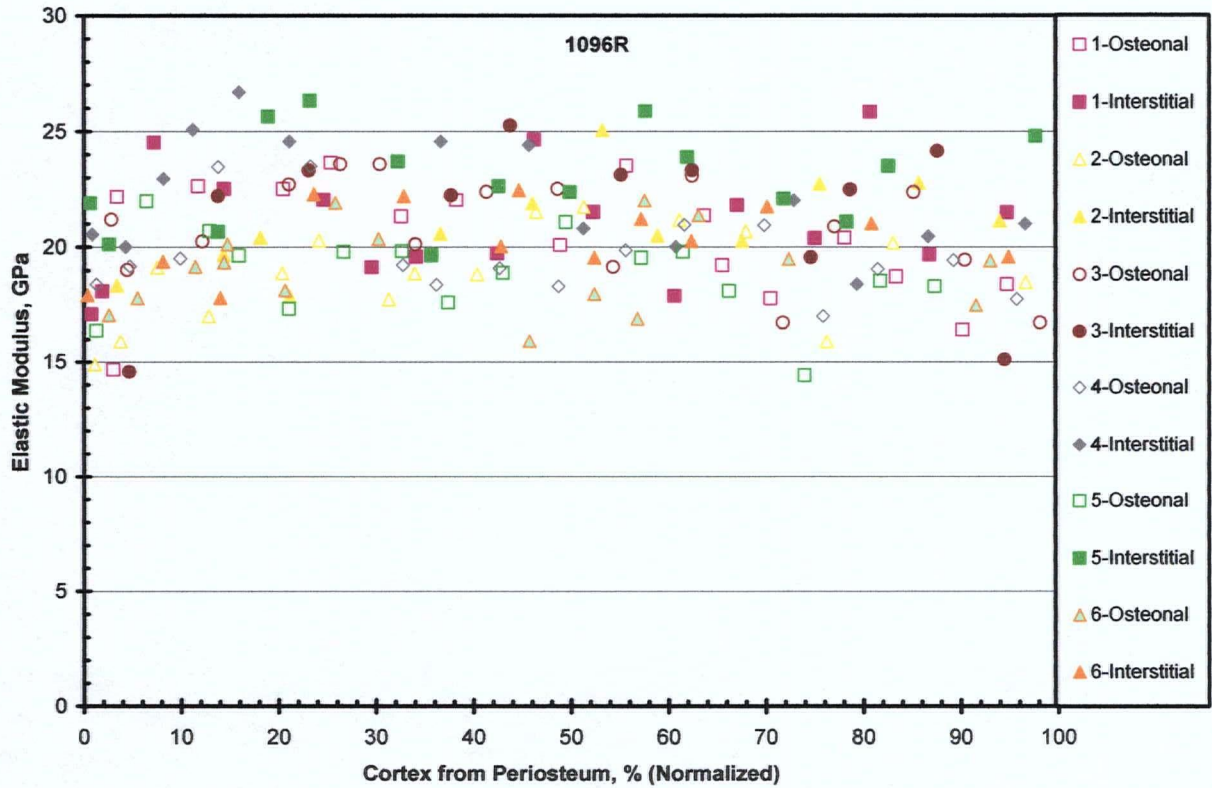


Figure B2 Modulus distribution – 1096R – all anatomical sites.

Figure B3 shows the mean value and standard deviation for elastic modulus according to anatomical site. Interstitial bone had higher elastic modulus than osteonal bone for both samples and for all anatomical sites. However, little can be concluded from the variation in material properties according to anatomical site. Besides the lateral site, the variation among the other anatomical sites appeared to be very small. More data should be acquired to provide a reliable statistical analysis.

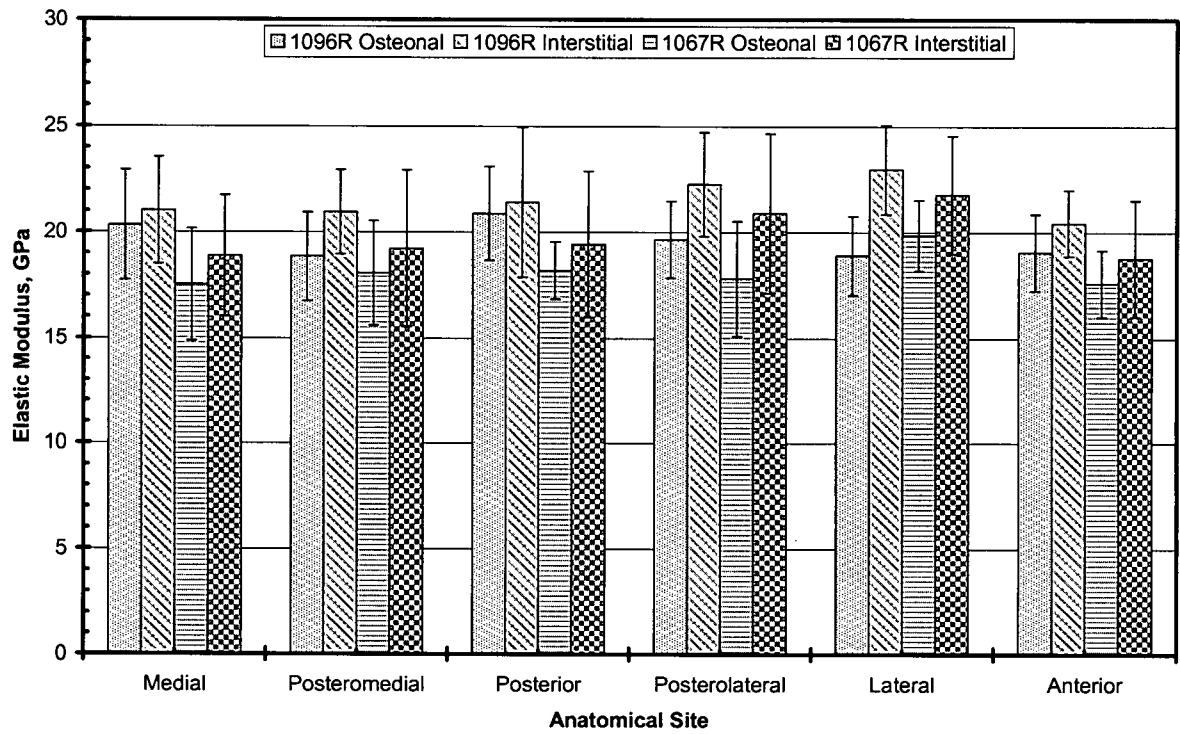


Figure B3 Mean ( $\pm$ SD) elastic modulus – anatomical sites.

## Appendix C – Newman-Keuls Post-hoc analysis

*Table C1 Modulus Post-hoc analysis – Newman-Keuls test.*

Var	O1	I1	O2	I2	O3	I3	O4	I4	O5	I5
O1		0.00014	0.00024	0.00014	0.00020	0.00015	0.00023	0.00013	0.00027	0.00014
I1	0.00014		0.10614	0.00715	0.11744	0.00237	0.15482	0.00424	0.14050	0.72593
O2	0.00024	0.10614		0.00014	0.79867	0.00014	0.71687	0.00014	0.83498	0.06510
I2	0.00014	0.00715	0.00014		0.00021	0.59037	0.00016	0.97266	0.00017	0.01016
O3	0.00020	0.11744	0.79867	0.00021		0.00016	0.84861	0.00021	0.73658	0.13667
I3	0.00015	0.00237	0.00014	0.59037	0.00016		0.00014	0.83324	0.00014	0.00419
O4	0.00023	0.15482	0.71687	0.00016	0.84861	0.00014		0.00016	0.83591	0.10896
I4	0.00013	0.00424	0.00014	0.97266	0.00021	0.83324	0.00016		0.00016	0.00417
O5	0.00027	0.14050	0.83498	0.00017	0.73658	0.00014	0.83591	0.00016		0.11567
I5	0.00014	0.72593	0.06510	0.01016	0.13667	0.00419	0.10896	0.00417	0.11567	

*Table C2 Bone Mineral content Post-hoc analysis – Newman-Keuls test.*

Var	O1	I1	O2	I2	O3	I3	O4	I4	O5	I5
O1		0.00637	0.90287	0.01275	0.94065	0.06472	0.93427	0.08383	0.92640	0.15094
I1	0.00637		0.00644	0.59083	0.00813	0.25812	0.00745	0.25538	0.00648	0.15692
O2	0.90287	0.00644		0.01264	0.89965	0.06322	0.82387	0.07813	0.97398	0.13181
I2	0.01275	0.59083	0.01264		0.01507	0.28800	0.01432	0.36770	0.01313	0.26343
O3	0.94065	0.00813	0.89965	0.01507		0.06932	0.83541	0.06917	0.96152	0.07484
I3	0.06472	0.25812	0.06322	0.28800	0.06932		0.06969	0.77231	0.06721	0.69408
O4	0.93427	0.00745	0.82387	0.01432	0.83541	0.06969		0.07987	0.96904	0.11847
I4	0.08383	0.25538	0.07813	0.36770	0.06917	0.77231	0.07987		0.08984	0.60526
O5	0.92640	0.00648	0.97398	0.01313	0.96152	0.06721	0.96904	0.08984		0.16783
I5	0.15094	0.15692	0.13181	0.26343	0.07484	0.69408	0.11847	0.60526	0.16783	